10-2015

Development of Material Characterization Techniques using Novel Nanoindentation Approaches on Hard and Soft Materials used in MEMS

Eyup Cinar
exc8020@rit.edu

Recommended Citation

Cinar, Eyup, "Development of Material Characterization Techniques using Novel Nanoindentation Approaches on Hard and Soft Materials used in MEMS" (2015). Thesis. Rochester Institute of Technology. Accessed from

Development of Material Characterization Techniques using Novel Nanoindendation Approaches on Hard and Soft Materials used in MEMS

by

Eyup Cinar

A Dissertation Submitted in Partial Fulfillment of the Requirements for the
Degree of Doctor of Philosophy
in Microsystems Engineering

Supervised by

Professor Dr. Ferat Sahin
Department of Electrical and Microelectronic Engineering
Kate Gleason College of Engineering
Rochester Institute of Technology
Rochester, New York
October 2015

Committee Approval:

We, the undersigned committee members, certify that we have advised and/or supervised the candidate on the work described in this dissertation. We further certify that we have reviewed the dissertation manuscript and approve it in partial fulfillment of the requirements of the degree of Doctor of Philosophy in Microsystems Engineering

Dr. Ferat Sahin, Professor
Dissertation Advisor, Department of Electrical and Microelectronic Engineering

Dr. David Borkholder, Professor
Committee Member, Department of Electrical and Microelectronic Engineering

Dr. Karl Hirschman, Professor
Committee Member, Department of Electrical and Microelectronic Engineering

Dr. Jiandi Wan, Assistant Professor
Committee Member, Microsystems Engineering

Certified by:

Dr. Bruce Smith, Prof.
Director, Microsystems Engineering Program

Dr. Harvey Palmer, Prof.
Dean, Kate Gleason College of Engineering

Dedication

I dedicate this dissertation work to my loving parents Nevin, Ibrahim and Elif Cinar for their unending support and sacrifices they have had for me.

I also dedicate this dissertation work to my friends who have always been there for me whenever I needed them.

Acknowledgments

First and foremost, I would like to thank Dr. Ferat Sahin for his support as my supervisor who has been very generous, merciful, and patient throughout my entire graduate life.

I wish to thank my committee members Dr. David Borkholder, Dr. Karl Hirschman and Dr. Jiandi Wan for agreeing to serve on my committee, their help, and valuable feedbacks.

Also, I would like to acknowledge Nanonics Imaging Ltd. (Jerusalem, Israel), particularly Prof. Aaron Lewis for his collaboration and support in this research.

Lastly, I am thankful for my coworkers and friends Celal Savur, Shitij Kumar and Ryan Bowen for their support.

Abstract

Development of Material Characterization Techniques using Novel Nanoindendation Approaches on Hard and Soft Materials used in MEMS

Eyup Cinar

Supervising Professor: Dr. Ferat Sahin

Investigating and modeling the mechanical properties of materials is important for many applications. The most common technique used for mechanical characterization of materials is called nanoindentation. The currently available tools utilized in order to perform nanoindentation have their limitations in terms of sensitivities in force and displacement for a broad range of material properties. When it comes to investigation of soft materials, these limitations might be more detrimental. In this dissertation work, novel nanoindentation techniques have been developed with a multi-probe scanning force microscopy (SPM) system in order to ease the major problems encountered with standard Atomic Force Microscopy (AFM) or nanoindentation systems. Tuning forks are used as probes during nanoindentation. By using the newly developed nanoindentation techniques for quasi-static nanoindentation experiments, the force information is extracted through the displacement of the indenter probe measured by a second probe with ultra-resolution. For dynamic nanoindentation, frequency modulation techniques have been used to extract force information from a single indenter tuning-fork probe. Thanks to the high quality of resonance (Q factor) of tuning fork probes, force measurements can be performed with an ultra high resolution. The accurate measurements of material properties on soft materials is used in characterization of microfabricated pillar sensors which can be used in measuring nN level of cell traction forces in a biomedical application. The techniques developed in this research also enable the system as an ultra-sensitive force sensor to apply nN scale lateral and vertical loads on microfabricated structures or biological specimens.

Contents

List of Tables

List of Figures

List of Publications

- **Journal Publications**
    1. E. Cinar, F. Sahin, D. Yablon, ”Development of a Novel Nanoindentation Technique by Utilizing a Dual-probe AFM System,” Beilstein Journal of Nanotechnology.
    2. E. Cinar and F. Sahin, ”A System of Systems Perspective to a Multi-Probe SPM System,” Int. Journal of Complex Systems: Computing, Sensing and Control.
- **Conference Publications**
    1. E. Cinar and F. Sahin, ”A New Approach for Nanoindentation using Multiprobe AFM System,” in Proc. of IEEE 14th International Conference on Nanotechnology, Toronto, Canada, 2014.
    2. E. Cinar and F. Sahin,, ”A system of systems analysis of a multiprobe SPM system,” in Proc. of IEEE 10th System of Systems Engineering Conference (SoSE), San Antonio, TX, USA, 2015.

List of Main Contributions

- A novel approach to nanoindentation has been developed with a multi-probe (SPM) system. This new approach has an ultra resolution in depth sensing and eliminates the drawbacks of current nanoindentation techniques performed particularly with atomic-force-microscopy (AFM) system on hard materials.
- Dynamic nanoindentaion methods are employed on characterization of soft materials utilizing tuning-fork indentation probes. Frequency-modulation technique is used to extract force values during nanoindentation. By this way, higher force resolution is achieved and significant improvement in the contact detection is provided.
- Ultra sensitive tuning fork force sensors are utilized in mechanical characterization of PDMS micropillar structures. These microstructures have been commonly used in many biomedical studies as force sensors. A through investigation of mechanical models for comparison with the experimental data is performed.

Chapter 1

Introduction

Characterizing the mechanical properties of materials is crucial for many applications. Various testing methods have been developed over the years in order to be able to investigate these properties and obtain the most accurate characterization as possible. Nanoindentation is one of these techniques that has been employed when other conventional testing methods (tensile, compressive testing) are not viable due to limited specimen resources or in the case of ultra soft materials for example a soft tissue [1], [2].

In nanoindentation, the material under the investigation is indented with a probe that carries a hard material tip with a known geometry and mechanical properties. Based on the level of submicron measured depth of penetration, contact area and applied load information; one can extract the mechanical properties of the material. The nanoindentation technique can be used on variety of materials and can result in the wide range of applications e.g. application of nanoindentation in order to show changes in nanomechanical properties of cancer cells with respect to healthy cells [3] and investigating the mechanical properties of wood cells by nanoindentation [4].

The most common tool used for nanoindentation experiments that do not require low force levels and high sensitivity measurement is *instrumented nanoindenter tools* (INI). Figure 1.1 shows an example schematic that illustrates the main components of an instrumented nanoindenter. The load is applied in vertical direction through electromagnetically generated force and the displacement is measured by capacitive sensors integrated into the system. These types of systems are preferred when high force levels are required. However, the sensitivity of the force and the displacement might not be as high as AFM's resolution therefore similar surface detection errors can also occur. By the time a surface contact is detected, the indenter might already be penetrated into the sample. This might cause significant overestimation of the material properties as it is addressed in [5].

In addition to instrumented nanoindenter (INI) tools, nanoindentation experiments can be also performed with an Atomic Force microscopy (AFM) tool. With AFM, usually a silicon cantilever is used to probe surface properties. As the cantilever is oscillated (tapping mode), the deflection of the cantilever is measured by a laser beam focused on the back of the cantilever. The deflected laser is measured by a quadrant photodiode and the displacement of the cantilever is measured as depicted in Figure 1.2. This technique

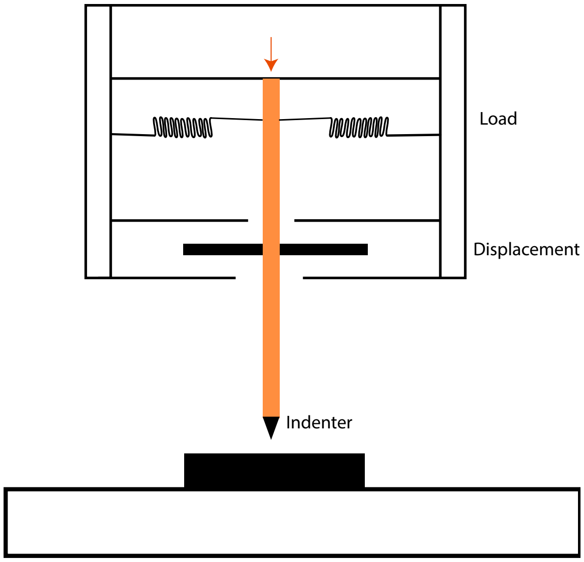

Figure 1.1: A schematic illustrating an instrumented nanoindenter tool.

is known as optical level method or beam bounce technology [6]. For a sample scanning operation, the voltage signal that is read from photodiode is amplified and sent over to feedback loop system for precise movement of the piezo scanner. Based on this feedback loop, the probe is kept within certain amount of error and in a highly ‘sensitive’ contact with the sample for an ultra resolution image of the sample.

An AFM system as shown in Figure 1.2 can be used for nanoindentation on different types of materials. The probe is used for indenting the material and the displacement of the indentation is read by laser beam bounce. Based on the spring constant of AFM cantilever and the displacement value, force curve plots can be deduced. These curves can be used to understand the

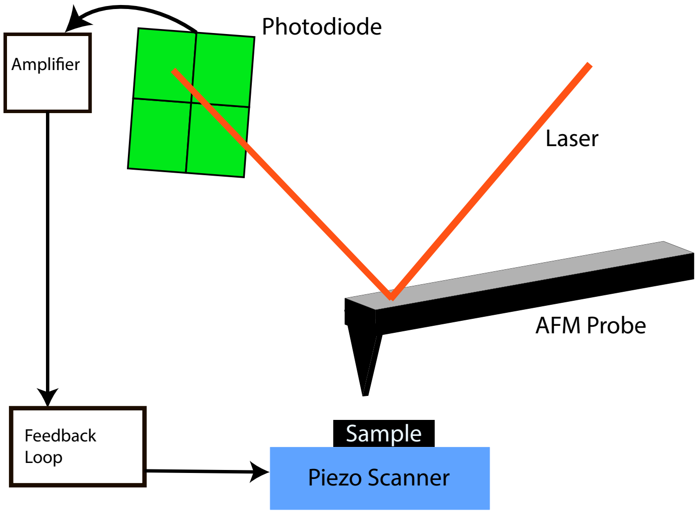

Figure 1.2: Schematic representation of an AFM system.

mechanical properties of the materials of interest. An AFM system is preferred usually when very small indentation is desired and high resolution of force and depth sensing is needed. In order to enable nanoindentation by using AFM systems on hard materials which require higher force levels, manufacturers provide stiffer indentation probes with diamond tips attached to the end of cantilever probes.

The high resolution imaging capability of AFM systems after performing the nanoindentation experiments is a powerful advantage of AFM systems. Through this, an accurate nanoindentation profile can be extracted after the experiment is completed.

However, one of the major problems of conventional AFM systems when they are used for force measurements is jump-to-contact or adhesion problems. As illustrated in Figure 1.3, due to relatively compliant cantilevers that are used and tip surface interaction forces, as the AFM probe approaches to the sample surface, after a critical point the probe snaps in to the surface. The magnitude of tip surface interaction forces that cause this effect might be considerably high even it may cause small depth indentation on soft materials [7]. Sun et al. calculates elastic modulus of PDMS soft material based on the indentation effects that are created by this phenomena [7].

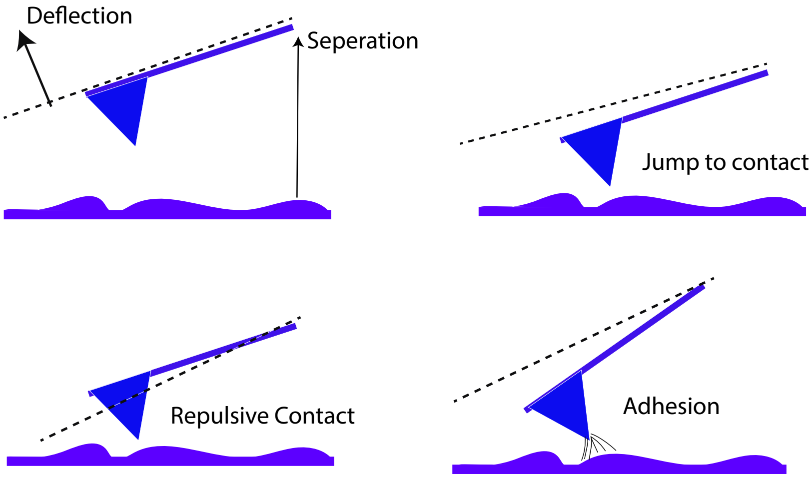

Figure 1.3: Illustration of an AFM probe approach and retract

Figure 1.4 shows an example force distance curve on PDMS obtained by Sun et al. [7]. As the AFM cantilever approaches the surface, at around 60 nm above the surface, due to adhesive interaction forces, the tip jumps into to surface of the specimen and indents the material. As the probe is retracted from the surface, adhesive forces come into play and creates the apparent hysteresis, as known as *Adhesive Hysteresis* [7].

Moreover, the second major problem occurs when nanoindentation is

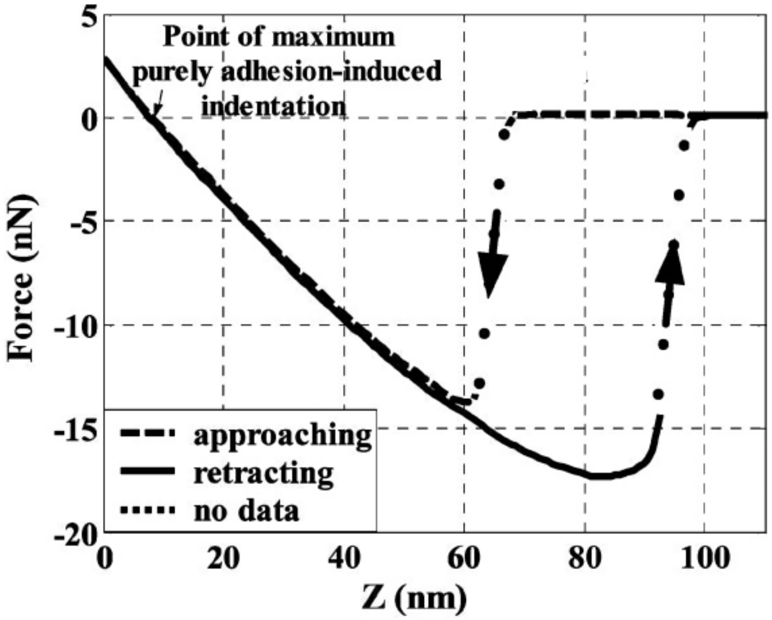

Figure 1.4: An example AFM force-distance curve on PDMS showing jump to contact and indentation effect [7]

performed on soft/bio materials by using a conventional AFM system with a compliant cantilever probe. As the probe approaches to the surface for indentation, the point of contact might not be accurately determined. Due to the complex nature of tip-sample interaction forces, it might get very hard to determine zero indentation point $(h = 0)$. This is commonly known as *surface detection problem* and might cause significant overestimation errors of material elastic properties as studied in [8].

Furthermore, during nanoindentation when an AFM probe is used to indent the sample, cantilever probes bend. The displacement that is read by optical lever method include both the indentation depth and bending of the cantilever. This also causes over-estimation problems on estimating the material properties due to displacement error caused by bending of the probe.

Since, for most of the AFM systems, the movement of the cantilever in XYZ directions are provided with one piezoelectric actuator and they are coupled, this results into hardware limitations on the application of complete uniaxial load and reading the measured forces for soft materials [9]. Ren and Zou provide control based solutions to this problem in order to eliminate the effects on this hardware limitations, as well [9].

A comparison of two techniques for nanoindentation experiments are given in Table 1.1. Among the several drawbacks of INI systems are low load and displacement sensitivity and lack of nm-scale profiling for extracting the nanoindentation experiments are performed [10]. On the other hand, AFM systems suffer from low lateral spring constant values which cause overestimation errors due to convolution of X and Y motion into Z motion during a nanoindentation experiment.

The focus of this dissertation is to develop and implement novel techniques in an effort to overcome the above mentioned drawbacks of currently available systems. In addition, the developed techniques are employed in accurate mechanical characterization of materials that are commonly used in micro-fabrication of *Micro-Electro-Mechanical-Systems* (MEMS) devices. These include hard and polymeric soft material such as *poly-dimethyl-siloxane*

Table 1.1: Comparison of Instrumented Indenter system to AFM nanoindentation method [10]

Characteristic	INI	AFM
Vertical spring constant	100 N/m	from <0.01 N/m to over 500 N/m
Lateral spring constant	10^5 N/m	10 - 1000 N/m
Lowest fundamental resonance	20-500 kHz	several thousand kHz
Displacement sensitivity	1 nm	0.05 nm or better
Load Sensitivity	10 nN	<0.05 nm or better
Dynamic range of force	10^8 N/m	10^3 N/m
nm-scale imaging	nonexistent to fair	excellent
Bandwidth	0.001- 100 Hz	1 Hz- several kHz
Temporal stability	good	fair

(PDMS).

The new proposed approaches are developed by utilizing a multi-probe Scanning Probe Microscopy (SPM) system that utilize tuning-fork based technology as opposed to conventional AFM cantilevers. Instead of relying on the displacement of a cantilever which is sensed by a laser beam as shown in Figure 1.2; our approaches extract the force information either through frequency modulation or through the deflection of the turning fork probe by utilizing a second probe system. The second probe is another independently operated SPM system which is kept in constant feedback contact on top of the indenter probe system to enable ultra resolution depth sensing during nanoindentation. A detailed representative figure is presented in Figure 1.5.

The self-oscillating tuning forks fabricated out of quartz piezo material has very sharp resonance curves. The sharper a resonance curve is higher the quality of resonance (Q factor) which enables ultra sensitive feedback

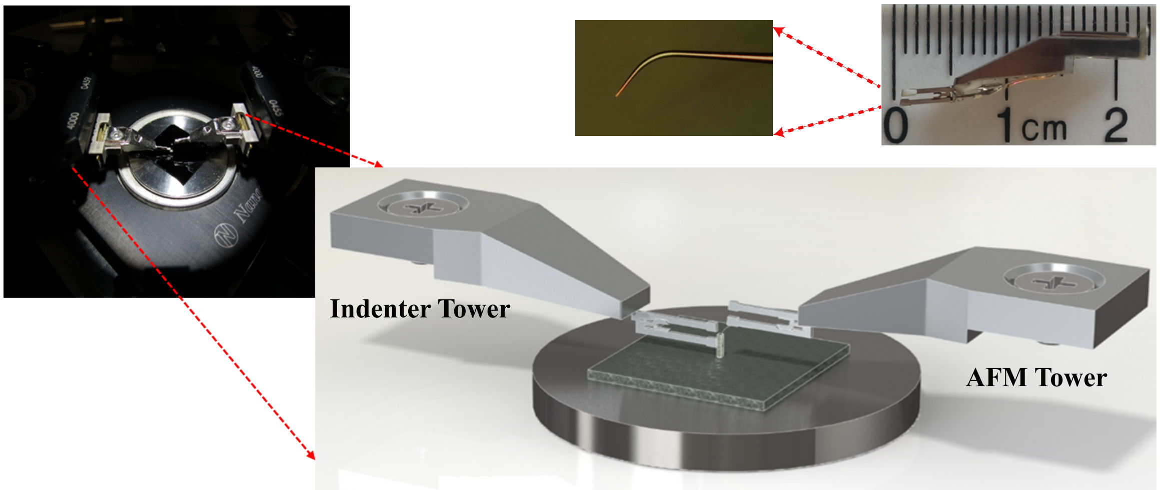

Figure 1.5: Representative schematic demonstrating a proposed two probe nanoindentation approach technique

mechanisms based on either the change of amplitude or the phase. Therefore, extremely high resolution force-displacement data for nanoindentation experiments can be obtained.

The high spring constant of tuning-forks also eliminates the previously mentioned bending errors introduced by compliant AFM cantilever probes during nanoindentation. The integration of the second probe that is only used to monitor the Z motion of the indenter probe with an ultra resolution eliminates the errors introduced by convolution of X and Y motion into Z motion due to low lateral spring constants as discussed in Table 1.1. The ultra-sensitive force sensor developed in this dissertation work is used on characterization of micropillar sensors. These sensors can also be used in a biomedical application to measure cell traction forces.

In the following chapter, a detailed examination of the multi-probe system that is used to develop new characterization techniques is introduced to the reader. In Chapter 3, we discuss the details of our novel multi-probe nanoindentation technique and related work in the literature. In chapter 4, the dynamic nanoindentation technique based on frequency modulation is shown and compared with other studies in the literature. Mechanical characterization of high-aspect-ratio micropillar structures by utilizing frequency modulation technique is presented in chapter 5. As an application, preliminary results on cell traction force microscopy is demonstrated. The last chapter is devoted to the derived conclusions of this dissertation work.

Chapter 2

An overview of the multi-probe system

The novel nanocharacterization techniques developed in this dissertation utilize a multi-probe scanning probe microscopy (SPM) system called Multi-View MV-4000 manufactured by Nanonics Imaging Ltd. [11].

Scanning probe microscopes are used in the field of nanotechnology and are crucial tools for the industry [6]. As the name implies, in SPMs, a cantilevered glass probe is used to probe surface properties of a specimen. This might include a high-resolution image of a surface in atomic resolution [12] or several other properties such as mechanical and electrical properties. In order to achieve this, the probe system is equipped with other subsystems that include complex circuitry such as PID controllers for feedback control, piezo scanners for precise positioning, Phase-Lock-Loop controllers, function generators, and power supplies.

Most of the SPM systems include single probe systems with the above mentioned subsystems. However, effective integration of multiple large systems that cooperatively working might open news doors to obtain higher capabilities and high level performance.

Figure 2.1 shows the single tower system and its subcomponents. A probe that consists of a tuning fork and an attached specialized probe tip is mounted at the end of the piezo scanners as shown in Figure 2.1. Tuning forks as high quality resonators are oscillated at $\sim$ 32 kHz by a 5V reference signal generated in SPM Controller box. SPM controller box includes PID feedback gains, low pass filter, and monitoring knobs that works as a switch to select between the signals of interest coming from different equipment, a mode switch that selects the card which carries out the signal processing, and a built-in lock-in card used during extracting the error signal.

There are three individual stepper motors for each direction (X, Y, Z). These are used to move the probe coarsely in each direction and have 21 nm of resolution. Among these, X and Y stepper motors are controlled by the multi-channel stepper motor system and the Z stepper motor is controlled by SPM controller box.

There is a computer that runs control software and provides a user interface for monitoring and programming the single system for each task. The computer is equipped with Data Translation hardware cards that provide high speed analog and digital input/output acquisition in order to be able to

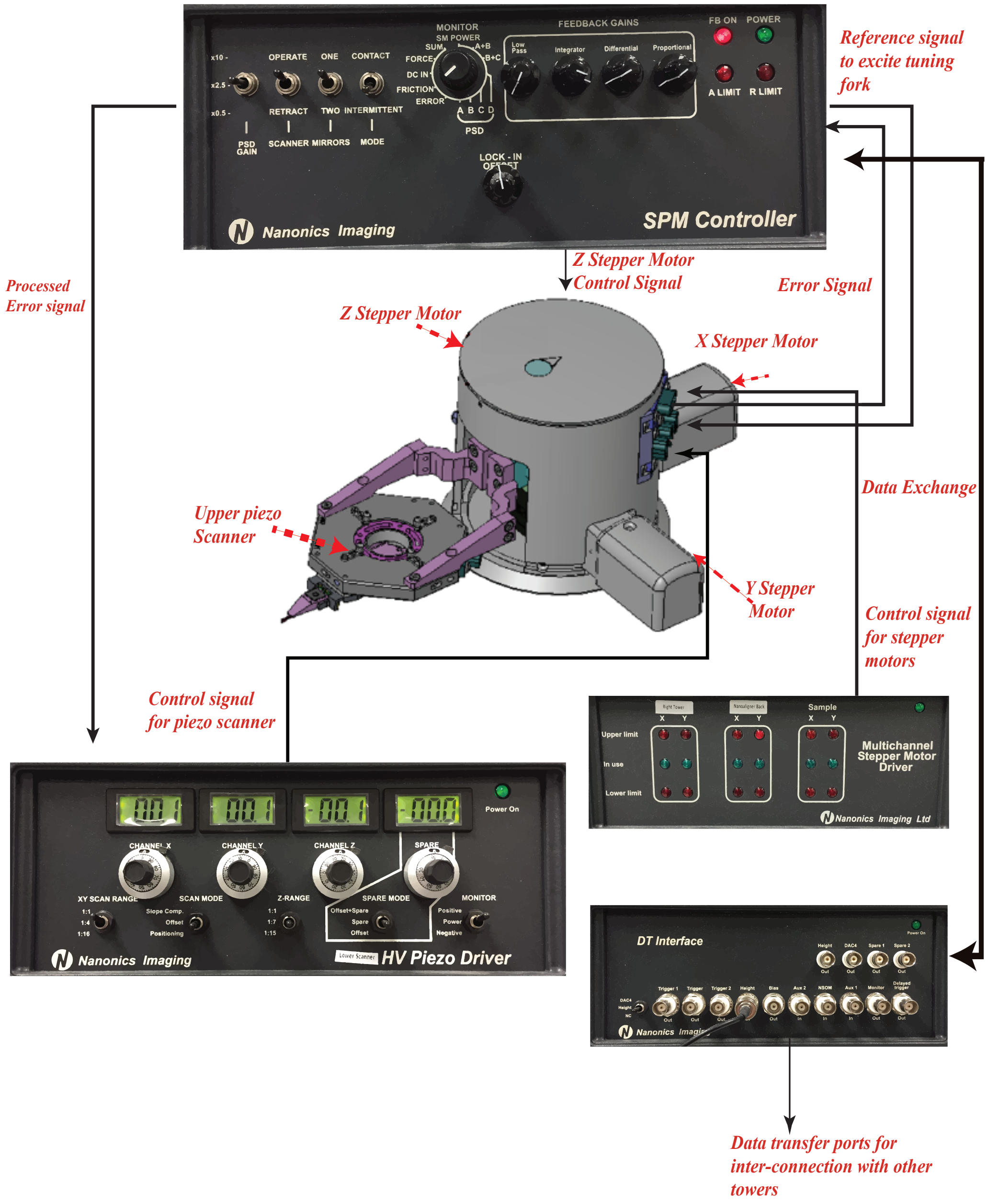

Figure 2.1: System architecture of an individual system

communicate with all of the system peripherals.

Initially when a probe is mounted onto the tower system, lock-in settings are configured in the software for the probe. This ensures that the probe is oscillated at a frequency which corresponds to the resonance frequency of the tuning fork probe. Zero to 5V p-p amplitude voltage is used to excite the tuning fork with a maximum resolution of up to 0.2 mV. For a scanning operation, the probe is positioned to a point of interest by using the stepper motors. The movement of the probe in X-Y directions are performed using the stepper motor control software running on the system computer. The Z-axis movement of the probe tip is controlled by both Z stepper motor and piezo actuators based on the signals obtained from probes oscillations. While the probe is oscillated at a fixed frequency by the built-in lock in controller, any physical perturbations to this oscillation is detected as a change in either amplitude or the phase of the oscillation of the tuning fork. As a result, the error signal is obtained. The built-in Direct Digital Synthesizer (DDS) system is used to generate probe oscillations and lock-in adjustments. The DDS system uses three independent generators with 32-bit resolution frequency determination and 20-bit phase determination. Two of these generators provide quadrature for lock-in processing and the third generator is used for exciting the tuning fork with an autophase algorithm. The system uses a clock frequency of 20 MHz and it has stability of 5 ppm (i.e. a long term stability measurement unit ppm-part per million means that over a 1ms interval the clock period can change by 5 ns) with a resolution of $<$ 5mHz. An FPGA based PID feedback controller is built in the SPM

Controller system that processes the error signal and sends it to the High Voltage (HV) Piezo driver system.

High Voltage (HV) Piezo driver system is responsible for precise control of piezo actuators integrated into the system. The piezo actuators are built-in inside scanner units and exist as upper or lower piezo scanners. These actuators manage sub-nanometer resolution movement of the probe based on the error signal obtained from probe oscillations. The error signal can be based on either the amplitude of the probe oscillation or the phase. This is determined during the lock-in settings inside the controller software, by the user.

Data Transfer (DT) Interface box provides a hardware interface for data exchange between the other systems. It contains 16-bit resolution Analog to Digital Converters (ADC) and 16-bit Digital to Analog Converter (DAC), that provide an interface between the Data Translation cards for control PCs and the SPM controller system. Data Transfer Interface box is also capable of generating/accepting digital synchronization input or output for triggering external devices.

Various external devices can be integrated into single system through these data transfer interface ports. There are a total of 14 terminals on the interface of data translation box. Ten of these are output terminals to send out the signal to external hardware units and four of them are configured as input terminal to accept the data from other systems for intercommunication.

The fine movements of the probe are performed using the upper piezo scanner. This is used for probe scanning and has a range of 30 μm (XYZ), a resolution of $\leq$0.05 nm in Z direction and $\leq$ 0.15 nm in XY directions. In addition to upper piezo scanners, as an independent scanner from tower systems, the lower piezo scanner holds the samples and can independently move specimens, it has a range of 80 μm (XYZ) and a resolution $\leq$ 0.05nm in each direction.

Figure 2.2 shows a closer look at tuning fork type probes used in MV 4000 multi-probe SPM system. The probe tines have approximately 4.5 mm length, 1.2 mm width and 0.25 mm thickness. Each tuning fork is fabricated out of quartz (a piezoelectric material) and metallic films are deposited on each prong of the fork in order to apply electrical voltage and oscillate the probe. The tuning forks are excited with 5V amplitude oscillator. By the electric connections to each prong, the signal is transferred to an electro-block positioned under the upper piezo scanner and amplified here. The amplified signal is carried to SPM controller system in order to be further processed. Based on initial lock-in settings determined by the user and the type of the feedback (either Amplitude or Phase feedback), an error signal is generated. The processed error signal is transfered to HV Piezo system, in order to create high voltage signals to be able to actuate piezo scanners and keep precise feedback contact.

Depending on the type of the application, various types of probe tips can be mounted on the prong of the fork. These might include cantilevered or straight glass probes as shown in Figure 2.2. The tip radius, shapes and the cantilever length can be precisely controlled by the laser glass pulling technology that are used to manufacture these tips [11]. Unlike conventional AFM cantilevers which are usually fabricated out of silicon, these probes do not obscure the objective view through microscope and brings a spatially and optically friendly probe setup.

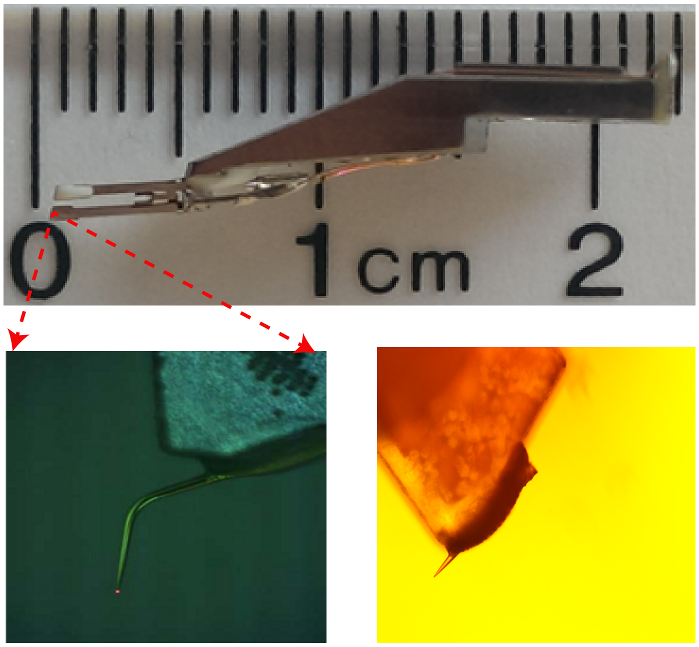

Figure 2.2: A closer look at tuning fork probes used in the system

Figure 2.3 provides a representative schematic showing the integration of multiple systems inside Multi-probe MV-4000 SPM tool. There are four tower systems and a lower scanner system as it can be seen in the setup. The number of tower systems can be increased according to the user requirements and specifications of the application. Each of the tower system includes the above mentioned subsystem components in Figure 2.1. Intercommunication between the systems is provided via DT Transfer interfaces and physical electrical signals are transferred by using coaxial BNC cables. For example, the height signal of a tower can be distributed to the rest of the tower systems and cooperative tasks can be performed by this means.

The lower scanner system which is positioned in the middle of the towers is a 3D piezo scanner that holds the samples. It is controlled in a similar way to the tower system and has its own HV piezo driver system. The sample scanner can be combined into operation with any of the tower system and can use the corresponding towers SPM controller. A low voltage adapter box is used to select between whether a tower systems piezo scanner or the lower system scanner will be used during the operation. It is also possible that the lower scanner and the upper scanner can share the scanning operations by working in tandem. For example, a Z-axis movement of the tip can be operated by only the lower scanner and X-Y scanning of the tip can be operated with the upper scanner. Different combinations can be obtained by adjusting the settings in the low voltage adapter.

Each of the tower can be independently operated. The towers are enclosed within an acoustic chamber in order to eliminate environmental noise. The scanning systems sit on top of an anti-vibration table to eliminate possible physical vibration noise into the precise operation of the system.

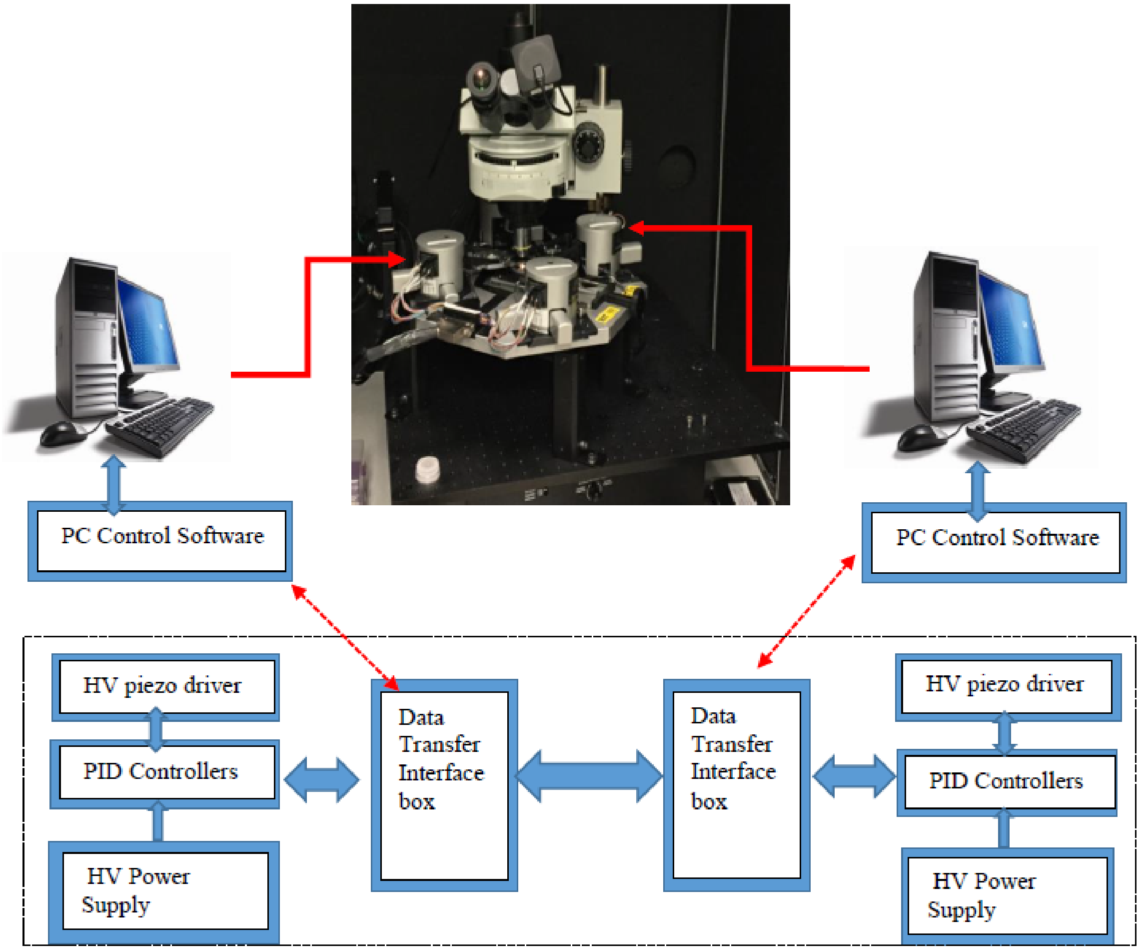

Figure 2.3: Diagram showing the connectivity between other systems

In this system tuning forks are used as scanning probes which are known to be high quality resonators. Figure 2.4(a) and 2.4(b) present the examples of AFM probe's frequency response curves. As the figures indicate, the tuning fork probes have a very sharp resonance curve and can oscillate at high frequencies. This makes it possible to obtain a very sensitive error signal and establish a closed-loop feedback control with a high accuracy. Depending on the application, it is possible to configure the system to be able to work in either amplitude or phase feedback error based on tuning fork's oscillation. Considering the rapid change of the phase as shown in Figure 2.4(b), a phase feedback is more sensitive as compared to the amplitude feedback. By the help of built-in lock in controllers, it is possible to monitor both the amplitude and the phase of oscillations, independently. When the phase feedback is used, the amplitude of oscillation can be independently monitored.

Using data transfer ports, information such as the error signal, height of the probes, force or friction generated for each probe can be transferred to other systems through auxiliary input terminals.

In addition and as per the requirement, other systems and sensors such as different types of detectors (Photo detectors, counters, CCDs), laser sources, nanoalignment and test measurement tools can be integrated into the system. This full integration capability comes from the whole system's flexible design and interoperability. Further details of the system operation are given in Appendix A.

In the next chapter, the novel multi-probe nanoindentation system that is

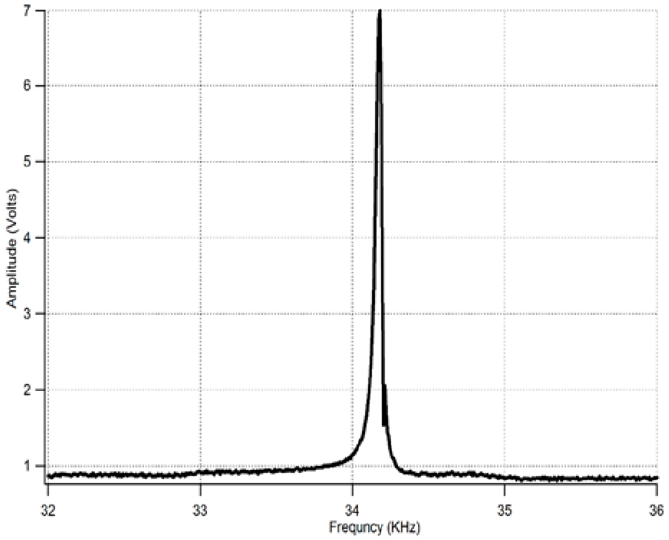

(a) Amplitude vs. Frequency response

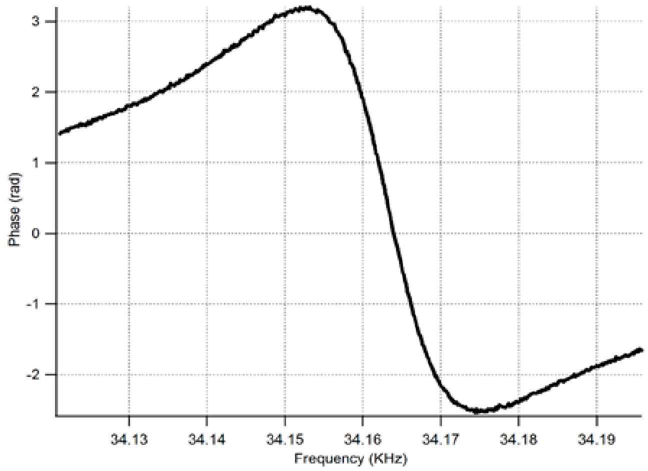

(b) Phase vs. Frequency response

Figure 2.4: An example resonance response of AFM probes used in the experiments

developed in this dissertation work is presented in detail together with the experimental results showing the viability of the new technique.

Chapter 3

Development of a novel multi-probe nanoindentation system

3.1 Introduction

The major problems and error sources encountered during nanoindentation experiments were addressed in detail in chapter 1. These include cantilever bending errors when standard AFM systems are used, zero-level contact detection problems, jump-to-contact artifacts, as well as sensor resolution limitations in depth sensing.

Addressing the above mentioned problems, significant research has been devoted to the design and the development of tools that will improve the accuracy of the obtained experimental data and yield a more accurate estimation of material properties by nanoindentation. Evan et al. report the development of a tool specifically designed for nanoindentation on compliant materials considering the surface detection problems of commercially available nanoindentation devices [13]. Nowakowski et al. demonstrate a nanoindentation system with a high precision where capacitive gauges are used for displacement measurement in the system [14]. The proximity of the indenter to the surface is sensed by tuning forks through their frequency response shift, showing the capabilities of accurate point of contact detection measurement of tuning forks. Oiko et al. recently demonstrated a development of nanoindentation probe that can be manipulated inside a scanning electron microscope (SEM) [15]. This system also utilizes tuning-fork technology which can be used as an ultra-sensitive force sensor owing to the fact of very high quality factors of tuning forks. They perform *in-situ* nanoindentation experiments on multi-walled carbon nanotube bundles however, the displacement data are only obtained from the SEM images limiting the high accuracy of displacement reading and the true depth sensing during nanoindentation. Zhao et al. present a nanoindentation device which is designed to operate inside an SEM chamber in order to perform *in-situ* indentation tests of Indium Phosphide [16].

In this chapter, a novel approach by a multi-probe scanning probe microscopy (SPM) system utilizing tuning-fork probe technology is reported in an effort to overcome the limitations and problems of current nanoindentation systems and provide a strong tool for our material characterization research for MEMS.

Instead of relying on the displacement of a cantilever measured by optical means, our approach uses a secondary AFM probe which is kept in closed-loop feedback contact with the indenter probe. This gives ultra-sensitive and high resolution capability in terms of true depth sensing during nanoindentation. With this approach, only the Z-axis motion of the straight indenter is monitored, independent of any possible tuning fork bending that may occur in spite of very large spring constant of tuning forks ($>$ 2600 N/m) [17]. During nanoindentation through the specimen, since the positioning of tuning forks is controlled with phase feedback, the point of contact can be determined with a great accuracy as compared to other nanoindentation tools. This also brings an advantage to the experimentally obtained data and overcomes the major problem such as discussed in [18] and [5].

In the next section, a theoretical background on nanoindentation is given to the reader. Widely used contact models such as the Hertz model and Oliver-Pharr model are introduced. These are employed in estimating the elastic properties of the materials from the experimentally obtained data.

3.2 Theoretical background on nanoindentation

The most fundamental and the simplest model used in nanoindentation experiments is the Hertz model [19]. The original Hertz problem examines the elastic deformation of two solid spheres (with Radii R_1 and R_2) as shown in Figure 3.1(a) that are in contact and one of them is pressed into another presented in Figure 3.1(b). When two spheres are pressed into each other with a force $F_{applied}$, an elastic deformation occurs with a circular contact area that has radius a and a depth δ that can be defined as in eq. 3.1 and eq. 3.2

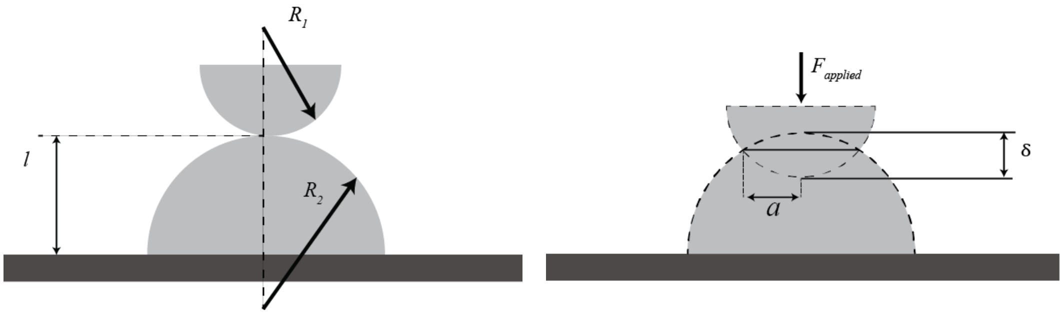

(a) Original representation of Hertz contact problem

(b) Elastic deformation when a force is applied over to the sphere

Figure 3.1: Schematic representation of Hertz contact model

$$a = \left(\frac{3F_{applied}R_{eff}}{4E^*}\right)^{1/3} \tag{3.1}$$

$$\delta = \left(\frac{9F_{applied}R_{eff}}{16\left(E^*\right)^2}\right)^{1/3} \tag{3.2}$$

Where R_{eff} and E^{*} are effective radius and effective modulus, respectively defined in eq. 3.3 and 3.4.

$$\frac{1}{R_{eff}} = \left(\frac{1}{R_1} + \frac{1}{R_2}\right) \tag{3.3}$$

$$\frac{1}{E^{*}} = \left(\frac{1-(\nu_1)^2}{E_1} + \frac{1-(\nu_2)^2}{E_2}\right) \tag{3.4}$$

The variables ν_1 and ν_2 are Poisson's ratios of the indenter and the substrate, respectively. For elastic deformation on flat substrates that is assumed to be infinitely long as compared to the indenter, the problem can be reduced into an equivalent geometry as seen in Figure 3.2. Based on eqs. 3.1-3.4, one can calculate $F_{applied}$ as given in eq. 3.5

$$F_{applied} = \frac{4}{3}\delta^{3/2}R_{eff}^{1/2}E^{*} \tag{3.5}$$

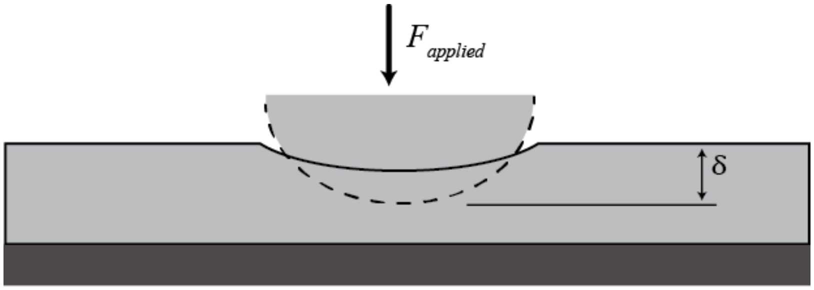

Figure 3.2: Equivalent geometry representation of Hertz contact model for a flat substrate

If the indenter's geometry and elastic modulus are known, one can use eq. 3.5 in order to fit a force-distance curve obtained from nanoindentation experiments and estimate the elastic modulus of substrate that is being under the investigation.

The Hertz model has several assumptions such as $E_{surface} << E_{tip}$ and $\delta << R_1$. In addition, it assumes that all of the deformation during nanoindentation is elastic and there is no plastic deformation on the substrate. However with most of the hard materials, during nanoindentation one can also observe plastic deformation. For this type of nanoindentation experiments, Oliver-Pharr (OP) model is the model that is widely used [20].

Once a force-distance curve is obtained, by using OP model, one can extract elastic properties such as elastic modulus and hardness of materials. Figure 3.3(a) shows a typical force-distance curve when nanoindentation includes a plastic deformation. In this curve, loading part includes both elastic and plastic deformations. However, during unloading it is assumed that only elastic deformation occurs. Therefore, stiffness can be approximated with the slope of unloading curve as shown in Fig 3.3(a). If unloading curve is fit to a power law such as $F = \alpha\left(h - h_f\right)^m$ where α and m are power law fitting constants then unloading stiffness S can be approximated as in eq. 3.6 by the slope of the fitting.

$$S = \left.\frac{dF}{dh}\right|_{h=h_{max}} \tag{3.6}$$

Figure 3.3(b) shows the important parameters during nanoindentation process. In these figures, h_c is the amount of the depth where contact is made between indenter and substrate, h_s is the amount of sink-in of the material during indentation, and h_f is the final depth of penetration that is left on the surface after nanoindentation is completed. Once a force curve such as given in Figure 3.3(a) is obtained, one can calculate elastic unloading stiffness by eq. 3.7 defined as the slope of upper part on the unloading curve as shown in Figure 3.3(a) [20].

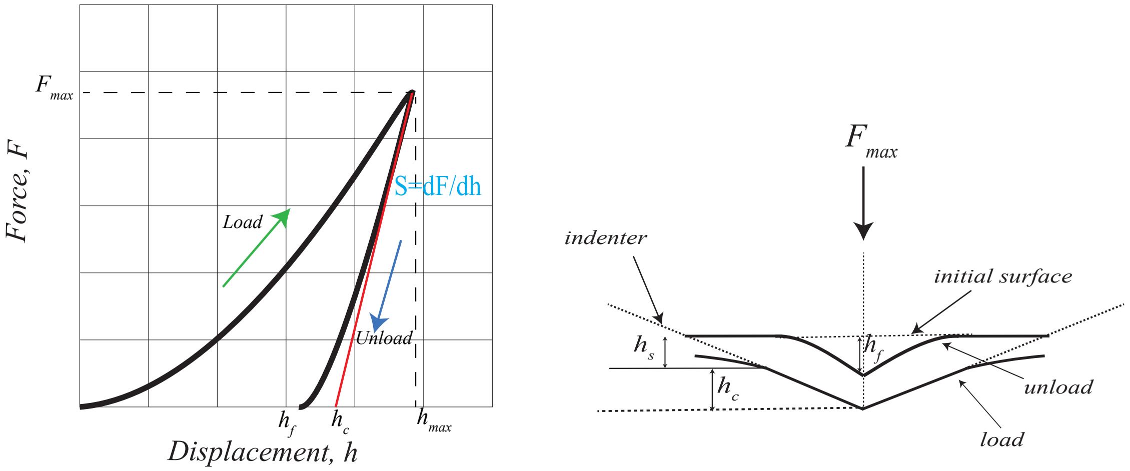

(a) a representative force-distance curve for Oliver-Pharr model

(b) Schematic illustrating loading and unloading process

Figure 3.3: Schematic representation of OP model

$$S = \beta \frac{2E_{eff}\sqrt{A_c}}{\sqrt{\pi}} \tag{3.7}$$

where E_{eff} is effective Elastic modulus including both indenter's elastic modulus (E_1) and sample's elastic modulus (E_2). It can be expressed as given in eq. 3.8. In the eq. 3.7, β is a correction factor that accounts for lack of axial symmetries for the indenter. It has been shown by Oliver and Pharr that $\beta \cong 1.07$ worked for most of the materials.

$$\frac{1}{E_{eff}} = \left(\frac{1-(\nu_1)^2}{E_1} + \frac{1-(\nu_2)^2}{E_2} \right) \tag{3.8}$$

The projected contact area of elastic contact, A_c in eq. 3.7 depends on both indenter's tip geometry and the depth of contact, h_c. It is possible to establish a mathematical formula for the area function such as $A_c(h_c)$ based on the indenter's specific tip geometry.

Once a force-distance curve is obtained such as shown schematically in Figure 3.3(a), one can calculate the stiffness parameter S from the slope of the unloading part and use eq. 3.7 and eq. 3.8 to extract sample's unknown elastic modulus (E_2). This is very powerful in terms of estimating elastic modulus of a material. However, it requires an accurate force-displacement curve. Thus, a system that creates accurate height and force readings is crucially needed. In the next subsection, we present our novel nanoindentation system which creates very precise force curves and allows us to calculate elastic modulus more accurately with high confidence.

3.3 The Novel Nanoindentation System

The experimental setup demonstrating the multi-probe nanoindentation technique is presented in Figure 3.4. For nanoindentation experiments, a diamond probe with a cube-corner geometry (MicroStar Technologies) is mounted vertically with a micromanipulator under the microscope onto the lower tine of the tuning fork (Nanonics Imaging Inc.). Indentation depth is measured by the second tower with a specifically fabricated cantilevered AFM glass probe tips coated with Cr. These probes have a cantilever length of 300 μm and 20 nm tip radius, and they are mounted onto the lower tine of the tuning forks.

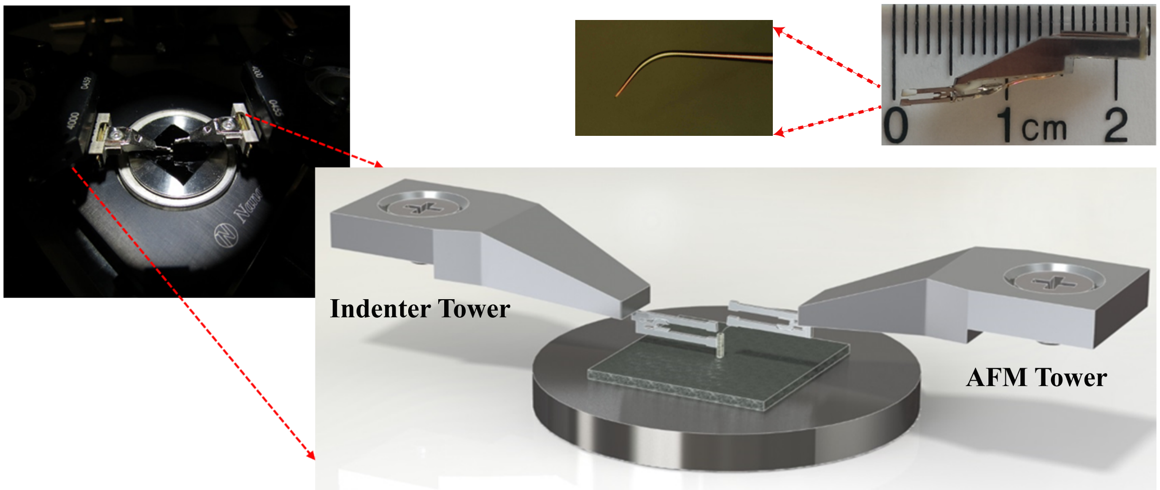

Figure 3.4: Experimental setup demonstrating the proposed two probe nanoindentation technique

An example image of cantilevered AFM tips is also shown in Figure 3.4. The material under investigation is placed on a flat sample holder on to the lower piezo-scanner. Initially, the left hand side probe (indenter tower probe) is moved down towards the sample by the Z-stepper motors while phase feedback error signal is monitored continuously. This means that the feedback is based on the change of the phase signal from the tuning fork. Contact of the tip with the sample is observed immediately with a change in error signal, at which point the stepper motion stops. Subsequently, the lower scanner is retracted by a safe distance amount ($\sim 3\mu$m). After this, by the help of the piezo scanner's fine movement capability, the sample is brought up automatically to ensure a very accurate contact positioning and a safe approach. Once the indenter probe is in feedback with the sample surface, the diamond probe is held in that state and the second probe on the right hand side (AFM tower probe) is placed on top of the diamond probe. Once the contact is established for both probes, nanoindentation experiment is started. A closer look at the positioning of the two probes that was given in Figure 3.4 is shown in Figure 3.5.

For nanoindentation experiments, the indenter probe oscillation is disabled and the desired sample displacement value is set. For example, for a target of 100 nm displacement, the programmed sample scanner first retracts the sample 100nm and then pushes toward the indenter probe 200nm. The displacement of the indenter is monitored with the AFM probe which is oscillating and kept in phase-feedback. In our proposed system, the depth

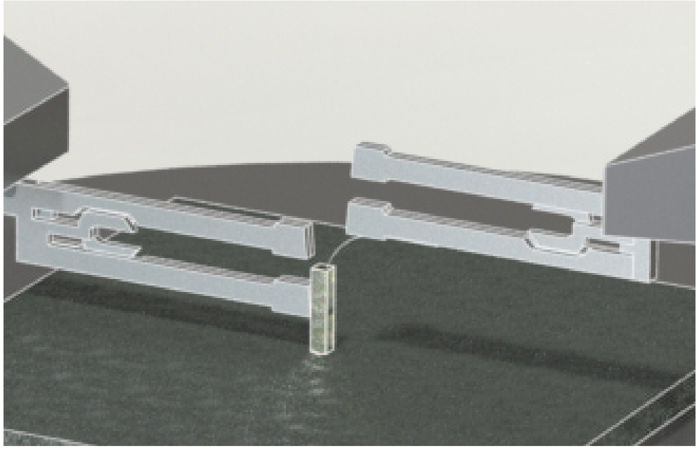

Figure 3.5: A closer look at the probe positioning for multi-probe nanoindentation approach

sensing is performed with an AFM probe which is in phase-feedback with the top of the diamond indenter probe. The AFM probe's height is controlled with a piezo scanner head which has a very high resolution($<$0.05 nm) due to highly oriented piezo materials used in the folded-piezo flexure scanner design. This also brings the best achievable resolution to our nanoindentation experiments in terms of depth sensing. In addition, since the AFM probe continuously monitors the Z-axis displacement of the indenter probe, only changes in Z motion are sensed with a very high accuracy of point of contact while the X and Y motion are ignored.

Calibration on the height signal is performed with a calibration grid (BudgetSensors) that includes both 115 nm micropillar and microwell arrays on a silicon chip. The step height of the features on the chip is measured and verified by using both contact profilometer and SEM measurements.

Figure 3.6(a) shows an example of experimental data where the AFM probe is continuously measuring and following the z-axis movement of the sample holder (lower piezo scanner) when the probe is in feedback. This measurement is performed by programming the piezo stage to move ± 200nm. When the movement starts, the piezo stage retracts from its initial position 200nm and gradually moves up for a total displacement of 400nm. As it can be seen from the figure, the AFM probe follows the stage movement, accurately. This shows that both the piezo stage movement and the AFM feedback movement are well calibrated.

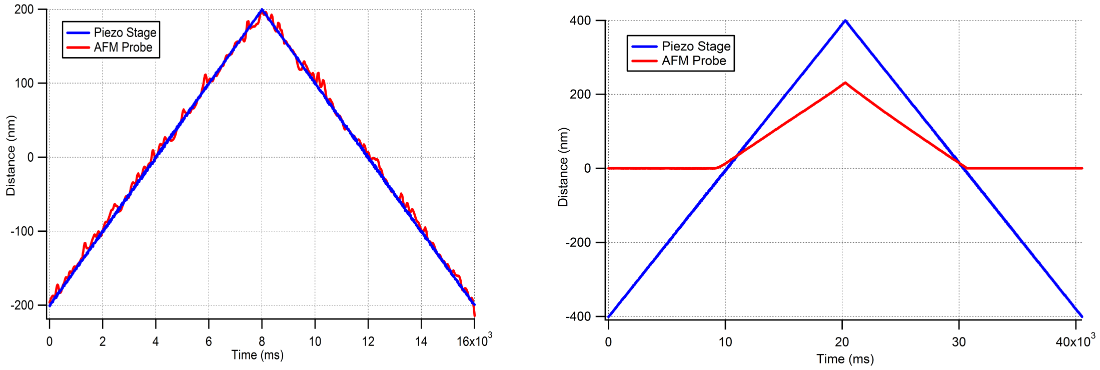

(a) Experimental data showing the AFM probe following the Stage

(b) Experimental data showing AFM probe following the indenter probe on a fused silica sample

Figure 3.6: Experimental data showing AFM probe measurements on the stage and on top of the diamond indenter for a fused silica sample

Figure 3.6(b) shows the data collected during a multi-probe indentation experiment on a fused silica sample. Initially, the diamond probe approaches the surface in phase feedback. When the contact is detected based on phase error signal, the approach is stopped automatically. The PID gains are then re-adjusted so that the error signal stays at zero with minimum deviation when the probe is in contact. After this, the AFM probe's approach is initiated to the top of the indenter. Similarly to the indenter probe, the AFM probe is operated in phase feedback mode. When contact is established with the indenter probe, the approach is stopped automatically and PID settings are adjusted so that the AFM probe will remain in contact at all times and will just follow the movement of the indenter. After the contacts for both probes are established, the configuration of the stage movement in the software is performed. In Figure 3.6(b), the stage is programmed to move ± 400nm. When the indentation process is started, the stage retracts 400nm first and then moves towards to the indenter. During the motion of the sample stage towards the indenter, the indenter probe oscillations are turned off and the indenter probe is no longer in feedback. The second set of data in red shown in Figure 3.6(b) is the displacement data read from the AFM probe during the indentation process. Note that the AFM probe reflects only the true z-axis movement of the indenter probe unlike the conventional AFM systems where the measurement relies on laser deflection of the cantilever itself which includes a convolution of X and Y motion into the laser deflection reading.

As it can be seen from Figure 3.6(b), as the piezo stage starts pushing up the sample towards the diamond indenter, the AFM probe's reading starts to go up as well and when the sample starts moving away from the diamond tip, the AFM probe reading starts going down and settles at position zero when the sample and the indenter are separated.

For the force level calculations, the spring constant of the tuning fork can be calculated from the beam formula as given in eq. 3.9.

$$k_{beam} = E_{quartz} \frac{w}{4} \left(\frac{t}{L} \right)^3 \tag{3.9}$$

where w and t are the width and the thickness of the free prong, respectively and L is the length of the prong. E_{quartz} is elastic modulus of quartz material of which the tuning forks are fabricated. Several studies have found this formula to be inaccurate and underestimate the spring constant of the tuning forks by a significant amount, even up to an order of magnitude [21], [17]. One reason for this is that the tip (diamond indenter in our case) is rigidly fixed at the end by epoxy glue and this might alter the effective dimensions of the free beam. Therefore, further investigation of the spring constant calculation based on this model is necessary.

We derive the effective spring constant of the indenter tuning fork by calibrating against a sample with known modulus. Based on the formula given in eq. 3.9 and a bare tuning fork's dimensions, the spring constant is calculated as $2600\ N/m$. Firstly, an indentation experiment is performed on a fused silica by using $k_{fork} = 2600\ N/m$. Then, Oliver-Pharr (OP) model is utilized to match the experimental data to the known elastic modulus of fused-silica sample 69.3 GPa [20], [22]. Fitting of the data over 10 different force curve measurements with an average modulus of 69.38 GPa yields a spring constant $k_{fork} = 4992\ N/m\ (\pm 264.11)$. One of the force-distance curves used in OP model fitting is given in Figure 3.7.

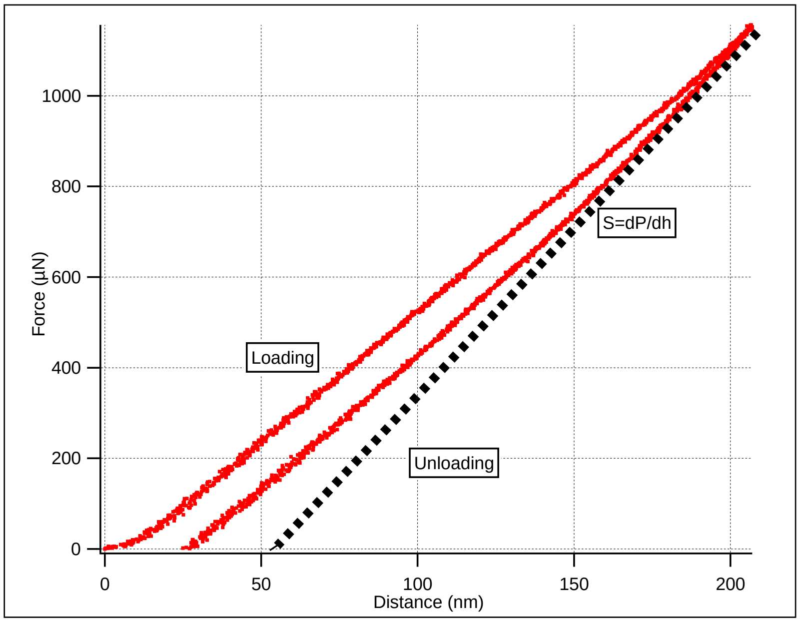

Figure 3.7: Fused Silica Force Distance Curve

Table 3.1 tabulates the calibration experiment results on the fused silica sample. Where h_{max} represents the maximum depth of penetration and $K_{calibration}$ is the spring constant value of the indenter tuning fork that is assumed in order to get the target elastic modulus value.

Figure 3.8 demonstrates the distribution of spring constant values with respect to depth of penetration during fused silica calibration experiments.

Table 3.1: Experimental data obtained during calibration of k_{fork} on the fused silica calibration sample

h_{max} (nm)	$K_{calibration}$ (N/m)	Estimated Modulus (GPa)
113.8	4850	69.6
157.6	5041	69.32
159	5041	69.47
159.4	5034	69.32
159.9	4490	69.38
160.6	5180	69.31
161.3	5175	69.29
165.5	5450	69.35
170.3	4620	69.4
206.98	5035	69.35
mean (std)	4992 (± 264.11)	69.38 (± 0.09)

The mean value of the spring constant is shown with a dotted line at 4992 N/m.

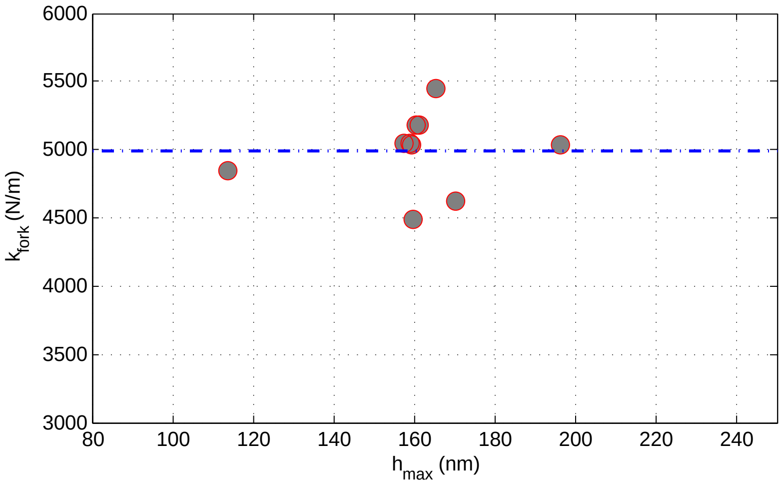

Figure 3.8: Spring constant vs maximum depth of penetration

To further verify the spring constant calibration and the force values for the rest of the experiments, finite element (FE) simulations have been performed as shown in Figure 3.9. In the simulations, the diamond indenter is pressed into the fused silica reference sample incrementally up to 10 nm depth of penetration in order to ensure that the results stay within the elastic regime. During the simulation, reaction forces on the surface of the indenter tip are evaluated showing that force levels for both experimental and simulation data are in a good agreement when k_{fork} is 4992 N/m. The variation among between data points is due to feedback oscillation where AFM probe is in constant feedback contact with the top of the indenter. This can be further minimized with fine-tuning of PID feedback gains in the system. In order to perform error analysis, Comsol simulation results are fit into a polynomial curve of forth order ($y = 0.0011x^4 - 0.00337x^3 + 0.3669x^2 + 0.5618x - 0.0061, R^2 = 1$) and compared with respect to experimental data. The calculated root mean square (RMSE) is 3.0607. Due to the simulation software limitations and in order to keep the deformation within the elastic regime, only the small amount of indentation can be simulated up to 20nm depth of penetration.

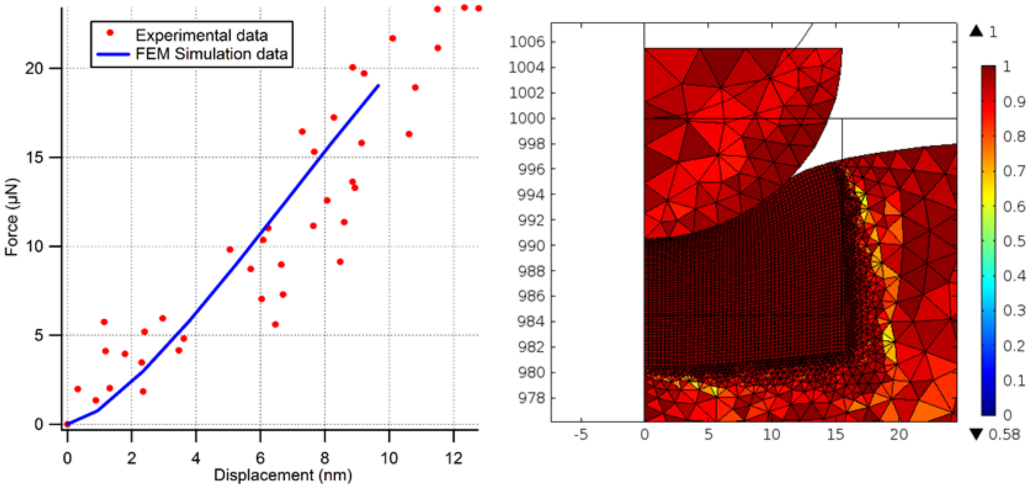

Figure 3.9: Finite element analysis data as compared to experimental data. Calculated root-mean-square-error (RMSE) 3.0607

Figures 3.10(a) and 3.10(b) show the characteristics of the cube-corner geometry diamond indenter tip used in our nanoindentation experiments. Figure 3.10(a) is obtained from an AFM scanning with the AFM tower and shows the cube-corner shape of the tip. Figure 3.10(b) is an TEM image of the tip showing the radius of curvature in nm.

In the next section, we present results in regards to estimating elastic moduli of hard materials using the spring constant calculated in this section.

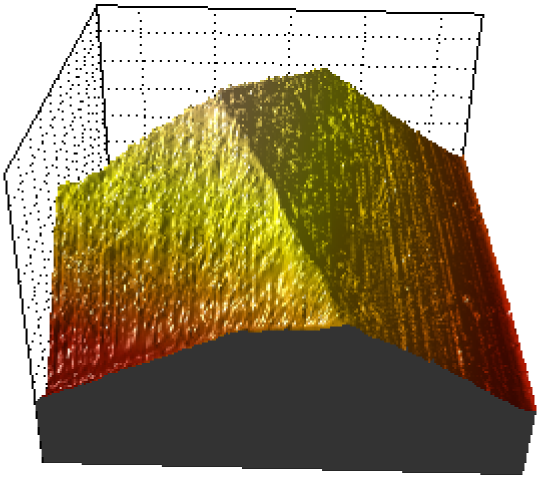

(a) A 3-D representation of AFM scan for the cube-corner diamond tip used in nanoindentation experiments

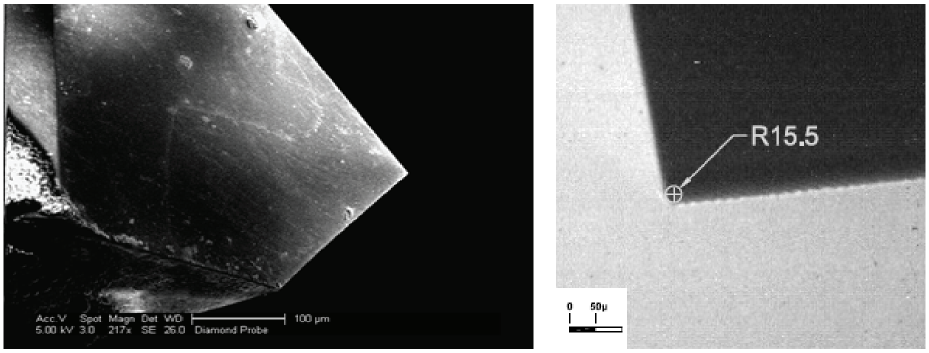

(b) SEM and TEM images of the diamond tip. The tip radius is measured as 15.5 nm

Figure 3.10: Images of cube-corner diamond tip used in nanoindentation experiments

3.4 Results

In the previous section, we have introduced the overall system components and the details of our proposed technique together with the calibration results. In this section, we present the nanoindentation results on different materials and our estimations based on the experimentally obtained data.

Figure 3.11 includes the force-distance curves with varying loads measured on silicon (100). The varying loads correspond to the programmed stage movements from 100 to 300nm. Within these experiments, the stage moves with a speed of $0.04\ nm/ms$. The maximum force increases from 445 μN to 1004 μN.

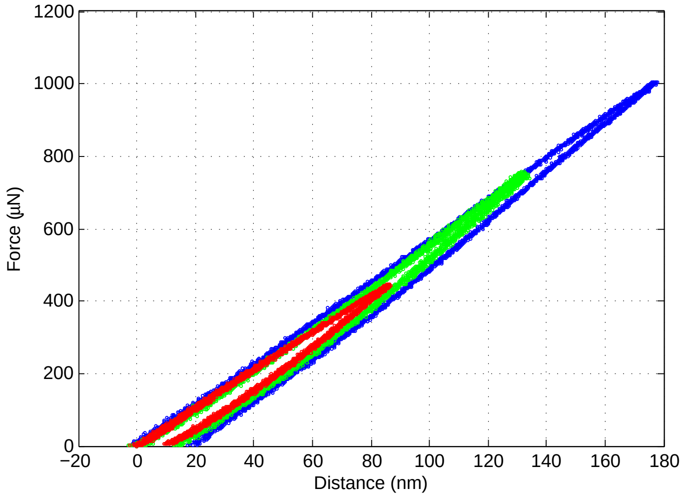

Figure 3.11: Force Distance Curves on Silicon Substrate

Figure 3.12 shows an example of a power law fitting of the unloading data from a silicon force-distance curve obtained experimentally. The fitting parameters $\alpha = 0.6668$ and $m = 1.4668$ fall within the expected ranges as listed in the OP model with an RMSE values of 5.1241 [20].

An AFM topographical image of indentation on silicon substrate is shown in Figure 3.13 together with its height profile. It shows quantitatively a residual indentation mark of the cube corner indenter tip at a depth of 27.5 nm. The topography of the residual mark that is constructed by an AFM

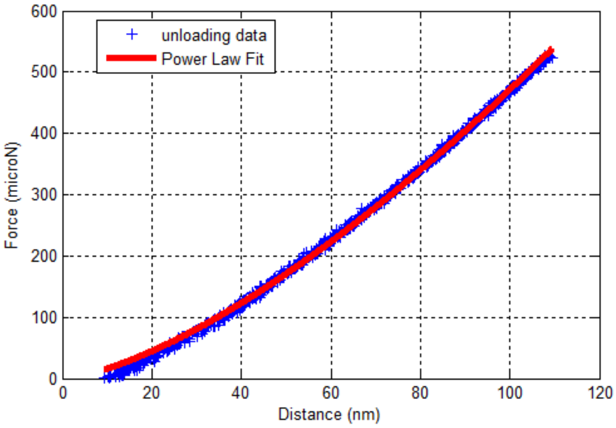

Figure 3.12: Power law fitting to the unloading part of a silicon force-distance curve RMSE=5.1241

scan suits well with the cube corner geometry shape of the diamond indenter tip. The depth of indentation mark measured by the scan is also within the range of h_f parameter according to the Oliver-Pharr model.

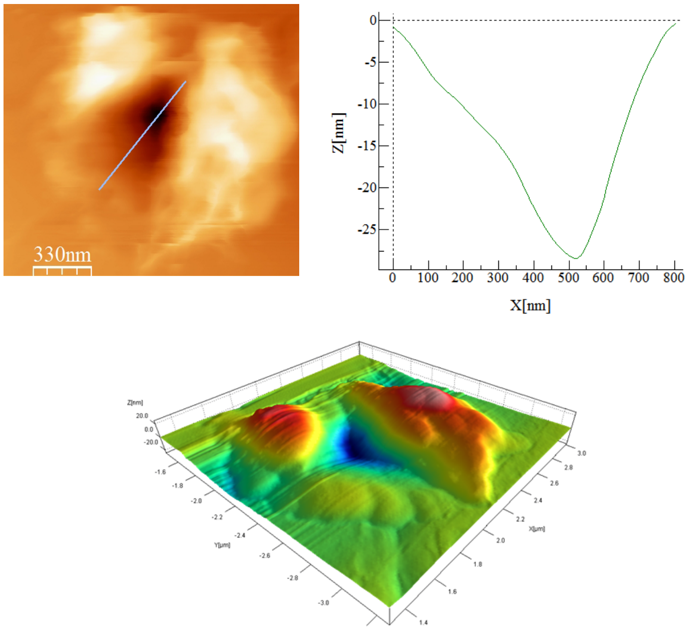

Figure 3.13: Topography and cross-sectional profile of indent on silicon

Figure 3.14 shows the nanoindentation results on a glass substrate (Corning ® Eagle Glass 2000™) with a reported elastic modulus of 70.9 GPa [23]. Varying load conditions similar to silicon nanoindentation experiments are applied during nanoindentation. As it can be seen, the force-distance curves obtained on different load conditions overlap with increasing h_f data points. According to the Oliver-Pharr model, this shows that the more penetration occurs through the substrate by the diamond indenter tip.

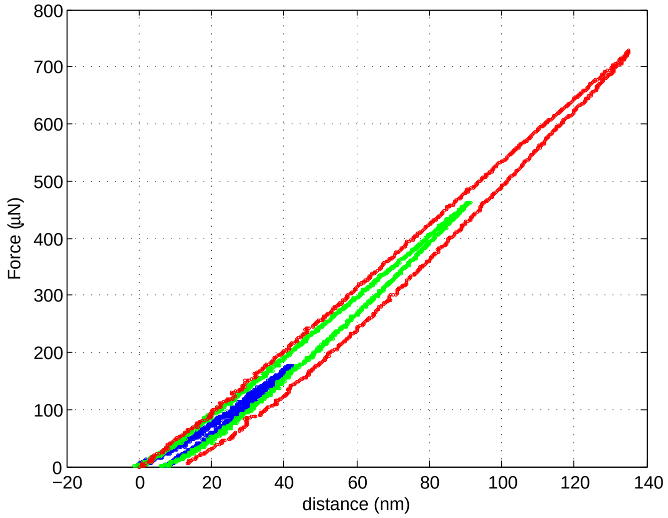

Figure 3.14: Force Distance Curves on Corning Eagle Glass Substrate

Figure 3.15 shows the power-law fitting results on Eagle glass substrate similarly to Figure 3.12 for silicon. The fitting parameters are $\alpha = 0.3359$ and $m = 1.4705$ with an RMSE value of 8.7804 fall within the expected ranges as listed in the OP model [20]. Based on the stiffness calculations according to the OP model and utilizing the tip characteristics, an average elastic modulus estimations of 67.83 GPa is obtained over 10 different set of experimental results.

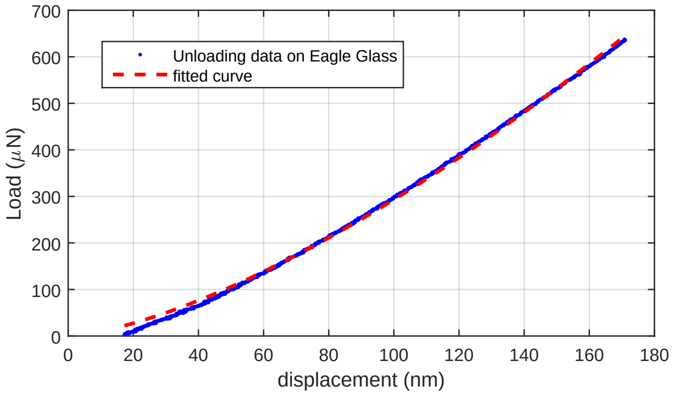

Figure 3.15: Power law fitting to the unloading part of an Eagle glass force-distance curve RMSE=8.7804

In addition to silicon and Eagle glass results, in Figure 3.16 we present the results on fused silica sample. Varying loading conditions are also applied by programming the stage for displacements ranging from 100 nm to 300 nm. The force-distance curves line up similarly to our silicon and fused silica sample results and h_f parameter increases based on increasing loading conditions.

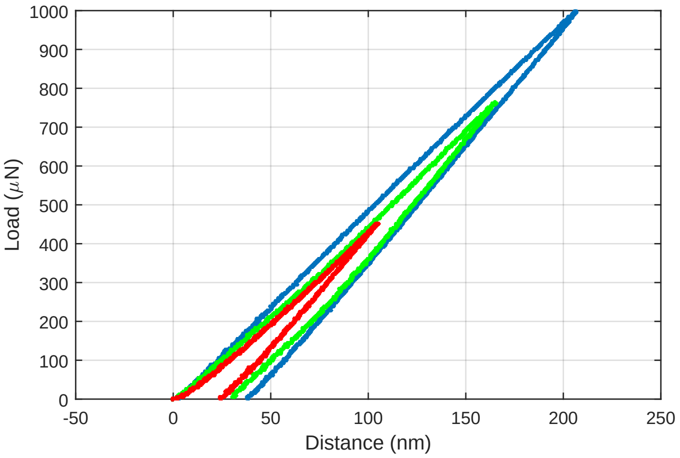

Figure 3.16: Force Distance Curves on fused-silica Substrate

Figure 3.17 demonstrates the power law fitting to unloading data on one of the experimental results for the fused silica sample with power law fitting parameters $\alpha = 0.1877$ and $m = 1.4680$ with an RMSE value of 15.0478. Based on the stiffness calculations given in eq. 3.6 and other OP model parameters, the average calculated elastic modulus is 69.38 GPa. The mean value is obtained over 10 set of experimental results.

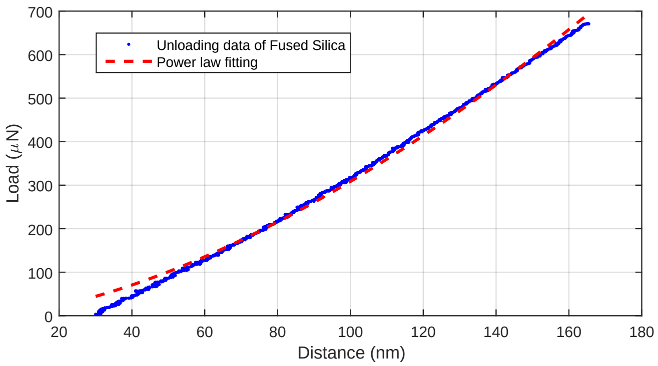

Figure 3.17: Power law fitting to the unloading part of a Fused silica force-distance curve RMSE=15.0478

Table 3.2 shows the properties of the materials used in nanoindentation experiments in our study and their corresponding material properties reported in the literature.

Table 3.2: Reported properties of the materials used in nanoindentation experiments

Materials	E(GPa)	Poisson Ratio	Ref
Si (100)	169	0.22	[24]
Fused Silica	69.3	0.17	[22]
Eagle Glass	70.9	0.23	[23]
Diamond (tip)	1150	0.07	[20]

In our calculations, the area function is taken as $A(h_c) = 2.598001h_c^2$.

This is generated by considering the physical measurements on the tip and the geometric calculations of the cube-corner indenter as suggested by the diamond-tip manufacturer's data sheet.

Table 3.3 presents the summary of experimentally obtained elastic modulus estimations of the materials used in this study. Mean and standard deviation values are calculated over 10 different set of experiments for each sample at varying load levels. Compared to reported moduli values in the literature, the values shown in Table 3.3 are in a good agreement.

Table 3.3: Estimation of elastic modulus by Oliver-Pharr fitting and the parameters used

Materials	Estimated Modulus (GPa)	Reported Modulus (GPa)	Oliver-Pharr β Parameter
Si (100)	166.87 ± 27.42	169	$\beta = 1.04$
Fused Silica	69.38 ± 0.09	69.3	$\beta = 1.04$
Eagle Glass	67.83 ± 7.68	70.9	$\beta = 1.04$

Our results show the viability of the presented novel approach in characterization of materials with a high accuracy. The new approach brings ultra-high resolution to nanoindentation experiments in terms of both the force and depth sensing. The second AFM probe monitors only the true Z-axis motion as the straight indenter probe is lifted in the Z-direction. This is a significant improvement over conventional AFM-based nanoindentation experiments that convolute X,Y motion into Z motion with laser-based detection of cantilever motion. Additionally, the high spring constant of the tuning fork gives excellent force sensitivity due to its significantly higher spring constant, quality factor, and ability to track motion through phase feedback.

In addition to an indenter probe and an AFM probe, with the current system up to four probes can be operated and could work in tandem. This opportunity brings other exciting novel applications to our nanoindentation approach. For example, while the two probes are performing a nanoindentation experiment, the third and the forth probe can be used in identifying changes in other material properties. By attaching a conductive Pt nanowire probe tips, the third probe can be used as a voltage source and the fourth probe can be used to measure the current. In this way, electrical nano-characterization of the sample can be performed during nanoindentation. Furthermore, thermoresistive probes can be integrated into the approach to monitor the thermal properties of the material during nanoindentation. Lastly, this novel approach can be integrated into environments where the usage of lasers is not possible as in the case of conventional AFM nanoindentation experiments. The findings from this chapter has been published in the literature given by the reference works [25], [26].

The next chapter focuses on mechanical characterization techniques for soft materials. These are based on dynamic frequency-modulation methods as opposed to quasi-static multi-probe nanoindentation technique developed and presented in this chapter.

Chapter 4

Characterization of soft materials utilizing dynamic nanoindentation technique

4.1 Introduction

Most of the nanoindentation instruments are optimized for a narrow range of engineering materials in the GPa regime and performs poorly when it comes to the characterization of soft materials.

One of the disadvantages of the previously presented quasi-static multi-probe nanoindentation technique is that due to the large spring constant of the tuning fork probes, nanoindentation of very soft material is limited or not possible. Furthermore, in terms of characterization of nanostructured materials, currently available sensor technologies' resolution range might not be sufficient [27]. In order to improve the resolution, instead of quasi-static methods, alternative studies have focused on the detection of force profiles through dynamic operation of oscillating microstructures which is referred to as *dynamic force spectroscopy* [28]. Dynamic force spectroscopy enables high sensitivity force measurements from oscillating structures made from even stiff cantilevers. The force values are obtained from amplitude or frequency shifts caused by perturbations to the resonance of the oscillating structures. Considering that tuning forks have sharp resonance responses and are high quality resonators, it is advantageous to use them in force spectroscopy measurements.

In this chapter, the results of soft material nanoindentation experiments that are performed utilizing a dynamic force spectroscopy technique are presented. Instead of determining the force ranges through static bending of the indenter probe, force information is extracted from the changes of resonance frequency due to perturbations occur between tip and sample.

4.2 Theoretical Background

There are two modes for dynamic force detection from an oscillating structure. One mode is amplitude modulation (AM) and the other one is frequency modulation (FM). For AM mode operation, the force inversion models are utilized to reconstruct a force-distance curve through the change in the amplitude of oscillating structures. Various theoretical inverse models have been developed in order to provide analytical solutions to this inversion. Some of these solutions ([29], [30]) were only valid for small amplitude changes called small amplitude solution and the other models have been developed for both large and small amplitude oscillations called arbitrary solutions [31], [32], [33].

In contrast to amplitude modulation (AM) techniques, frequency modulation (FM) utilizes the change in resonance frequency of an oscillating structure and has more sensitivity as compared to AM mode. Giessibl derived the formula that enables determination of frequency change given the applied forces to an oscillating cantilever for both large and small oscillations as given in eq. 4.1 [34]. In this equation, k is the spring constant of the cantilever, F is the force between tip and sample, ω_{res} is the unperturbed resonant frequency, $\Delta\omega$ is the change in resonant frequency, a is the amplitude of oscillation, and z is the distance of closest approach between tip and sample.

$$\frac{\Delta\omega}{\omega_{res}} = \frac{1}{\pi a k}\int_{-1}^{1} F(z + a(1 + u))\frac{u}{\sqrt{1 - u^2}}du \tag{4.1}$$

In order to obtain force values from the frequency shift in FM mode, equation 4.1 must be inverted. Several studies have worked on this inverse problem and proposed models that were either valid for very small amplitude of oscillation or very large amplitudes [35], [36]. However, employment of any of these models for a nanoindentation experiment where the force levels can vary from very small (nN) levels to large (μN) regime can lead to estimation errors due to the limitations of the models. The long waited accurate formulae for FM mode force estimation that works for arbitrary range of oscillation amplitude is proposed by Sader and Jarvis [28].

Sader and Jarvis developed a physical model that theoretically proves the force exerted on an oscillating cantilever at resonance frequency can be extracted utilizing the change in resonance frequency and amplitude of oscillation by using the formula in eq. 4.2 [28].

$$F(z) = 2k \int_{z}^{\infty} \left[\left(1 + \frac{a^{1/2}}{8\sqrt{\Pi(t-z)}} \right) \Omega(t) - \frac{a^{3/2}}{\sqrt{2(t-z)}} \frac{\mathrm{d}\Omega(\mathrm{t})}{\mathrm{d}t} dt \right] \tag{4.2}$$

where $\Omega(t) = \Delta\omega(z)/\omega_{res}$ and ω_{res} is unperturbed resonance frequency of the tuning fork, $\Delta\omega(z)$ is the change in resonance frequency, k is the spring constant, a is the amplitude of oscillations, and z is the distance of closest approach of tip. When the integral is calculated numerically using this equation over the change of tip displacement parameter t, one can correlate the changes of the resonance frequency into force values.

The self-oscillating tuning forks formed out of quartz material has very sharp resonance curves as it was shown in Figure 2.4(a). These probes can have a very high quality of resonance (Q factor) and can be utilized in ultra-sensitive force measurements through FM as it was proved by the Sader's formula in eq. 4.2. Having much higher quality factors as compared to conventional AFM cantilevers also enables tuning fork probes to be used in liquid environment more efficiently, which is another major advantage for biological applications [37].

Supporting this, Figure 4.1 depicts the force resolution limits of tuning fork as compared to AFM optical lever methods and piezoresistive cantilever resolution studied in [27]. As it can be seen, the tuning forks have the widest range of force sensing. By utilizing the tuning fork probes, one can reach higher resolution ranges in terms of force sensing capability.

In addition, since force sensing with tuning forks do not require any laser beam bounce system and self-sufficient, it also enables experiments in conditions where laser might interfere with the measurements e.g. near-field optical measurements.

Since tuning forks have very sharp resonance response and our system has high resolution in terms analog to digital conversion hardware, ultra small changes in frequency can be detected. This helps us with obtaining the highest possible force resolution quantitatively in real time as opposed

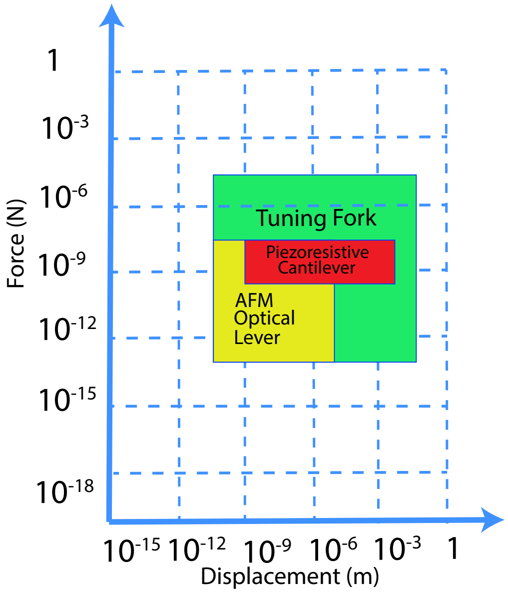

Figure 4.1: Force vs. Displacement resolution comparison of different sensors [27]

to other AFM cantilever based nanoindentation techniques. By this way, one can obtain the most accurate force curves in elasticity calculations for materials under investigation.

With phase signal used as feedback signal, amplitude can be monitored as a separate independent quantity. Thus, when a tuning fork with a tip approaches the surface with phase feedback, the oscillation amplitude is measured independently. The touching of the tip to the surface is detected very accurately since one sees an amplitude change independent of any effect of feedback. Therefore, one knows the exact point of contact which gives high precision and accuracy in estimation of material properties. This specifically eliminates a common problem encountered in material characterization of soft/biomaterials [5].

Furthermore, as it was addressed in chapter 1, due to very low spring constant of conventional AFM cantilevers and the surface interaction forces during nanoindentation, ‘snap-in’ effect occurs. This makes it very hard to investigate surface interaction forces. Higher spring constant eliminates this problem, as well.

Several studies have utilized tuning fork probes and the Sader’s formula in order to perform force measurements for mechanical characterization of ultra small specimens such as thin films or MEMS structures [27], [38], [15]. Acosta et al. have utilized tuning fork based probes for developing a wide range mechanical characterization tool inside a scanning electron microscope [27]. Abrahamians et al. developed a nanorobotic system utilizing tuning fork probes in order to measure mechanical stiffness of MEMS membranes in situ inside an SEM [38]. Oiko et al. utilized tuning fork probes and frequency-modulation force calculations in order to characterize multi-walled carbon nanotube bundles inside SEM [15].

These studies in the literature have showed the experimental validity of the Sader’s formula and motivated us to implement the same approach for nanoindentation experiments to characterize soft materials.

4.3 Experimental Setup

Special probe tips have been fabricated in order to perform nanoindentation experiments on the soft materials. These included straight indenter probes similar to diamond probe that was fabricated for hard materials (Figure 3.10(b)) as well as cantilevered probes.

Figure 4.2(a) - 4.2(c) demonstrate the images taken from each of the indentation probes fabricated for soft material nanoindentation. The probes in Figure 4.2(a) are straight indenter probes. Conical geometry ($\sim$ 20nm diameter) as well as spherical geometry ($\sim$ 400nm diameter) probes are fabricated. In addition to straight indenter probes, cantilevered ($\sim$ 50 μm length) probes are fabricated as shown in Figure 4.2(b) and 4.2(c). The tip diameter of these probes range from $\sim$ 40nm to $\sim$ 4 μm.

In order to keep the oscillation amplitude within reasonable magnitudes for nanoindentation and determine the distance of closest tip approach z in eq. 4.2, several calibration experiments were performed. Figure 4.3 shows a schematic of amplitude calibration experiments. Each probe was pressed against a hard sample (Silicon). Due to the hardness of the silicon sample and the spherical tip geometry of the probe tip, there is no nanoindentation expected on the sample. First, the probe contact is established and the

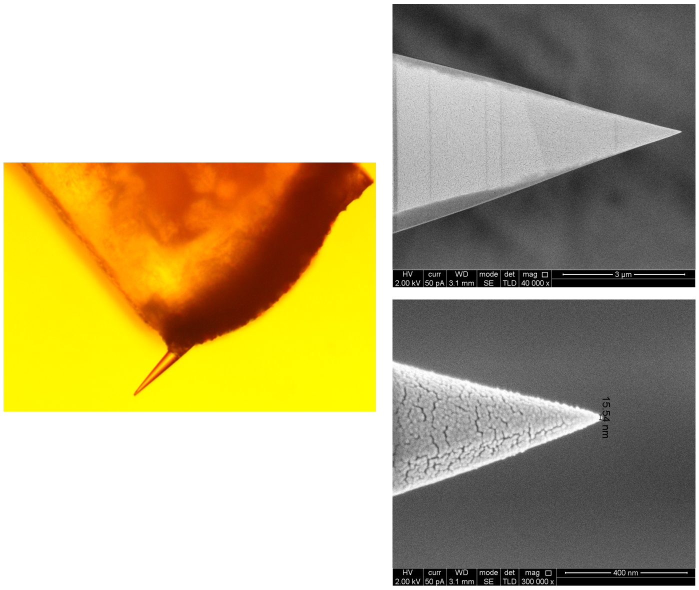

(a) Straight indenter probes fabricated for nanoindentation experiments including both conical shapes and ball probes (image not shown)

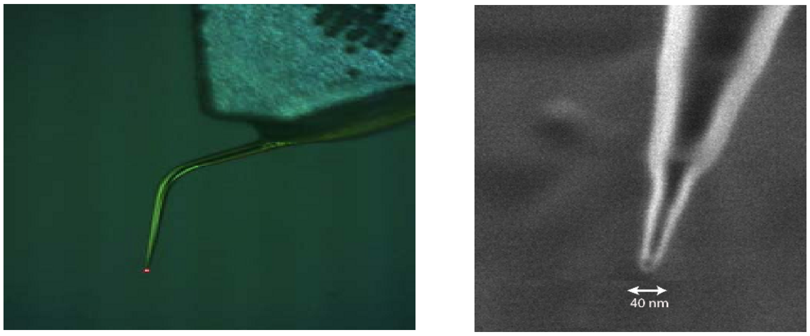

(b) Sharp tip cantilevered AFM probe including its SEM tip measurements

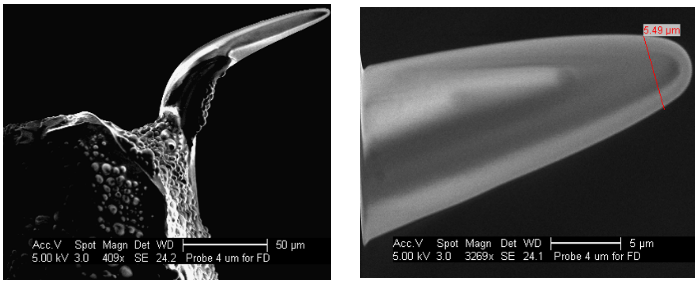

(c) Cantilevered indenter ball probes including SEM tip measurements

Figure 4.2: Cantilevered and straight indenter probes fabricated for soft material nanoindentation experiments

sample holder is programmed to press against the indenter tip so that its amplitude reaches zero for a very short time and then the sample is withdrawn. By analyzing the generated plots of amplitude vs. stage offset readings, one can determine the free oscillation amplitude.

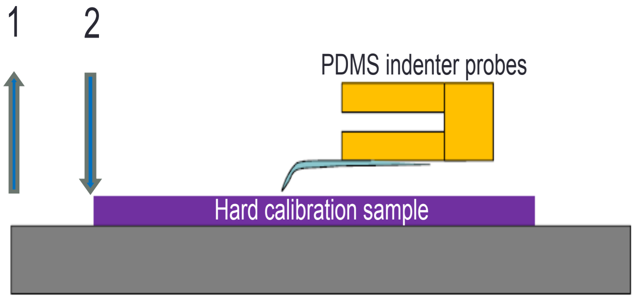

Figure 4.3: Schematic depicting amplitude of oscillation calibration experiments where there is no nanoindentation expected due to the hardness of the sample and the spherical tip geometry of the probe

Figure 4.4(a) shows the experimental data of the change of amplitude after a calibration experiment is performed. Initially, the stage is programmed to withdraw from the tip for about 150 nm and therefore there is no amplitude of oscillation change observed. After the initial withdrawn, the sample stage starts moving the sample up against the tip.

As it can be seen, as the stage pushes the sample up after around 3500 msec, the amplitude of the probe starts decreasing and it reaches to zero volt value. Immediately after this, the stage is withdrawn again and therefore amplitude of the probe starts to increase and reaches to its free oscillation value which is about 5.5 V. Figure 4.4(b) shows amplitude vs. stage offset during the calibration experiment. In order to determine magnitude of free oscillation of amplitude, one can measure the difference between where the amplitude starts to decrease and the amplitude is zero. This is calculated as 10.78 nm for this experimental setup.

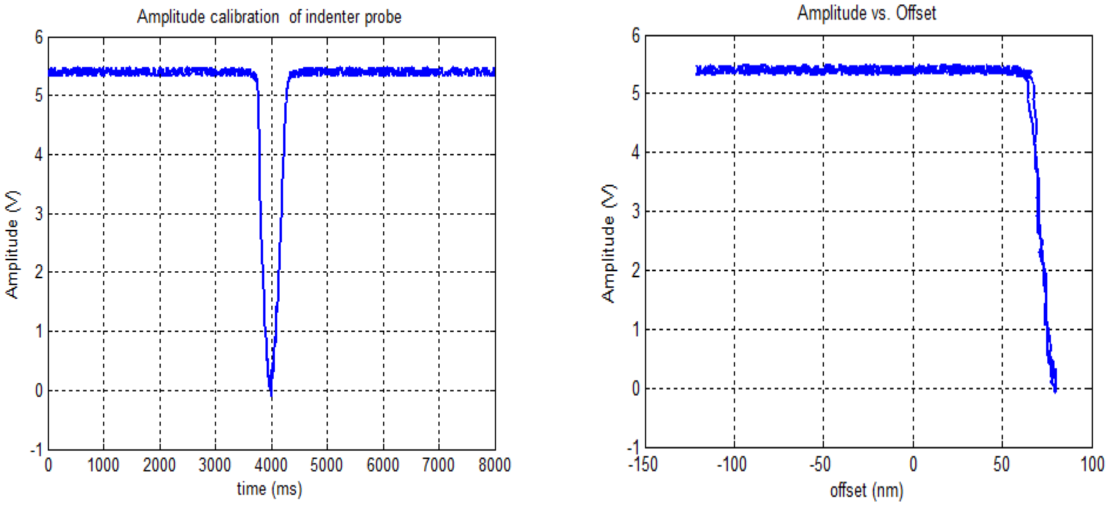

(a) Amplitude vs time (b) Amplitude vs Ofset

Figure 4.4: Experimental data from one of the amplitude calibration experiments

In order to keep magnitudes of oscillation within a reasonable range for nanoindentation experiments and also to ensure safe and stable approach to the specimen, 10 nm of probe oscillation has been determined as stable approach criterion. Each probe is calibrated with respect to this value before soft material nanoindentation experiments.

There are two parameters that need to be adjusted in order to perform amplitude calibration. One of these is called *Osc1* parameter which represents the amount of voltage applied to excite tuning fork. This ranges between

0-5 V_{pp}. Once the *Osc1* parameter is decreased, the amplifier gain parameter should be increased in order to provide an accurate feedback operation through error processing. High analog gain is not desired since excessive gain will also decrease signal-to-noise ratio. Similarly, very low *Osc1* parameter will reduce the amplitude of oscillation but may also cause reduced sensitivity due to lower quality of vibration.

Similar to a formula shown by Simon et al. for a scanning probe microscopy system [39], a linear expression can be developed between oscillation amplitude and amplitude readout such as $A_{OSC} = \alpha A_{READOUT}$.

According to this, an α coefficient is given for our system such as in eq. 4.3 where $A_{READOUT}$ term is $\sqrt{Amp^2 + Error^2}$ in mV. The term $A_{READOUT}$ can be obtained from output signals via the lock-in amplifier unit. A detailed formulation is derived in Appendix section A.

$$Mag_{nm} = \frac{800\sqrt{Amp^2 + Error^2}}{LockinGain * 5800} \tag{4.3}$$

In the next section, dynamic nanoindentation experiments and their results will be discussed.

4.4 Nanoindentation experiments on PDMS soft samples

Polydimethylsiloxane (PDMS) is a silicon-based organic polymer that has been widely used in microfabrication of microfludics chips and several other biomedical applications [40], [41], [42]. Its biocompatibility, transparency and easy to mold properties make it an attractive material for many microsystem applications.

PDMS mechanical properties have been investigated by many researchers in the literature [43–50]. As a rubber-like material, its mechanical properties can vary depending on its preparation conditions. The base polymer is mixed with its curing agent with a weight ratio (usually 10:1) and cured at a temperature which forms cross-links between its monomers. Due to its high dependency on preparation conditions, a broad range of elastic properties have been reported in the literature ranging from 0.1 MPa to 5 MPa [51]. Therefore, careful preparation conditions and highly accurate soft material characterization techniques are crucial.

The PDMS nanoindentation samples are spin coated on 18cm x 18cm glass substrates. First, PDMS is prepared with its curing agent (10:1) ratio and mixed thoroughly for a homogeneous mix. The mixture is placed in a vacuum desiccator for degasing (from starting time of the desiccation to spin coating is tracked and effort is given to keep the elapsed time on average one hour). Using SCS manual spin coater tool, the recipe is optimized in order to obtain the most uniform coating. After spin coating, glass slides are heated on a hot plate at 150 ^oC for 20 mins. The razor blade is used to scrape off the half of the coated film in order to create a step height for profilometer measurements. Thicknesses of the films on glass slides are measured with Tencor P2 profilometer and three measurements are taken across the cut line. By using the data obtained from profilometer measurements, the spin-coating curve is generated as it is given in Figure 4.5.

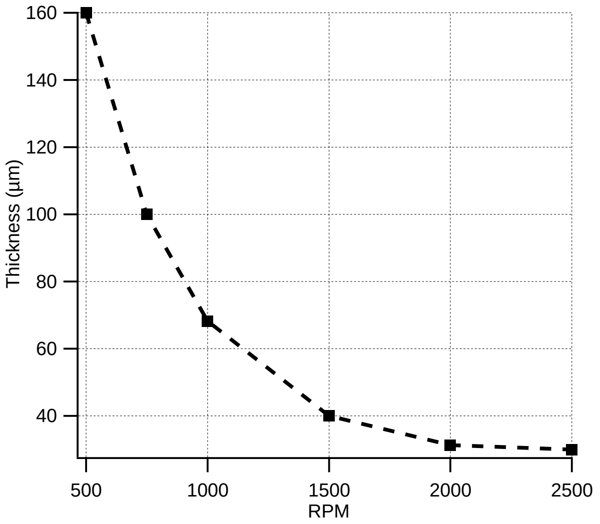

Figure 4.5: Spin speed vs thickness curve for PDMS

Nanoindentation experiments have been performed by using different types of probes as shown in Figure 4.2(a)- 4.2(c). Initial experiments are performed with straight sharp conical probes ($\sim 20nm$ diameter) and ball probes ($\sim 200nm$ diameter) where their images are shown in Figure 4.2(a).

During these experiments, the sample tip is moved up and down for nanoindentation using the lower piezo scanner. Initially, the tip approach is performed through sample surface with stepper motors and immediately after a contact is detected, the sample is retracted by piezo scanners. A fine approach is automatically initiated with piezo scanners to enable sensitive contact with the material surface. As the tip stays in feedback contact with the sample, the system is programmed for specific stage movements and the speed. The similar nanoindentation operation can be also performed with tip movement using upper piezo scanners instead of sample movement with the lower piezo scanner (sample holder). Figure 4.6 shows the user interface that is used to input nanoindentation parameters. If the sample scanner is used to move the sample up and down for nanoindentation, firstly the scanner retracts the sample down in an amount of Z_{min} μm then pushes the sample up against the probe by the amount of distance $Z_{max} + Z_{min}$ in μm. If the upper piezo scanner is used to move the tip through the sample then firstly the tip is retracted upwards in an amount of Z_{min} and then moved through the sample in an amount of distance $Z_{max} + Z_{min}$. Usually Z_{max} and Z_{min} are selected as the same numbers where Z_{min} is always a negative number however for soft materials due to adhesion between tip and sample, a different Z_{min} can be considered for complete dissociation of tip and sample. Speed is the parameter in $\mu m/msec$ that indicates how fast the sample/probe is moved up and down between Z_{max} and Z_{min}. Speed parameter is adjusted such that the total rise and down is around 30 secs in order to avoid possible noise sources due to rapid movement.

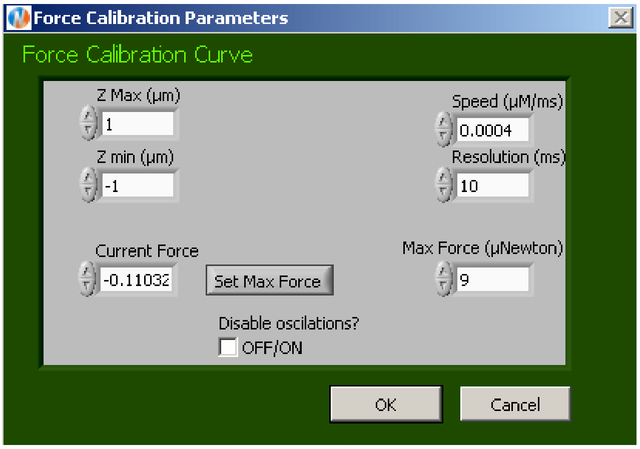

Force Calibration Parameters

Force Calibration Curve

Z Max (µm) 1

Z min (µm) -1

Speed (µM/ms) 0.0004

Resolution (ms) 10

Current Force -0.11032

Max Force (µNewton) 9

Disable oscilations?

☐ OFF/ON

Figure 4.6: Graphical user interface for inputting nanoindentation parameters before the experiment

When the nanoindentation experiment is started, the sample is retracted away from the indenter tip first and the probe gets out of the feedback. That is, the piezo scanners are not controlled in order to keep the tip in contact with the sample itself. Once the contact feedback mechanism is shut down, the stage is programmed to retract the sample in an amount of Z_{min} parameter. After this, the stage moves up the sample in an amount of Z_{min}+ Z_{max}. Immediately after, the stage is retracted the same amount, Z_{min}+ Z_{max}. At the end, the feedback mechanism is switched on so that the tip maintains contact with the surface.

Figure 4.7(a) and Figure 4.7(b) show changing of amplitude and error vs. time during one of the PDMS nanoindentation experiments with straight indenter probes. Initially as the oscillation amplitude is at about 5.3 V, when the sample is started to be pushed up against the probe, the amplitude starts to decrease. When the stage reaches its maximum programmed movement, it starts retracting the sample down and this is reflected as an increase in the amplitude of the fork up until that the probe and the sample are completely separated. Then the amplitude returns back to its initial value which is 5.3 V.

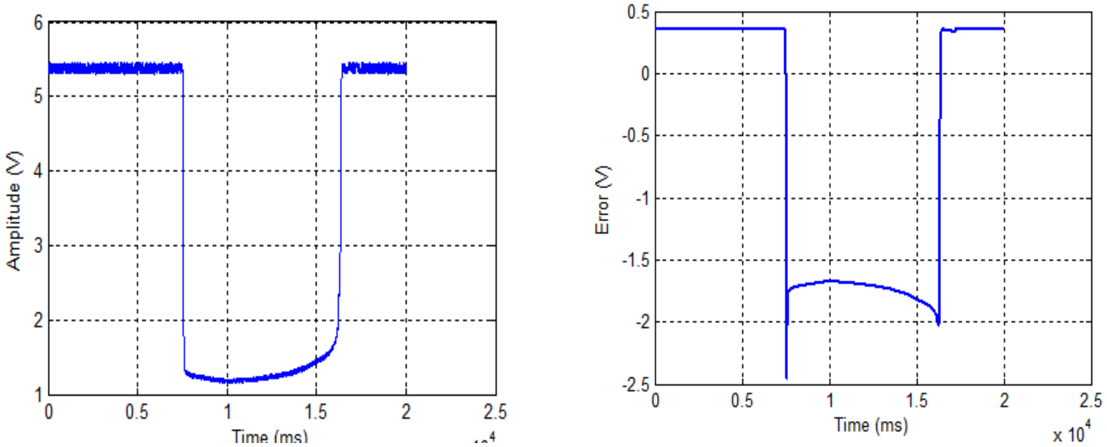

(a) Amplitude vs time (b) Error vs time

Figure 4.7: Change of amplitude and error during PDMS nanoindentation experiment with straight indenter probes

Since the system is programmed to operate in phase feedback mode, the error signal that is shown in 4.7(b) is the change of fork's phase oscillation with respect to the reference signal generated by the phase-lock-loop system.

Figure 4.8 shows the force-distance curve calculated by using Sader's formula given in eq. 4.2. As it can be seen in error vs. time plot in Figure

4.7(b), the vertical force applied by pushing the sample up and the straight indenter probe configuration makes the phase (error) signal change abruptly at the end and an overshoot is observed in the error signal. One reason for this could be a hardware limitation of the feedback circuitry that processes the error signal and causes overshoot in the error signal. This also affects the calculations of force values from Sader's formula due to iterative summation for integral operation and causes jumps in the force curve, as shown in Figure 4.8.

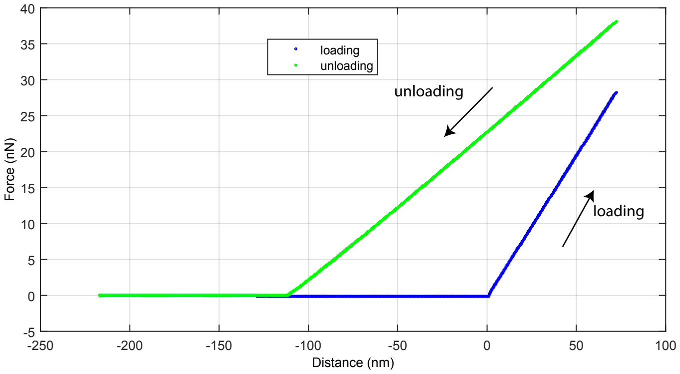

Figure 4.8: Force distance curve calculated using Sader's formula by utilizing straight indenter probes.

In order to reduce the spikes caused by this impact, cantilevered indentation probes are fabricated as shown in Fig 4.2(b) and 4.2(c). These probes can perform initial contact more smoothly so that the processed error signal by the PID controller do not include overshoot. The cantilever length is determined to be $\sim 50\mu m$. Diameters as small as $40nm$ and large spherical probes up to $4\mu m$ are fabricated.

Initial experiments with cantilevered $40nm$ type probes have shown promising effects on generation of force-distance curves. Figure 4.9(a) shows the amplitude vs. time plot during indentation onto PDMS using cantilevered probe. The spikes that exist in the error signal with straight indenter probes do not appear on the cantilevered probes and the force distance curves generated by Sader's formula is smoothed out and better fits to the contact models such as the Hertz contact.

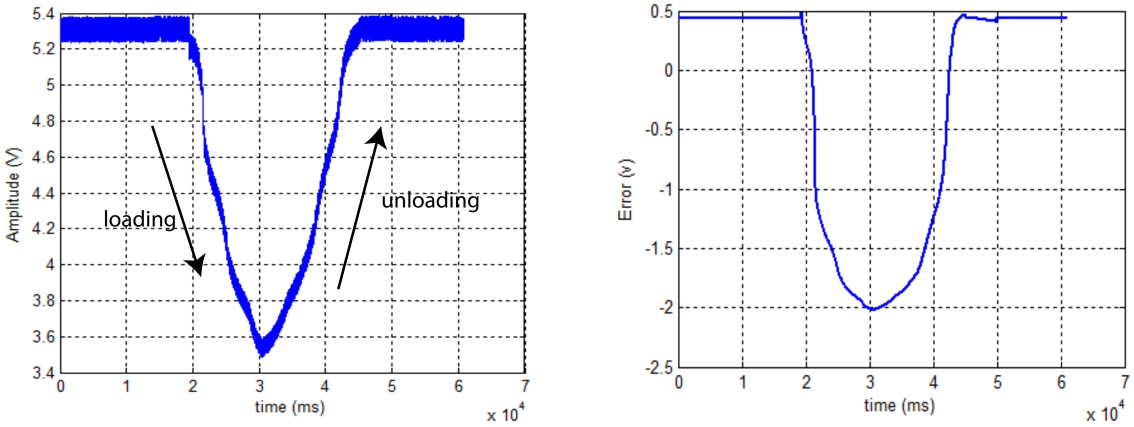

(a) Amplitude vs time (b) Error vs time

Figure 4.9: Change of amplitude and error during PDMS nanoindentation experiment with cantilevered indenter probes

Figure 4.10 presents an example of the force-distance curves obtained with cantilevered probes. Hertz contact model that was previously introduced in section 3.2 is fitted to the loading part of the force distance curve when E=1.85MPa and R=20nm. Unlike straight indenter probes, the cantilevered probes do not exhibit jumps in the force-distance curves caused by the overshoot in the phase error signal. This is due to reduced physical impact on loading during nanoindentation which keeps the change of error within hardware limitations.

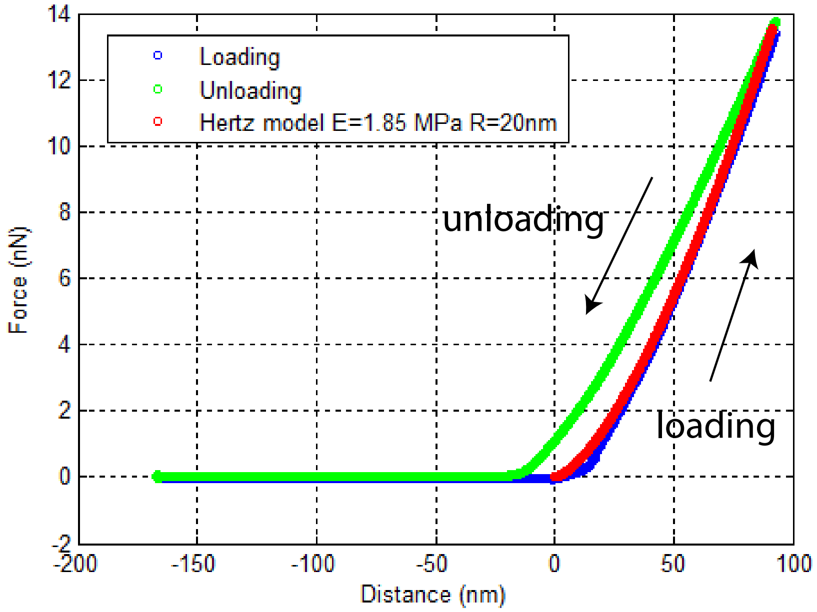

Figure 4.10: Force distance curve calculated using Sader's formula by utilizing cantilevered indenter probes with $R \cong 20nm$.

One of the important assumptions for Hertz model is that during indentation, surface deformations (δ) are small. That is, the tip geometry is much larger than the deformation on the surface ($\delta \ll R$). Considering this important criterion, larger size ball probes are fabricated as shown in Figure 4.2(c).

Figure 4.11(a) and 4.11(b) demonstrate the change of amplitude and error signal with respect to time. As compared to the results that were shown in Figure 4.7(b) with straight indenter probe, the cantilevered ball probes give promising results in terms of force-distance curve calculations without the overshoot effects during loading in nanoindentation experiments. Asymmetric change of error signal during unloading with respect to loading part is due to the adhesion interactions between PDMS material and the ball probe tip which is reflected as higher force values on the unloading curve in Figure 4.12

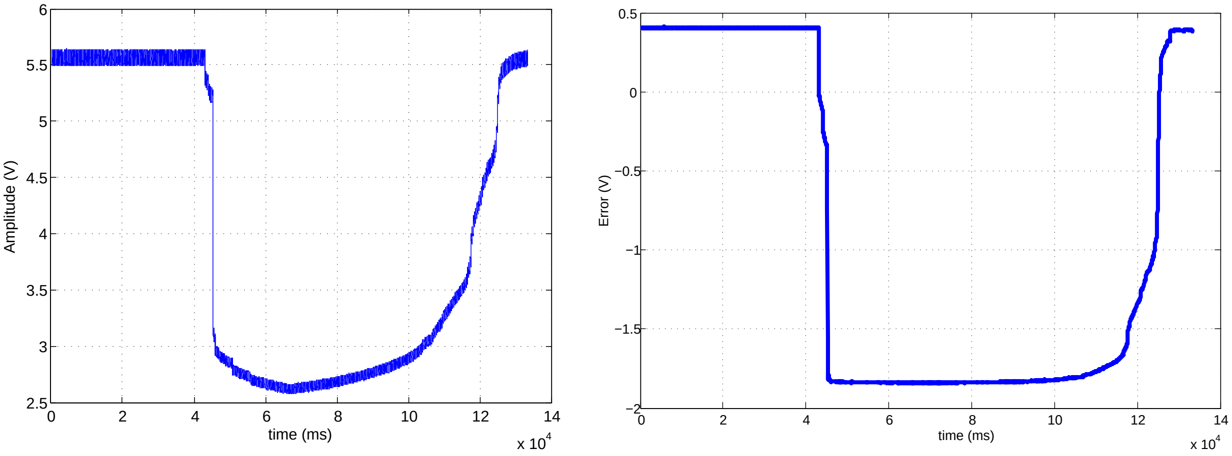

(a) Amplitude vs time (b) Error vs time

Figure 4.11: Change of amplitude and error during PDMS nanoindentation experiment with cantilevered indenter ball probes with $3.52\mu m$ diameter as shown in Figure 4.2(c)

Figure 4.12 presents the force-distance curve obtained by using cantilevered ball probes with $3.52\mu m$ diameter. The Hertz model fitted with $R = 1.76\mu m$ and $E = 0.8MPa$ is also included in Figure 4.12. In order to verify the force levels and the fitting results, finite element simulations are performed in COMSOL. As the results indicate, obtained values are in agreement with both Hertz contact model as well as the simulation results.

The calculated RMSE between Comsol simulation results and experimental data is 16.1386. The RMSE value between Hertz model estimation and experimental data is 7.0737. The hysteresis between loading and unloading curves is due to mechanical effects such as adhesion between tip and soft PDMS sample.

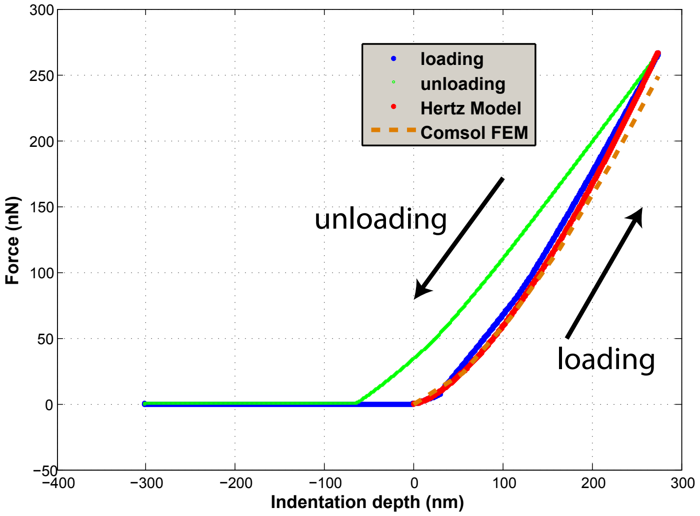

Figure 4.12: Force distance curve calculated using Sader's formula by utilizing cantilevered indenter probes with $R = 1760nm$.

Figures 4.13(a) and 4.13(b) demonstrate the configuration of nanoindentation simulations. An axisymmetric simulation model is configured on PDMS material where Elastic modulus is taken as 0.8MPa and radius of the indenter is taken as $R = 1.76\mu m$ which is calculated through SEM images of the actual ball probe. The material PDMS is modeled as Linear Elastic Material inside COMSOL and the tip is pressed against the sample with a prescribed incremental displacement of 274 nm. Reaction forces on the surface of the ball indenter is calculated by integral operators and summed up in order to calculate nanoindentation forces as it is shown with a dotted line in Figure 4.12.

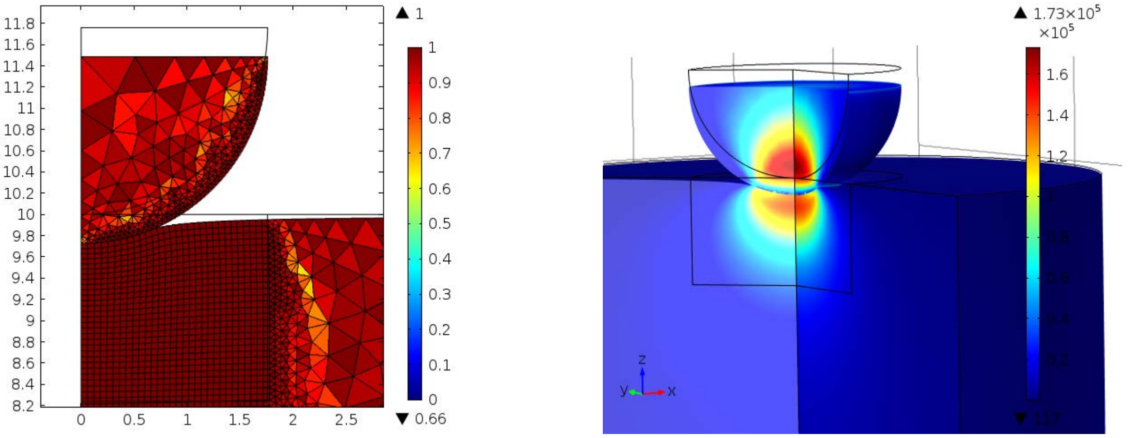

(a) Mesh deformation of nanoindentation

(b) 3-D representation of nanoindentation simulations

Figure 4.13: Nanoindentation simulation results in COMSOL for ball probes with $R = 1.76\mu m$ and $E = 0.8MPa$

The ball probes with larger radii have been used for the rest of the nanoindentation experiments on PDMS. In order to examine nanoindentation size effects on varying thickness of PDMS films, different thicknesses of PDMS are spin coated on glass slides while keeping the curing time and the curing agent ratio exactly the same at each time.

Figure 4.14 shows the results obtained on $161.23\mu m$ thick PDMS films with varying indentation depths indicated as h_{max}. The estimated elastic modulus values settle at around 0.8 MPa after nearly 150nm indentation depth. Similar effects are also observed by other studies in the literature and attributed as *Indentation Size Effect* on various types of polymer materials [45], [47], [52], [53], [50].

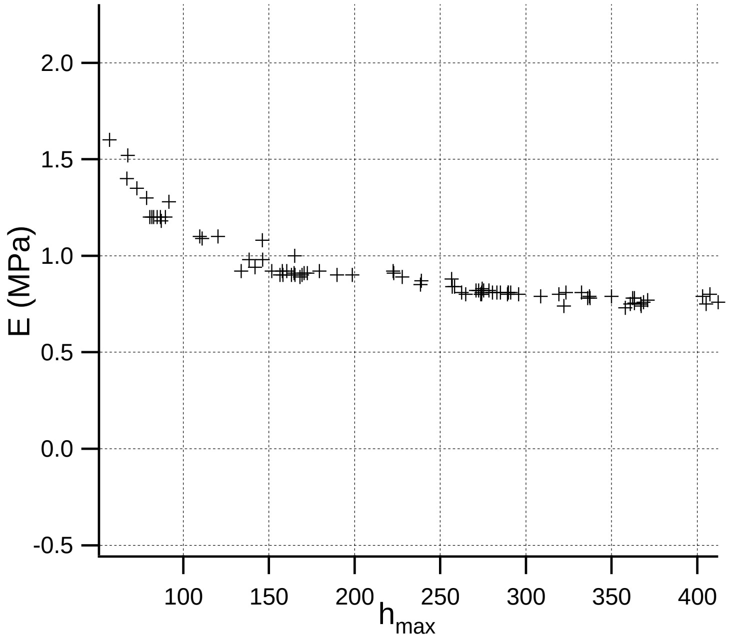

Figure 4.14: Estimated elastic modulus vs. indentation depth performed on $161.23 \pm 1.39\mu m$ spin-coated PDMS with probe radius $R = 1760nm$

Wrucke et al. summarizes the results of other studies in a graph where similar indentation size effects have also been reported as shown in Figure 4.15 [52]. Although some of the polymers such as UHMWPE (Ultra-high-molecular-weight-polyethylene), PTFE (polytetrafluoroethylene or teflon) do not exhibit such effects, as it can be seen from the graph, the rest of the polymers exhibit this type of indentation size effects.

The high scatter below 50nm regime could be attributed to the reasons such as surface roughness, and indenter imperfections. However for $h >$

$50nm$ the size effect is still observed in many polymers.

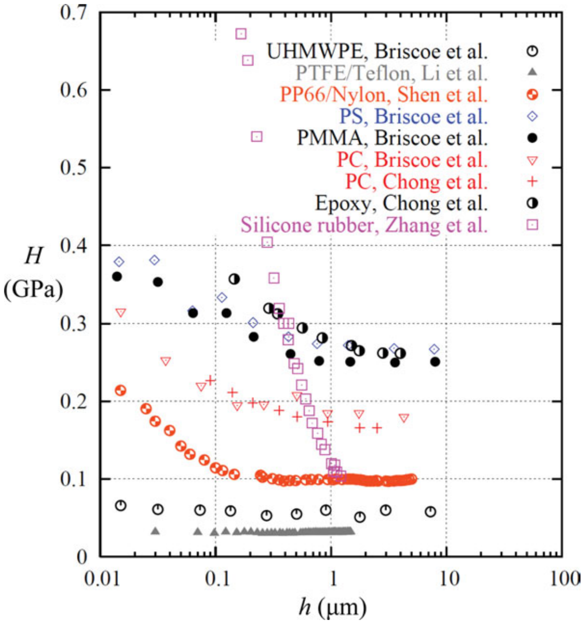

Figure 4.15: Elastic modulus estimation vs. indentation depth of various polymers that exhibit indentation size effect [52]

There are several rationales behind this effect proposed in the literature. Lim et al. and Zhang and Xu both suggest that surface effects such as surface stress, surface roughness, adhesion, and friction at the edges of the indenter for smaller depths might result in increased force levels and therefore might cause the overestimation of the elastic modulus [53], [54]. Zhang and Xu identifies that there exists a critical indentation depth where beyond this depth, the bulk deformation predominates [54].

Figure 4.16 shows the results that Lim et al. received on PDMS nanoindentation with different curing ratios [53]. It shows that when 10:1 ratio has been used, similar indentation size effects on elastic modulus estimations have been also observed.

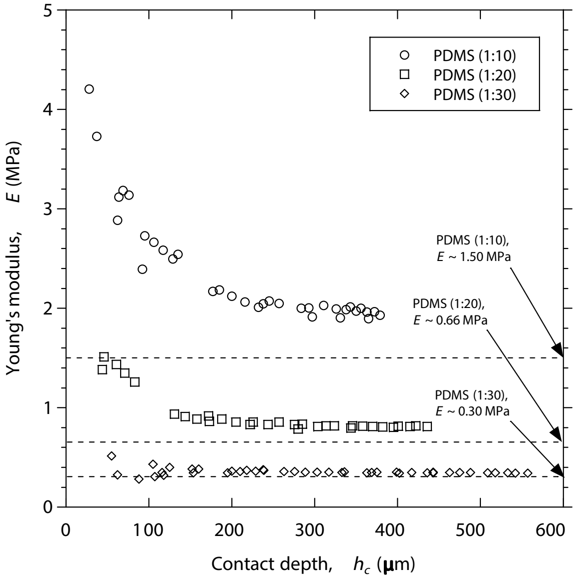

Figure 4.16: Elastic modulus estimation vs. indentation depth of PDMS that exhibit indentation size effect similar to our findings [53]

Liao et al. compare Hertz contact model estimations of PDMS nanoindentation with respect to JKR model which takes the adhesion effect of indentation into consideration by expanding the Hertz model [55]. The nanoindentaiton experiments are performed with a spherical probe geometry similar to our experiments. As the results in Figure 4.17 demonstrate, the estimated values of elastic moduli converge into the JKR model estimations (dashed lines of constants) as the maximum applied force becomes larger. This suggests that the Hertz estimation can be used as a procedure to estimate elastic modulus by fitting data without taking surface adhesion effects into consideration.

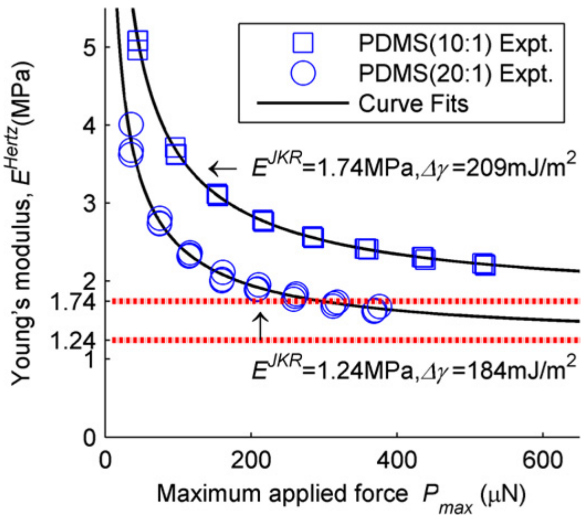

Figure 4.17: Elastic modulus estimation vs. indentation depth of PDMS [55]

In order to observe whether varying film thickness affects elastic modulus estimations, thinner and thicker PDMS films are prepared. The lowest thickness at which a uniform film can be obtained by spin-coating process is found to be around $35\mu m$ (Figure 4.5). Therefore $35\mu m$ films are prepared at 2000 rpm spin-speed and cured with the exact same preparation conditions with the rest of the samples. In addition to thin PDMS samples, manually prepared thick PDMS samples are also used for investigation of bulk elastic modulus estimations.

Figure 4.18 presents the results of nanoindentaiton obtained on $35.23\mu m$ thick spin-coated PDMS sample. A similar type of behavior on elastic modulus estimations has been observed as shown in Figure 4.14. The elastic modulus estimations change with indentation depth but settles at around 0.75MPa.

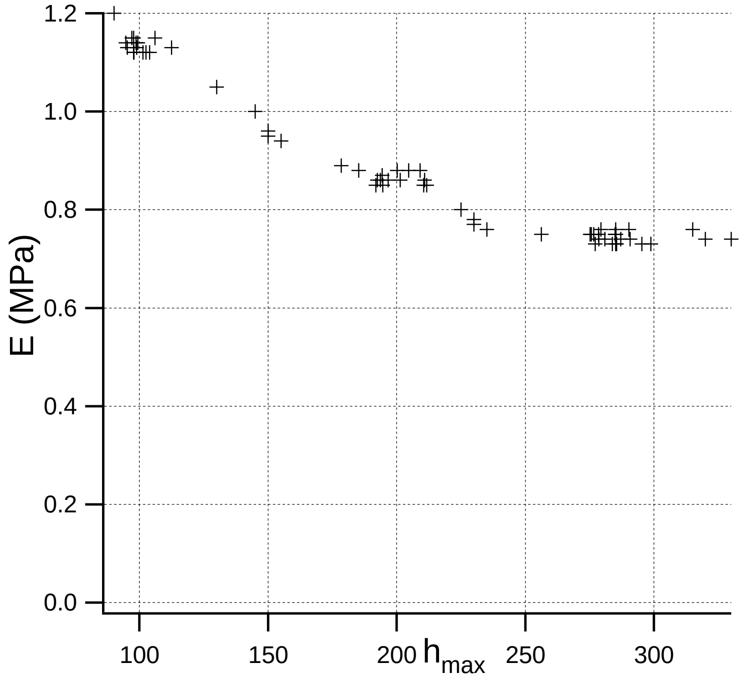

Figure 4.18: Estimated elastic modulus vs. indentation depth performed on $35.23 \pm 0.085 \mu m$ thick spin-coated PDMS with probe radius $R = 1760nm$

Figure 4.19 shows the results on bulk PDMS with a large thickness that is not prepared with spin-coating process but other parameters were kept exactly the same. Similar behavior has also been observed with bulk thickness levels where estimated elastic modulus settles at around 0.8MPa.

Table 4.1 summarizes the results obtained on $161.23\mu m$, $35.23\mu m$ and relatively thicker PDMS ($\sim 1cm$) named as bulk. The average results are obtained by grouping the measurements for the same level of penetration depths that is $h_{max} \simeq 250nm$ over 15 experimentally measurements. This level is determined to be a critical indentation depth that elastic moduli estimations are observed to start settling.

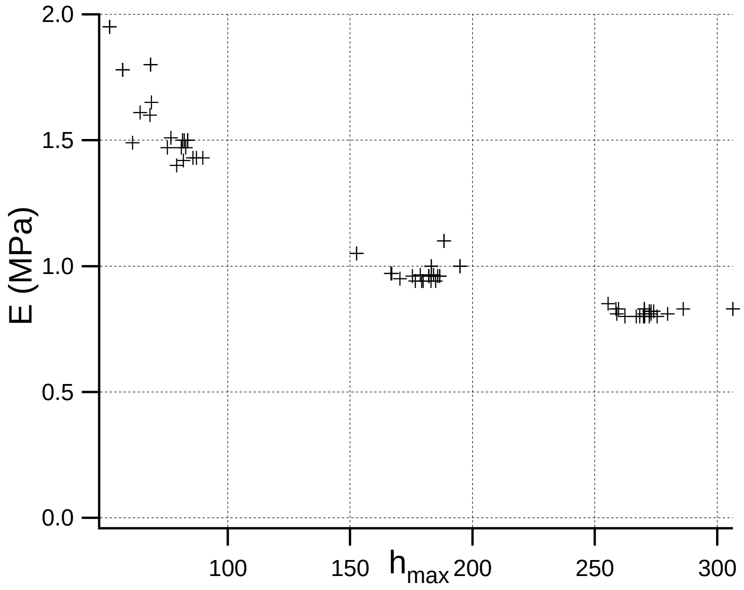

Figure 4.19: Estimated elastic modulus vs. indentation depth performed on bulk PDMS with probe radius $R = 1760nm$

Table 4.1: Summary of results estimating PDMS elastic moduli on different thickness levels and at similar indentation depths

PDMS Film Thickness	$\hat{h}_{max}$	**std**	$\hat{E}(MPa)$	*std*
35.23 μm	225	29.12	0.7758	0.054
161.23 μm	279.43	9.71	0.8049	0.043
Bulk	269.62	2.85	0.8115	0.014

According to the results in Table 4.1, 0.8 MPa elastic moduli can be accepted as a reasonable value for PDMS on further studies in this dissertation work.

4.5 Conclusions

In this chapter, by utilizing frequency modulation (FM) techniques and tuning fork indentation probes, it is shown that we can successfully estimate elastic modulus of soft materials particularly for PDMS material. Optimal tuning fork nanoindentation tip characteristics have also been throughly examined and determined within this section. The estimated elastic modulus results are within the same margin for various range of film thicknesses and significant deviations are not observed through current thickness levels as opposed to several studies have reported in the literature [50], [47], [45]. However, in order to assure the observed variation is due to experimental noise, further experiments with more intermediate thickness levels might be necessary. On the other hand, indentation depth dependency is observed on elastic modulus estimations similar to other studies and critical depth is determined for these experiments. The results obtained in this section is also used to accurately estimate mechanical deflection behaviors of high aspect ratio PDMS micropillars.

The dynamic force sensing technique developed in this chapter enables users to utilize tuning fork probes as an ultra-sensitive force sensors. By using these techniques, mechanical characterization of MEMS microstructures can be successfully performed. The next chapter presents the microfabrication techniques of PDMS micropillars, the mechanical experiments performed with tuning-fork sensors for characterization as well as the results showing the viability of these experiments on a biomedical application.

Chapter 5

Mechanical characterization of high aspect ratio PDMS micropillar structures and its application to measuring cell traction forces

5.1 Introduction

In chapter 4, frequency-modulation techniques are utilized in order to extract force values for nanoindentation on soft materials which require a high resolution force and displacement sensing. Thanks to high quality resonance properties of tuning forks, one can obtain very high resolution force sensing that can be used as a force sensor in mechanical characterization of micro-nano structures that might be critical components of MEMS devices.

In this section, an accurate mechanical characterization of high aspect ratio (HAR) micropillar structures utilizing ultra-sensitive tuning-fork force sensors are demonstrated together with its application in a biomedical study.

High aspect ratio (HAR) microstructures have been the main focus of many studies. With the rapid advancement of nanotechnology and microfabrication techniques, researchers were able to mimic and analyze such structures where they were inspired by the nature most of the time. Among these high aspect ratio structures, micropillars are the simplest and most commonly studied patterns. At micrometer scale, one can observe these structures as dense arrays on certain plants used for self-cleaning purposes [56]. Similar structures have been studied for dry adhesion properties inspired by gecko footpad [57].

By utilizing microfabrication techniques, researchers have fabricated the same artificial hierarchical structures in order to obtain dry adhesive properties for various applications [58] .

On the other hand, a significant amount of research has been devoted to biological analysis of single cells by utilizing HAR micropillars. Cells can be cultured on micro structures and they can be used as a helpful tool for biologists in order to investigate physical environmental factors on cell response [59–67]. For example, by changing the aspect ratio of these structures, substrate stiffness can be modified. Several researchers in the literature have investigated the response of cells by altering the aspect ratio of micropillar structures which make the substrate less or more stiff. Fu et al. studied the different responses of stem cells on micropillar structures based on the varied stiffness [68]. By changing the aspect ratio of micropillar structures a softer (fat like) or stiffer (bone like) substrates can be created.

In addition to the substrate stiffness tests that are made possible using these micropillar structures, it is possible to measure very small scale cellular forces by utilizing them. Cells are known to exert forces on the substrates as they perform certain biological events e.g. cell proliferation, migration, and adhesion which are highly important in understanding of various medical phenomenon [69], [70]. Among these, traction forces are the tangential forces exerted by cells on the substrates as the cells move forward. These forces are generated by reorganization of cell cytoskeleton which occurs due to the restructuring of actin elements in cell cytoplasm. By utilizing the deflection of microposts, it is possible to analyze and quantify these forces. As cellular traction forces are very small (nN) forces, in order to extract the most accurate data, mechanical characterization and modeling of these microstructures should be performed very accurately, as well. These include elastic properties of the material that these structures are made of as well as through mechanical deflection models that will accurately predict deflection of the micro-structures.

Many studies in the literature have utilized PDMS HAR micropillar arrays as force sensors to quantify cellular traction forces [69,71–76]. Bashour et al. use PDMS micropillar to measure T-cell traction forces and investigate the effect of biological cell receptors such as CD3 and CD28 [77]. Khademolhosseini et al. present microfabrication of active magnetic PDMS micropillar arrays to apply cyclic forces to cells for tissue engineering applications [78]. Roure et al. demonstrate measurement of mechanical forces applied by Madin-Darby canine kidney (MDCK) epithelial cells [79].

Despite the common use of PDMS micropillar arrays as force sensors in biomedical applications, the mechanical models employed to estimate force levels are very simple and can significantly overestimate the results. This is due to the inherent material behavior of PDMS as an elastomer as well as size-scale effects that arise for micron-level dimensions. Hence, several studies focused on pure mechanical characterization of these structures and proposed the appropriate models that give improved mechanical behavior estimates. [80–84].

Du et al. suggested the use of viscoelastic material models such as viscoelastic Timoshenko beam model for PDMS micropillar arrays due to insufficiencies encountered with standard Euler or Timoshenkp beam bending models [81], [83], [84]. A major drawback of these studies is the resolution limit of the utilized equipment for force and displacement sensing. A commercial instrumented nanoindenter tool that is mostly used for hard material nanoindentation experiments is utilized and this might not have sufficient force resolution for an accurate material characterization of soft PDMS micropillars.

Schoen et al. investigated the contribution of substrate warping on PDMS micropillar deflection and modify standard Timoshenko beam model to include the warping effect for pillar deflection [80]. A commercial force sensor (FT-S270 OEM, FemtoTools) is used to read force values during micropillar deflection experiments. The sensor's operating principle is based on measuring the capacitive deflection change between comb-like interdigitated electrodes when the cantilever on the tip is deflected. The reported specifications of this sensor based on the manufacturer include sensitivity of 2.0 μN with a stiffness of 1000 N/m [85]. Considering the expected force levels that PDMS micropillar structures are used for sensing (nN regime), the employed sensor is not satisfactory.

In a recent work published by Lee et al., deformation behavior and mechanical properties of PDMS micropillar structures with 30 μm height and 10 μm diameter are studied inside an SEM environment, *in-situ*. Silicon microcantilever with a piezo-resistive read-out circuit is used to read the force values during vertical loading and unloading operation on the micropillar [82]. Figure 5.1 demonstrates the experimental setup inside the SEM chamber as well as images taken during one of the load experiments. The results show the strong adhesion effects between the tip and the micropillar surface and the authors investigate mechanical behavior such as buckling during loading and effective elastic modulus estimations.

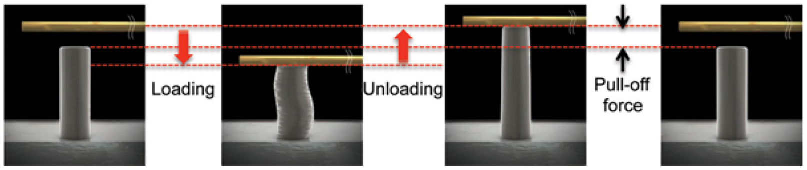

Figure 5.1: In situ mechanical characterization of PDMS micropillar by utilizing a silicon microcantilever as a force sensor [82]

In this chapter, a mechanical characterization technique of PDMS HAR micropillar structures is presented by using an ultra-sensitive force sensor that is developed during this dissertation work and verified by utilizing identification of soft material elastic properties, particularly PDMS. Various mechanical models are investigated to find out the most accurate model for micropillar structures. The results of an example application for cell traction force measurement are presented where our findings can be applied for an accurate cellular force microscopy technique. The next section presents a detailed description of microfabrication techniques that are used to fabricate HAR PDMS micropillars.

5.2 Microfabrication process of High-Aspect-Ratio PDMS Micropillar structures

The PDMS micropillar structures with different aspect ratios are fabricated utilizing micromolding process. The micromolds that are necessary for this operation is created by using SU-8 lithography.

The SU-8 is an epoxy based negative photoresist material which has been commonly used as a structural material in high aspect ratio patterning of MEMS structures. The photoresist operates in i-line (365nm) wavelength band and crosslinks upon UV light exposure. In order to investigate the processing limits and optimize the process parameters for our SU-8 micropillar fabrication, both positive and negative types of chromium masks are designed and fabricated. These masks include different diameter and spacing feature sizes of molds and pillar structures. The microfabricated molds fabricated with SU-8 have been used to pattern PDMS material utilizing soft lithography approach.

Figure 5.2 shows the details of microfabrication process in order to create SU-8 molds that are used to fabricate PDMS micropillars arrays. The designed mask contained features as small as 5 μm diameter circles and 10, 20, 50, 100 μm diameter circles as well. In order to investigate our process resolution and maximum aspect ratio that can be achievable using the SU-8 lithography technique, different SU-8 film thicknesses have been prepared. The SU-8 type 2075 (MicroChem) have been used to coat wafers in ranging thicknesses from 20 μm to 100 μm where SU-8 thinner solution have been utilized to dilute the photoresist whenever it was needed.

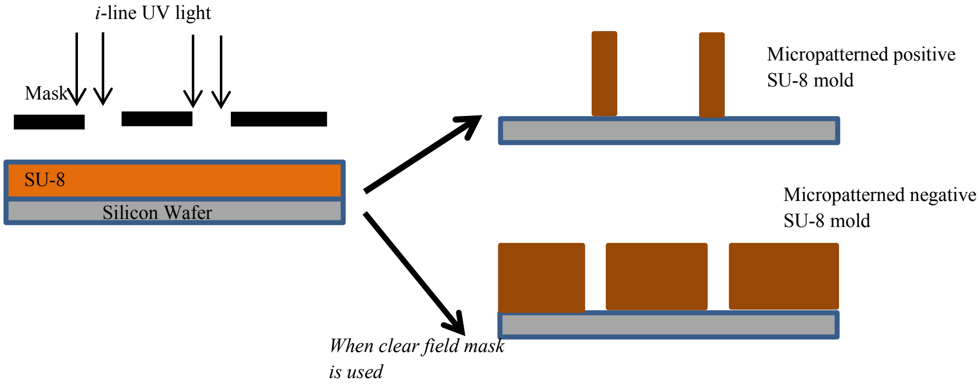

Figure 5.2: SU-8 mold microfabrication

An extensive experimentation is conducted to find the optimum film thickness as well as the highest achievable aspect ratio. There were several difficulties encountered during the microfabrication process. One of these problems was edge-bead problem occurred during exposure step of SU-8 films which limited the process resolution. Due to high viscosity of SU-8 films, during spin coating an edge bead occurs [86]. Figure 5.3 presents a detailed schematic of the edge bead problem encountered during SU-8 processing and the important parameters. According to this, the smallest feature size or critical dimension (CD) that one might obtain is given by the formula in eq. 5.1.

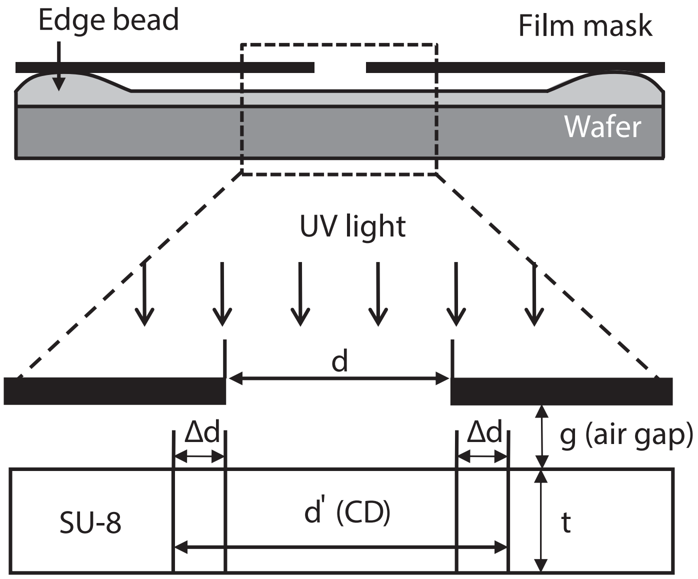

Figure 5.3: Schematic showing the effect of edge bead problem with SU-8 during microfabrication process [86]

where λ is the wavelength of the light that is used to expose the photoresist in meters, g is the amount of air gap between the mask and the film, t is the uniform film thickness outside of the nonuniform photoresist film area. As it can be seen from eq. 5.1, the air gap g is proportional to critical dimension CD. Thus, the higher the air gap will result in lower resolution on SU-8 films.

$$CD = \frac{3}{2}\sqrt{\lambda(g + \frac{t}{2})} \tag{5.1}$$

In order to answer this problem, the SU-8 films were sprayed with SU-8 solvent and left for homogeneous drying covered with a petri dish as suggested in [86]. This allows the film to reflow and after the relaxation, the edge bead disappears. Figure 5.4 demonstrates an image taken during microfabrication of wafer molds.

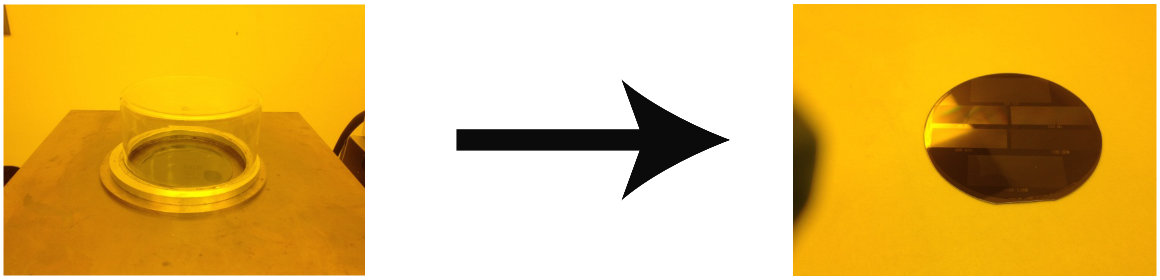

Figure 5.4: Image taken during microfabrication process in order to eliminate the edge bead problem and a wafer mold fabricated without the edge-bead problem

Figure 5.5 demonstrates some of the micromolds (microwells) fabricated with SU-8 lithography.

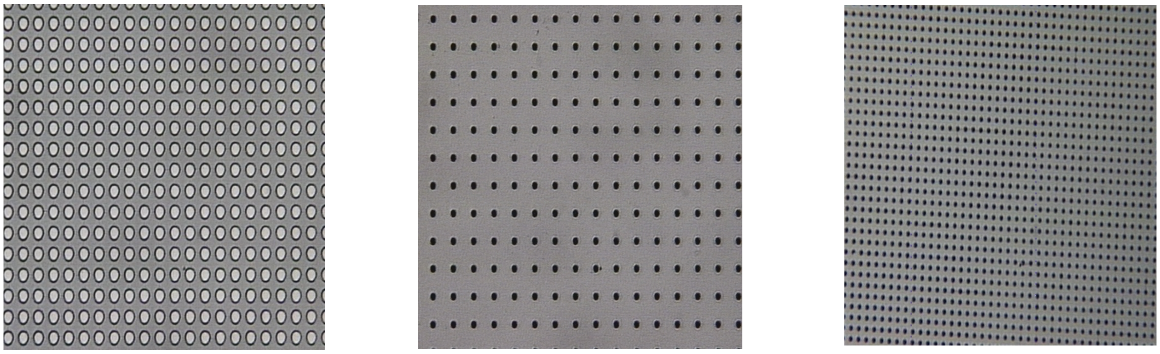

100 µm diameter molds

50 µm diameter molds

5 µm diameter molds

Figure 5.5: Micromolds fabricated by utilizing SU-8 lithography

Another major problem encountered during the development stage of micromolds. For small feature sizes when microwells are created with clear field masks, due to surface tension of the developer solvent, the bottom of the microwells were not developed completely. This caused shallow microwell heights than the actual film thickness. In order to overcome this problem, instead of utilizing microwell molds, SU-8 micropillars are fabricated first then used to create PDMS microwell molds.

During SU-8 micropillar fabrication process, due to reduced adhesion of micropillars to silicon wafer, it was observed that some of the SU-8 pillars were breaking off (Figure 5.6). This problem is remedied by coating the wafer initially with a very thin layer of flat SU-8 and flood expose. After this, the second layer of SU-8 that is on the target thickness of micropillar structures is spin-coated and patterned. Since the bonding of SU-8 layer to another SU-8 layer is stronger than bonding to silicon, this enhanced the durability of micropillar structures for further fabrication steps. In order to reach a very thin layer of SU-8, SU-8 thinner is diluted with its thinner using magnetic stirrer and spin coated immediately. The base layer thickness for this modification was $5\mu m$.

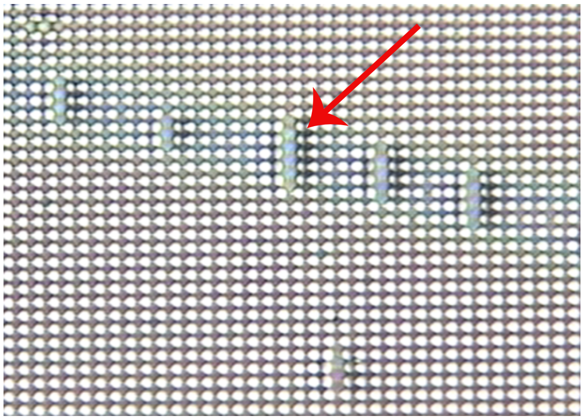

Figure 5.6: Physical failure of SU-8 pillar molds that has $10\mu m$ diameter, $5\mu m$ spacing and 20 μm film thickness happened during the development step

In order to pattern PDMS polymer utilizing these molds, PDMS is mixed in 10:1 ratio with its curing agent, and poured over the SU-8 molds fabricated in the previous step. The whole process of PDMS micropillar fabrication is shown in Figure 5.7.

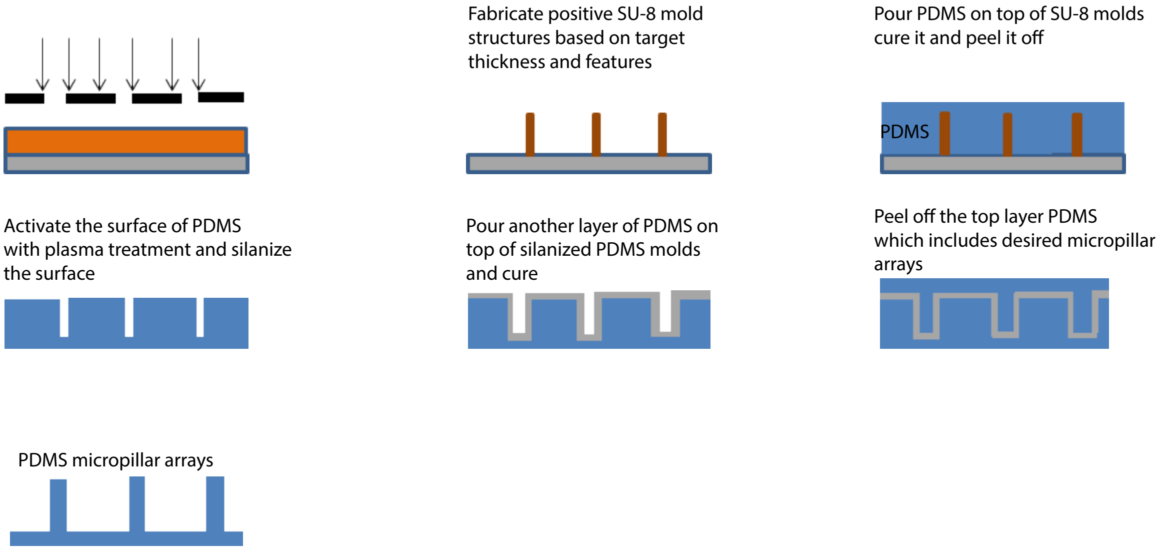

Figure 5.7: Schematic that explains the fabrication of micropillar arrays utilizing positive SU-8 mold structures

Once PDMS micromolds are fabricated, in order to enable PDMS to PDMS pattern transfer, the mold surface is activated with a plasma treatment first and then silanized with trichlorosilane (Gelest Chemical) by leaving inside a vacuum desiccator overnight. The silanized PDMS micromolds can be used similarly in order to pattern another layer of PDMS which includes the micropillar arrays. In the next section, mechanical characterization of micropillar structures with tuning fork sensors is presented.

5.3 Mechanical deflection experiments with tuning-fork sensors

In order to mechanically characterize single micropillar and extract force displacement curves similar to thin PDMS film characterization, the fabricated structures have been positioned as 90^o tilted. A representative schematic is given in Figure 5.8(a). Various different types of probe models have been used in order to establish sensitive contact with the tilted micropillars. As opposed to cantilevered indenter probes, straight indenter probes with 200nm diamater is used in pillar pushing experiments due to its ultrasensitivity in terms of contact detection with the pillar surface during approach. Figure 5.8(b) shows one of the micropillars used in deflection experiments with $h = 29.85\mu m$ and $D = 9.5\mu m$.

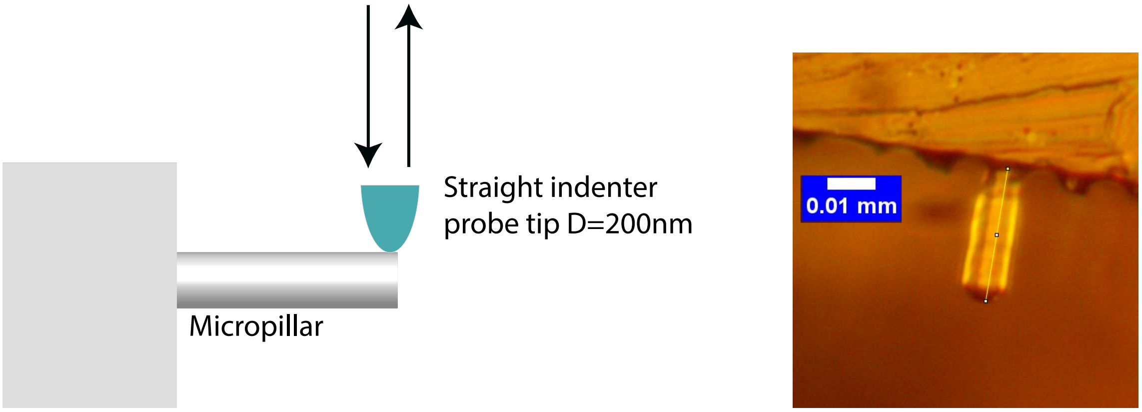

(a) Tilted micropillar deflection experiment setup

(b) Example microscope image of a tilted micropillar $h = 29.85\mu m$ and $D = 9.5\mu m$

Figure 5.8: Experimental setup and microscope image of one of the micropillars

Before approaching to the pillar, amplitude and PID control settings were adjusted so that during approach when the contact is detected no visual deflection occurs on the microscope camera. Long distance 50X objective is used to capture images during the experiments together with additional 10X optical zoom of the camera. Initially, the microscope optical plane is adjusted so that the glass probe tip mark is visible through camera. The probe is placed close to the surface of the pillar and the tip is adjusted to the point of interest for contact, by using X and Y offset knobs, manually. These knobs are used for fine-positioning of the probe tip by applying voltages to the upper piezo scanners and are available within the HV Piezo Control box unit. The measurements are taken at the very end of the pillar by applying prescribed displacement to the probe tip and force values are calculated by utilizing Sader's formula which was introduced in the previous chapter (eq. 4.2).

Figure 5.9 presents change of height and phase signal vs. time in msec during load-unload experiments of a micropillar. The probe tip is pushed 1346 nm and the phase signal increases during pushing and decreases during the retraction of the probe tip.

Figure 5.10 presents the force-distance curve generated by utilizing Sader's formula and the data obtained in Figure 5.9. Note that, during calculation of the F-D curves for micropillar deflection experiments, the spring constant

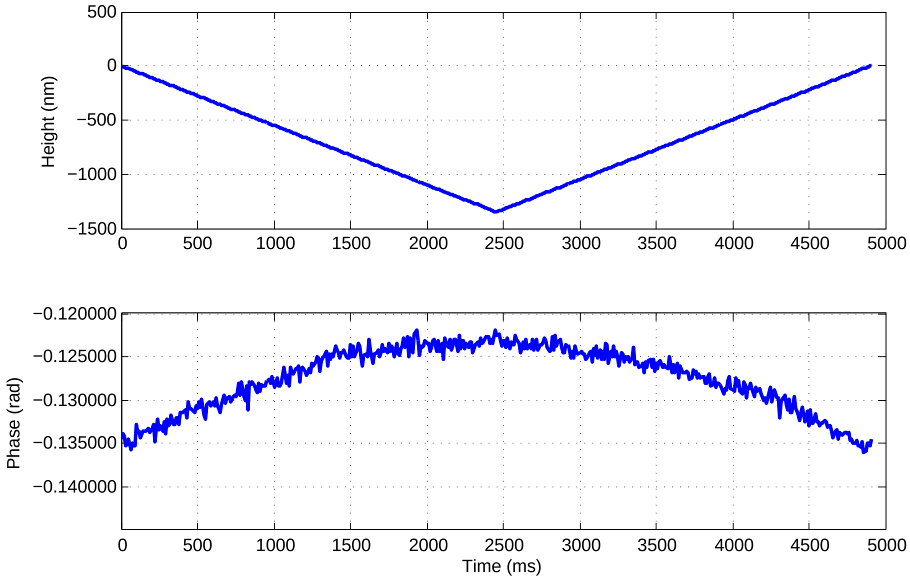

Figure 5.9: Data from one of the micropillar pushing experiments. Change of probe height vs. time plot during mechanical deflection (top graph) and change of phase vs. time plot (bottom graph)

of the tuning fork is taken 4992 N/m in accordance with the value that was determined during nanoindentation experiments in chapter 3.

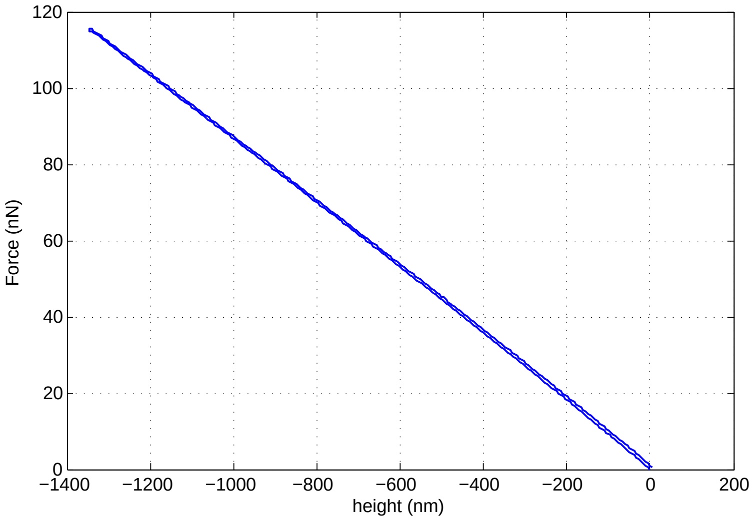

Figure 5.10: Force-distance curve calculated utilizing Sader’s formula based on the data obtained in Figure 5.9

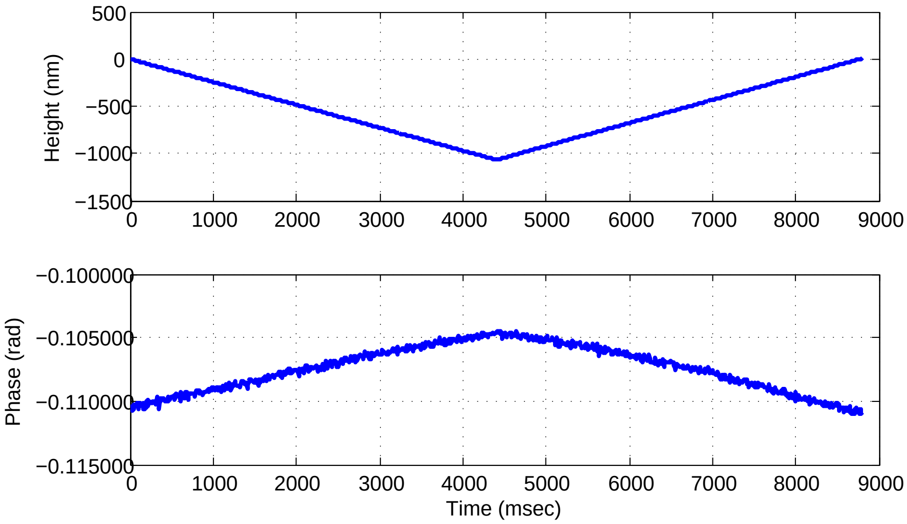

Figure 5.11: Data from another micropillar pushing experiments. Change of probe height vs. time plot during mechanical deflection (top graph) and change of phase vs. time plot (bottom graph)

Figure 5.12 presents the change of phase data with respect to the probe tip from another deflection experiment where the pillar is pushed at the top in the total of 1066 nm. The corresponding force-distance curve generated by this experiment is given in Figure 5.12.

In the next section, an introduction is given to mechanical models that will be used to estimate bending behaviors of micropillar structures and verify the experimental results.

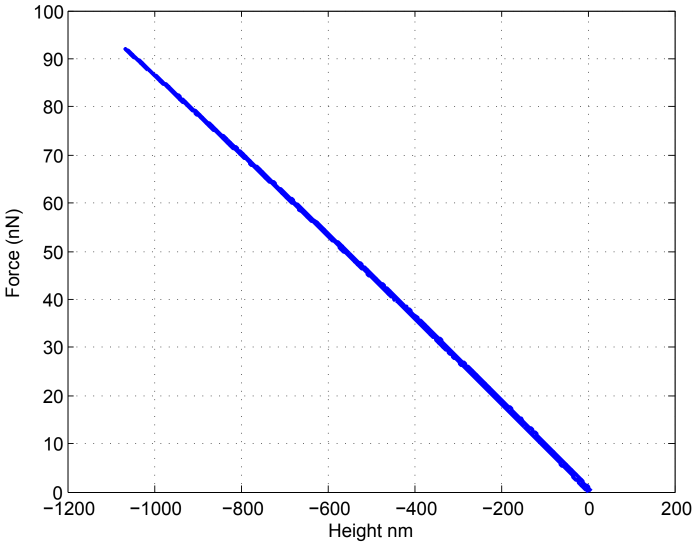

Figure 5.12: Computed Force-distance diagram by Sader formula from the experiment in Figure 5.11

5.4 The mechanical models used for micropillar deflection experiments

In order to verify the F-D curves obtained during deflection experiments, various mechanical models have been investigated. These include Euler-Bernoulli beam deflection theory [87], Timoshenko beam theory [88], and finite element simulation models. Finite element models include Linear Elastic Model and Hyperelastic models such as Mooney-Rivlin elastic model. This section is devoted to the introduction of these models to the reader. The comparison of each model with respect to the experimentally obtained F-D curves will be presented in the next section.

5.4.1 Beam Deflection Theories

There are two well-known beam deflection theories for modeling cantilever structured beams such as given in Figure 5.13. The first model is called Euler-Bernoulli Beam Deflection Theory (EBBDT) [87]. It was proposed by both Euler and Bernoulli and derived according to three a priori assumptions.

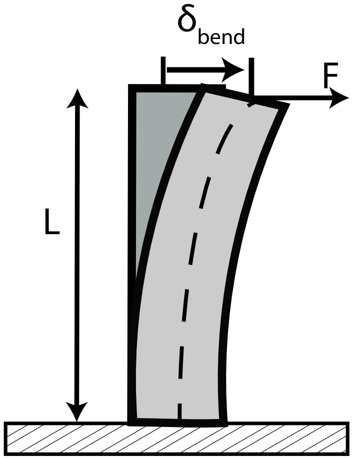

Figure 5.13: Elastic pillar deflection induced by lateral force F on top

In this theory, the first assumption is that the cross-section of the cantilevered body is rigid on its plane which means that there is no deformation of the cross-section during bending of the structure. The second assumption is that the cross-section rotates around a neutral surface (indicated with dash lines in Figure 5.13). The third assumption is that the cross-section remains perpendicular to the neutral surface during deformation. Based on these assumptions, if a lateral force F is applied at the end of the cantilever, one can write a force-displacement formula such as given in eq. 5.2. In this equation, E is the elastic modulus of the material that the cantilever is made, I is the second moment of inertia, L is the length of the pillar and δ_{bend} is the displacement occurring due to the bending of the cantilever.

$$F = \frac{3EI}{L^3}\delta_{bend} \tag{5.2}$$

The moment of inertia for circular cross section structures is $I = \frac{\pi R^4}{4}$ where R represents the radius of the micropillar.

The second well-known beam deflection theory is called Timoshenko beam theory (TBT) [88]. Timoshenko beam theory relaxes the third assumption of the EBBDT and it is assumed that the cross-section is no longer constrained to remain perpendicular to the neutral axis but it can rotate around it. Therefore, it accounts for shear deformation effect as shown in Figure 5.14 that is $\delta_{pillar} = \delta_{bend} + \delta_{shear}$.

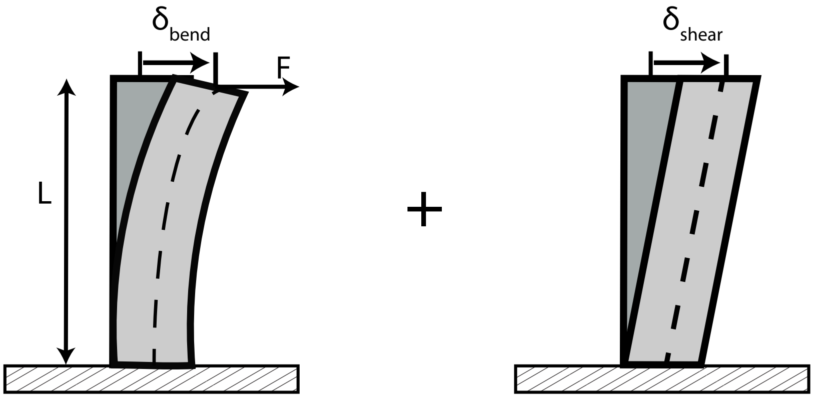

Figure 5.14: Schematic illustrating elastic pillar deformation for Timoshenko model including shear deformation

The relationship between applied lateral force F and the total pillar displacement for Timoshenko's beam theory,$delta_{pillar}$ is given in eq. 5.3.

$$\delta_{pillar} = (\frac{3EI}{L^3} + \frac{KGA}{L})F \tag{5.3}$$

Where $A = \pi R^2$ and represents the cross-sectional area of circular micropillar, G is the shear modulus given as $G = \frac{E}{2(1+\nu)}$ and ν is the poisson's ratio of the material, K is called Timoshenko's shear coefficient and is expressed as $K = \frac{6+6\nu}{7+6\nu}$.

In the next section, modified Euler beam model developed for size-dependent behavior of micro cantilever structures is introduced.

5.4.2 Scaling Effect on Beam Deflection Models

It has been proposed by several studies that conventional beam deflection models such as Euler beam theory might suffer estimating the deflection behavior of micro-structures in the micrometer scale regime. This effect is called *size-dependent behavior* and it is due to contributions from strain gradients during the deformation of the micro-structure [89], [90].

Park and Gao extends Euler beam model based on the modified stress theory [90]. They present the modified Euler beam formula that includes the *size effect parameter* l such as given in eq. 5.4.

$$\delta(x) = \frac{Fx^2}{6(EI + GAl^2)}(3L - x) \tag{5.4}$$

where $\delta(x)$ represents the deflection of the beam at a distance x from the bottom.

The length scale parameter (l) can be found from bending rigidity $D^{'}$ by the formula given in eq. 5.5.

$$D^{'} = \frac{EI + GAl^2}{bh^3} \tag{5.5}$$

where b and h represent the width and the thickness of a cantilever beam. One can find the bending rigidity $D^{'}$ from experimental load vs normalized deflection curve as proposed by Lam et al. [89]. Figure 5.15 presents a representative curve obtained by Lam et al. for several aspect ratios of cantilever structures [89].

In this Figure, h/a represents the aspect ratio of the cantilever and w_0 represents the displacement of the cantilever upon the load Q. Once bending rigidity $D^{'}$ is determined in a similar fashion to Figure 5.15, one can find the scaling parameter l to be used in eq. 5.4.

In the next section, constitutive models used in COMSOL Finite-Element-Analysis tool are introduced.

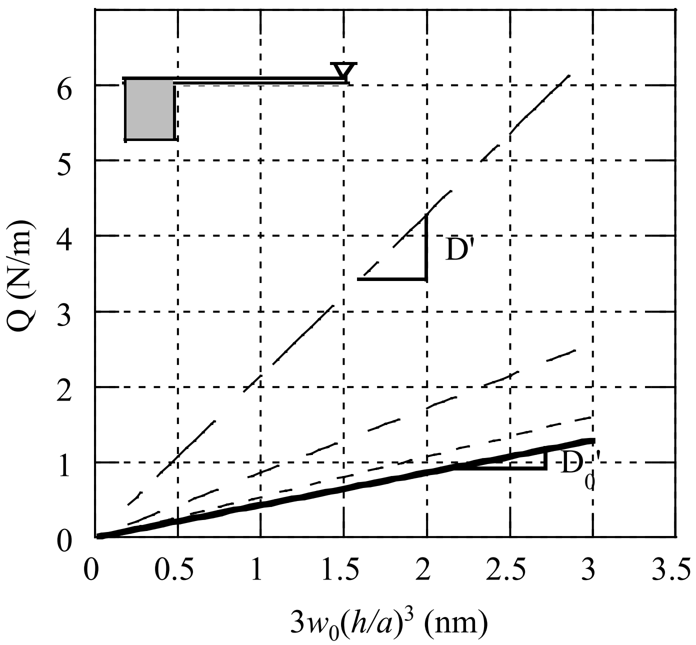

Figure 5.15: Load vs normalized deflection curve obtained by Lam et al. for different aspect ratio of microcantilevers to determine bending rigidity D'

5.5 Linear Elastic and Hyperelastic Constitutive Models

When a stress is applied to a material, most of the materials show a linear stress and strain relationship up to a level. When the applied stress is proportional to the strain, the material is said to be a linear elastic material. The constitutive equation (the equation representing how material behaves e.g. the relation between stress and strain) for a linear elastic material is called *Hooke's law* and it is given by $\sigma = E\epsilon$, where σ is stress and ϵ is strain. For an isotropic material, this equation can be extended into both uniaxial and shear stresses as follows:

$$
\begin{aligned}
\epsilon_{11} &= \frac{1}{E}[\sigma_{11} - \nu(\sigma_{22} + \sigma_{33})], \\
\epsilon_{22} &= \frac{1}{E}[\sigma_{22} - \nu(\sigma_{33} + \sigma_{11})], \\
\epsilon_{33} &= \frac{1}{E}[\sigma_{33} - \nu(\sigma_{11} + \sigma_{22})], \\
\epsilon_{12} &= \frac{\sigma_{12}}{2\mu}, \\
\epsilon_{23} &= \frac{\sigma_{23}}{2\mu}, \\
\epsilon_{31} &= \frac{\sigma_{31}}{2\mu},
\end{aligned}
\tag{5.6}
$$

For σ_{ij}, i and j represent principal coordinate system axes.

For a finite-element-analysis (FEA) simulation, these equations are applied to very small finite elements created by meshing algorithms of the entire geometry.

For polymer materials although Linear Elastic (LE) material model could be valid for very small strains, after a certain point due to the large deformation of polymers, the stress and strain relations will exceed proportional limit and LE model will not suffice. In this case, Hyperelastic constitutive models can be used in order to predict mechanical behavior of polymer materials. There are various models in the literature that are proposed for polymer materials such as Mooney-Rivlin model [91], [92] , Ogden model [93], Yeoh model [94].

Several studies have investigated and compared these models for PDMS material. Yu and Zhao investigate deformation of PDMS membrane and a PDMS microcantilever by utilizing above mentioned hyperelastic models and compare the results with linear elastic constitutive model [95]. Their findings show that linear elastic model is sufficient for estimating small deflections on PDMS micro-structures. However, for larger displacements hyperelastic modeling is needed. For larger displacement regime, Mooney-Rivlin model is used. In another study, Kim et al. performed various characterization experiments such as tensile test and fit the data to well-known hyperelastic models [96]. Their results indicate that Ogden model is preferable for analyzing the PDMS structures for all ranges of deformation including tensile and compressive regimes. Gao et al. reported similar findings to Yu and Zhao that Mooney-Rivlin model matches deformation data for all range of materials and is a suitable model for PDMS deformation experiments [97], [95].

Due to simple correlation of its model parameters to the fundamental material properties e.g. elastic modulus, Mooney-Rivlin model is selected for our micropillar deflection modeling and a brief introduction is given next. Let W be the strain energy density function for PDMS. For Mooney-Rivlin model and PDMS, W is a function of the three strain invariants I_1, I_2, and I_3 such as given in eq. 5.7.

$$W = W(I_1, I_2, I_3) \tag{5.7}$$

where $I_1 = tr\mathbf{C}, I_2 = [(tr\mathbf{C})^2 - tr\mathbf{C}^2]/2, I_3 = 1$ and $\mathbf{C}$ is the right Cauchy-Green deformation tensor.

The stress tensor can be written as in eq. 5.8

$$\mathbf{S} = \frac{\partial W}{\partial \mathbf{E}} = 2\frac{\partial W}{\partial \mathbf{E}} \tag{5.8}$$

where $\mathbf{S}$ is the second Piola-Kirchhoff stress tensor, $\mathbf{E}$ is the Green strain tensor. A relationship between $\mathbf{E}$ and $\mathbf{C}$ can be written as:

$$\mathbf{E} = \frac{1}{2}(\mathbf{C} - \mathbf{I}) \tag{5.9}$$

where $\mathbf{I}$ is the second-order unit tensor. If the material is incompressible, $I_3 = 1$ meaning that there is no strain occurring in Z-direction. In this case, the strain energy density function W can be written as a polynomial function of $(I_1 - 3)$ and $(I_2 - 3)$ such as given in eq. 5.10.

$$W = c_1(I_1 - 3) + c_2(I_2 - 3) \tag{5.10}$$

where c_1 and c_2 are material constants and can be related to shear modulus G

or elastic modulus E for infinitely small deformations as given in eq. 5.11.

$$G = \frac{E}{2(1+\nu)} = 2(c_1 + c_2) \tag{5.11}$$

Numerical analysis using built-in COMSOL model uses strain density function in eq. 5.10 for Mooney-Rivlin model and requires c_1 and c_2 parameters as an input [98].

In the next section, comparisons of experimental models introduced in this section are presented with respect to experimentally obtained force-distance curve results.

5.6 Comparison of experimental results with mechanical models

In this section, force-distance curve results obtained on a micropillar deflection experiment is compared with mechanical models. The analytical models that are introduced in the previous sections such as Euler-Bernoulli and Timoshenko beam models are implemented for the specific geometry of micropillar dimension. Additionally, numerical simulations are performed using COMSOL finite-element-analysis tool. The micropillar is modeled as either with COMSOL Linear Elastic Material model or Mooney-Rivlin Hyperelastic Material model.

Figure 5.16 presents five different mechanical models and one of the deflection experiment data obtained on the pillar with dimensions measured as $D = 8.9\mu m$, $L = 24\mu m$. Micropillars are fabricated in the same preparation conditions and held for PDMS nanoindentation experiments. The elastic modulus of PDMS is taken as 0.8 MPa based on our experimental findings in Chapter 4.

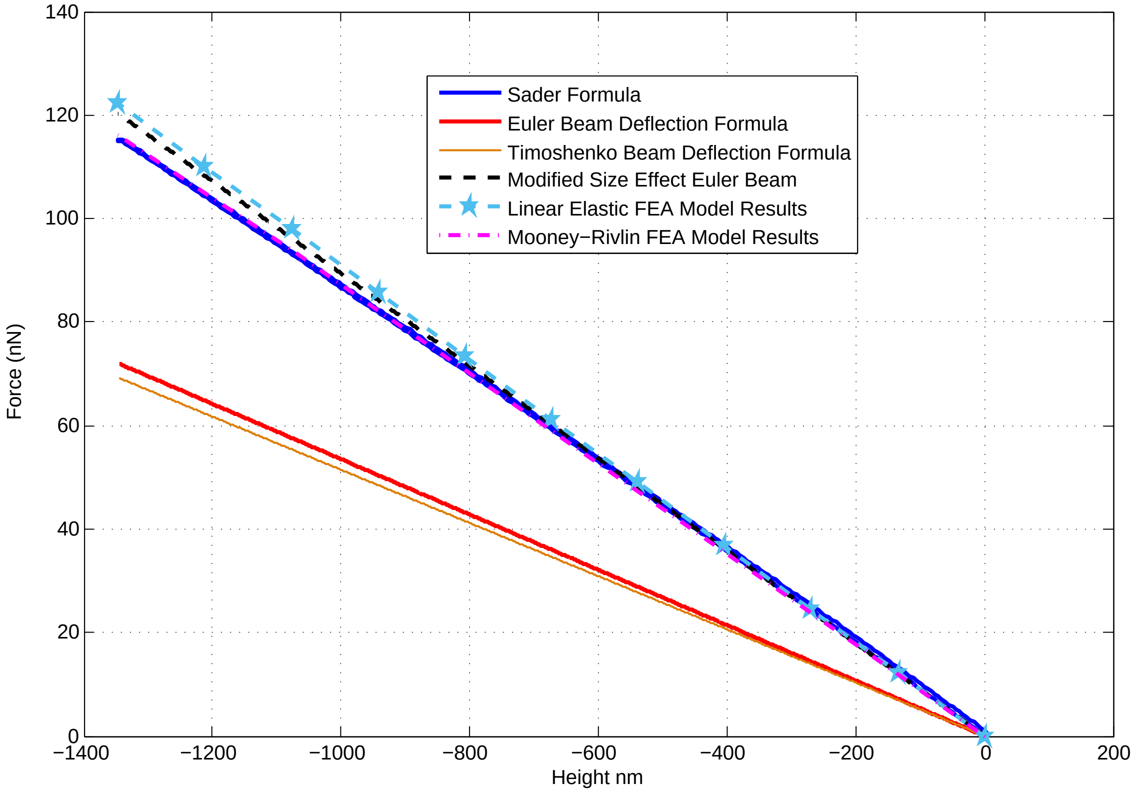

Figure 5.16: Comparisons of mechanical models with the experimental result

The calculated root mean square error (RMSE) values with respect to experimental results is given in Table 5.1.

Table 5.1: Root mean square errors of mechanical models calculated for each model with respect to the experimental result.

Mechanical Model	***RMSE***
Mooney-Rivlin Hyperelastic Model	0.8955
Mod. Size Effect Euler Beam Formula	1.9957
Linear Elastic Model	3.0185
Euler Beam Formula	26.1677
Timoshenko Beam Formula	28.1765

It has been found that FEA models such as Linear Elastic Model can estimate the mechanical behavior of micropillar more accurately. Although Linear Elastic Model performs better for small deflections, it diverges from the actual experimental data as the displacement gets larger. On the other hand, Mooney-Rivlin Hyperelastic model is in very close agreement with our experimental data with an RMSE value of 0.8955 indicating that Hyperelastic models can be a better fit for a full range of deflection experiments. As compared to the FEA models, the standard beam deflection models such as Euler and Timoshenko diverges from experimental data as the RMSE values indicate. Implementing modified Euler Beam formula that was discussed in the previous section gives a better estimation and indicates the size effect considerations for small scale beam deflection experiments.

Figure 5.17 shows PDMS micropillar modeled in COMSOL simulation environment with the exact dimensions of the pillar that the experimental data is obtained in Figure 5.16. Free tetrahedral shape user-defined meshing profile is created with default fine mesh element size on the pillar structure and coarse mesh element size on the remainder of the geometry. A prescribed uniaxial displacement is applied incrementally on the top of the pillar auxiliary sweep study extension option in the solver configuration. Reaction forces are calculated on the surface of the pillar by integral operators after the simulation is completed. The tip displacement is read by point operator and displacement expression element for a reference point selected on the tip of the micropillar. Together with the reaction force operator values, the results are tabulated and exported into a text file for an input to be read in MATLAB environment.

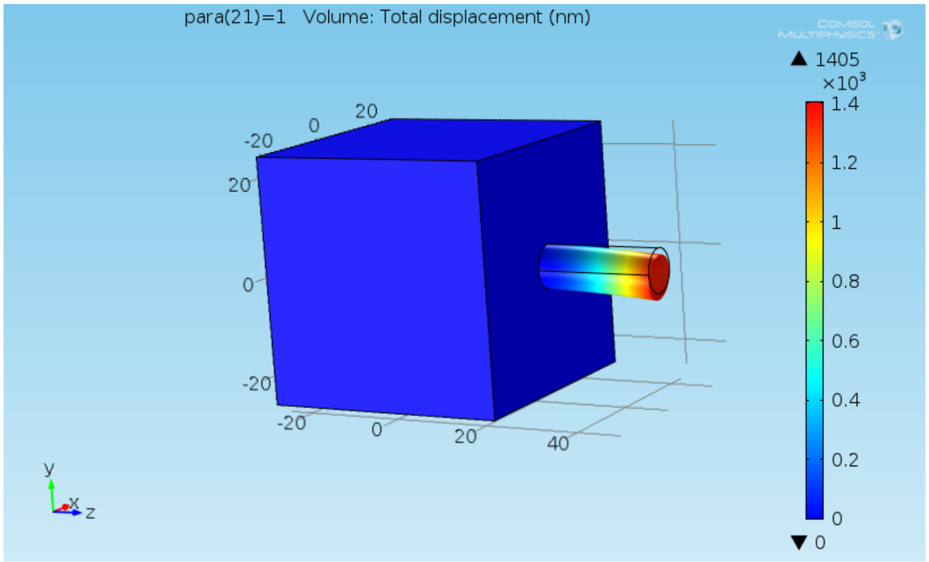

Figure 5.17: Deflection of PDMS pillar (1395 nm) modeled in COMSOL as Linear Elastic or Mooney-Rivlin Hyperelastic Material Model

In summary, micropillar mechanical characterization experiments have been performed with a novel approach by utilizing tuning fork probe sensors as a force sensor. Experimental force-distance curves have been compared with well-known mechanical models. It has been found that the PDMS elastic modulus value estimated through our novel nanoindentation experiments were accurate and in good agreement with the force-distance data. In addition, the conventional beam formulas are not sufficient when it comes to estimating the mechanical behavior of PDMS micropillar. Therefore, during FEA simulations Hyperelastic Material Models such as Mooney-Rivlin is suggested. If classical bending models are used, one should include the scaling effect modifications into the model since conventional beam models are found to underestimate the deflection results as it was also presented by other studies in the literature.

In the next section, an application of PDMS micropillar sensors as a force sensor is presented for a biomedical application in order to measure cancer cell traction forces.

5.7 The use of PDMS micropillars as a force sensor to quantify cancer cell traction forces

In order to demonstrate the applicability of our microfabricated pillar structures as a force sensor to quantify cellular traction forces for cancer cells,

$5\mu m$ diameter, $20\mu m$ height and $5\mu m$ spacing micropillar arrays are fabricated. To create a thin and uniform layer of PDMS micropillar arrays, PDMS is spin coated on silanized molds as shown in Figure 5.18.

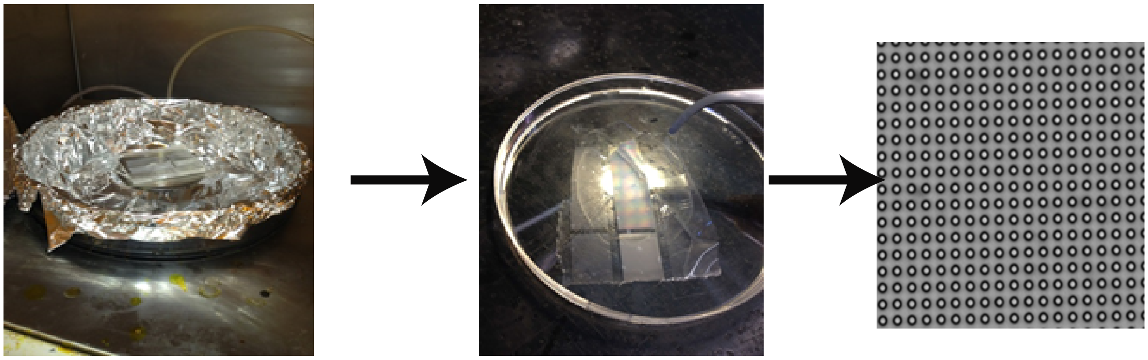

Spin Coating of PDMS

The peeled off PDMS micropillar array

Microscope image of 5 µm diameter pillar

Figure 5.18: Spin coating process of thin layer PDMS micropillar array for

Before culturing HCT 116 colorectal cancer cell on top of the micropillars, the micropillars are plasma treated for 7 mins to make the pillar surface hydrophilic. This is done in order to facilitate the next step of cell seeding which includes fibronectin protein coating of pillars. After plasma treatment with a corona treater for 10 mins (Electro-Technic Products Inc model BD-20AC), 500 $\mu g/mL$ of fibronectin (Life sciences) is introduced on the top of the PDMS micropillar substrate. Subsequently, the device is submerged into 70 % ethanol for 5 mins to sterilize and washed with phosphate buffered saline (PBS) solution for 5 mins to remove ethanol. The cells are detached from the culture flask by trypsin and a low concentration of cells inside the culture medium are micropipetted onto the micropillars.

Figure 5.19 shows an image taken where HCT-116 cells incubated on the top of the micropillars after 45 minutes. The image is taken with Zeiss AxioVision upright microscopy with a 20x objective.

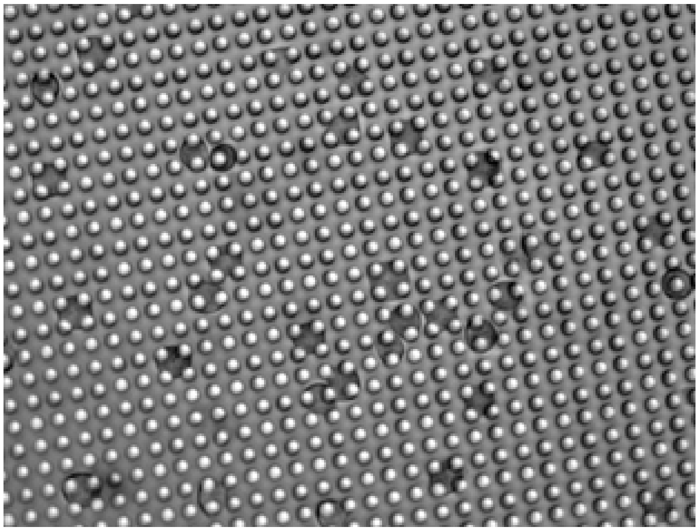

Figure 5.19: HCT-116 cells seeded on top of the fibronectin coated micropillars. Image taken after 45 minutes of incubation time

Figure 5.20 presents an image taken after 24 hours of incubation time. As it can be seen, some of the cells are well attached to the pillar substrates and able to pull or push them.

In order to quantify the deflection of pillars, image processing algorithms are employed and implemented in MATLAB. By utilizing circle detection algorithms provided by MATLAB [99], circular Hough transform is performed on the images in order to detect circles and the centroids of the pillars. Circular Hough transform looks for high gradient foreground pixels that might be the possible edge of the circles in images. The algorithm

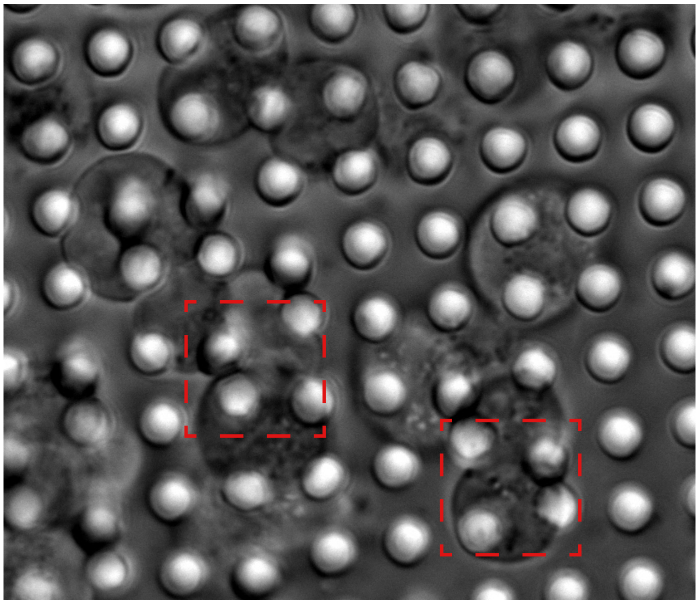

Figure 5.20: HCT-116 cells seeded on top of the fibronectin coated micropillars. Image taken after 24 hours of incubation time. The cells are able to either push or pull the micropillar force sensors

initially generates an accumulator array candidate pixels and implement a voting mechanism between these pixels for a form array with full circle of fixed radius. Figure 5.21(a) demonstrates the accumulator array generated after circular Hough transform is completed for the image shown in Figure 5.20. Figure 5.21(b) shows the circles detected by the algorithm marked as blue and their centroid locations marked as red cross.

Figure 5.22 demonstrates the deflection values of some of the micropillars obtained by calculating the pixel shifts of centroid locations with respect to a line fitted to unperturbed pillar centroids. The pixel to distance ratio is calculated by measuring the average circle diameters which corresponds to $5\mu m$ diameter for the pillars. The force curve demonstrated in Figure 5.22

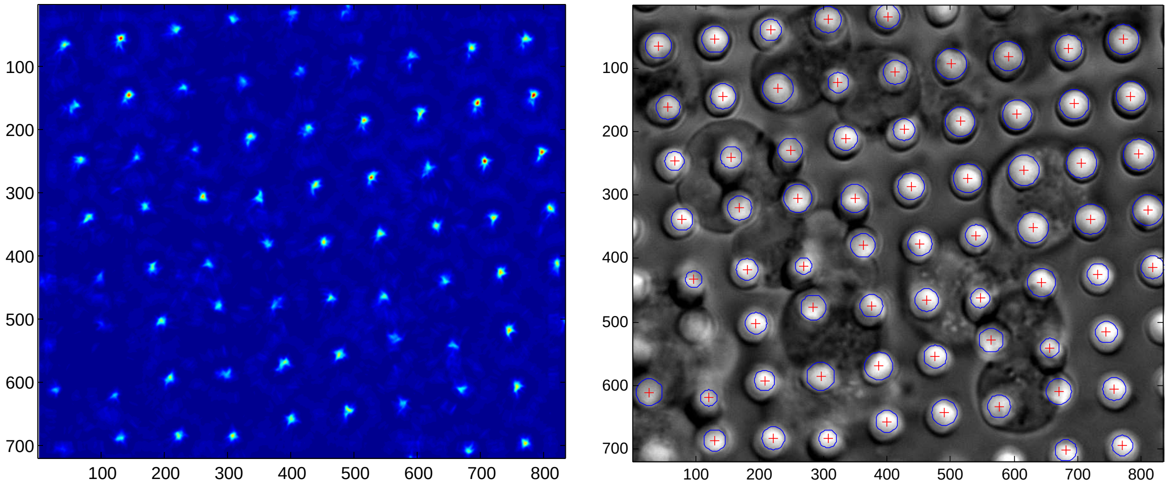

(a) Accumation gradient array resulted from Circular Hough Transform (b) Detected circles marked with blue and their centroid locations amrked with red cross

Figure 5.21: Results of Circular Hough Transform on detecting optical deflection of micropillar arrays by HCT116 cancer cells migration

is generated by utilizing modified Euler Beam formula with a displacement parameter calculated from the pixel shifts in the image (1382 nm).

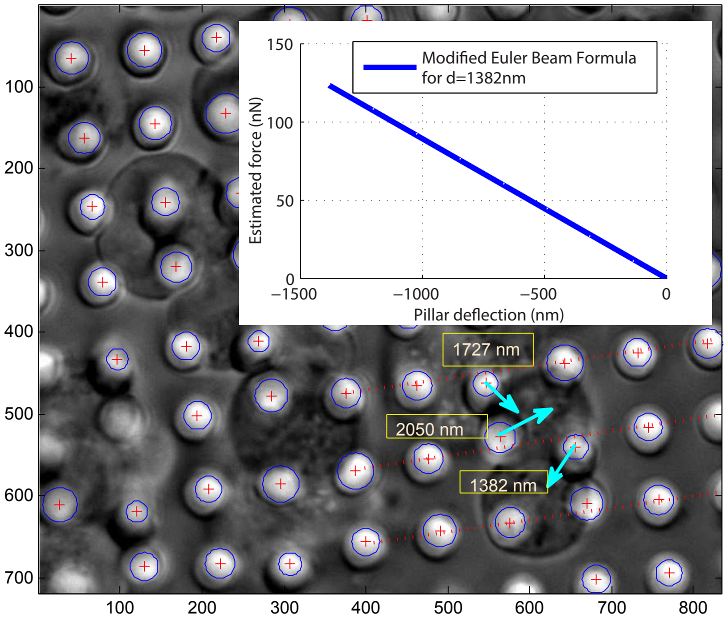

Figure 5.22: Quantification of pillar deflections created by HCT 116 cancer cell forces

As given in Figure 5.22, the calculated force value of corresponding pillar deflection utilizing modified Euler beam formula (eq. 5.4) are within the range of our mechanical characterization experiments and show the viability of our techniques that are developed in this dissertation work. Furthermore, as a reference work for comparison, our force level estimates also fall within the same range of force levels that are presented in [100]. Lea et al. investigate mechanosensing mechanism of cell adaption with varying substrate stiffness [100]. Fibroblast REF52 cell type is used. Micropillar structures out of PDMS are fabricated with pillar diameter ranging from $2\mu m$ to $4\mu m$ and center-to-center distance of $4\mu m$. The stiffness of the PDMS micropillars are adjusted by changing the height dimension of the elastic modulus of PDMS together with varying cross linking ratio from 3.3 $\%$ to 10 $\%$. Their elastic moduli estimations that correspond to varying crosslink ratios are $E = 0.3\ MPa$ to $1.8\ MPa$.

Figure 5.23 demonstrates the results obtained by Lea et al. for measuring the cell traction forces of fibroblast cells on varying substrate stiffness created by different aspect ratios and cross-linking ratios. Since the force values are calculated based on the simple Euler beam deflection formula that is given in eq. 5.2, we anticipate that their values are underestimated due to the insufficient mechanical model employed according to our findings in this Chapter.

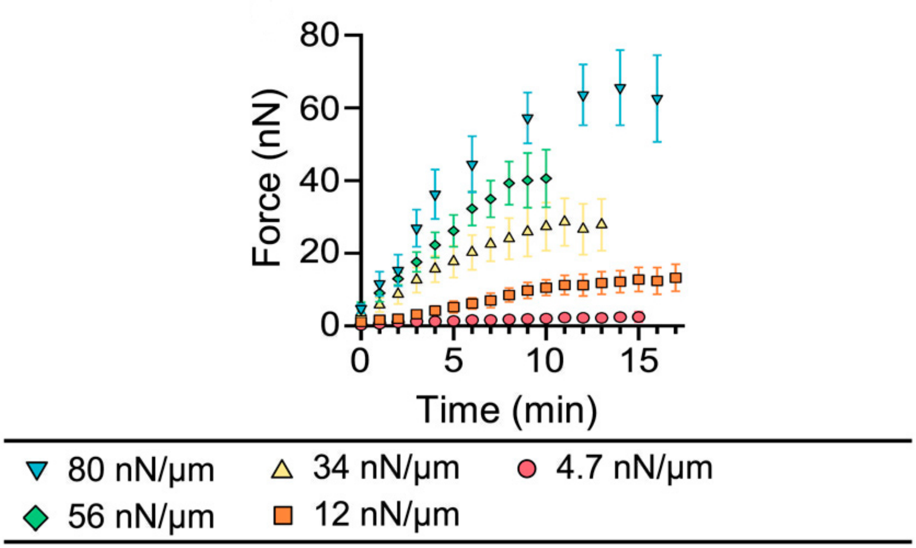

Figure 5.23: Example reference work reporting the force values calculated for fibroblast cells on varying substrate stiffness [100]

Chapter 6

Conclusions and Future Work

Some of the limitations on currently available characterization tools and accurate mechanical models of micro-structures are among the limiting factors for product development of MEMS devices. With the motivations of developing improved tools and techniques and providing advances in the material characterization field, this dissertation work has the following contributions:

- A novel approach to nanoindentation has been developed with a multi-probe (SPM) system. This new approach has an ultra-resolution in depth sensing and alleviates the drawbacks of current nanoindentation techniques performed particularly with atomic-force-microscopy (AFM) system on hard materials.
- Different than multi-probe nanoindentation where static deflection of indenter tuning-fork is sensed by another probe to determine force levels, dynamic nanoindentaion methods are employed on characterization of soft materials utilizing soft material tuning-fork indentation

probes. In dynamic nanoindentation approaches, force values are extracted by employing force spectroscopy models which are based on the perturbation of the oscillating tuning forks at resonance frequency. Frequency-modulation (FM) technique is used to extract force values during nanoindentation. By this way, higher force resolution is achieved and significant improvement in the contact detection is provided.

- Ultra sensitive tuning fork force sensors are utilized in mechanical characterization of PDMS micropillar structures. These microstructures have been commonly used in many biomedical studies as force sensors. A through investigation of mechanical models for comparison with the experimental data is performed.

The multi-probe approach that is developed in this dissertation work can be easily integrated into environments where integration of laser-based displacement mechanism might be complicated. These include cryogenic chambers or ultra-high vacuum environments.

Furthermore, ability to use up to four probes can bring more advantages such as simultaneous operation of the probes where additional two probes can be used for different types of measurements such as electrical or thermal measurements during nanoindentation of the specimen. With gold coated glass fiber tips that can be mounted on tuning fork probes, electric voltages can be supplied and measured so that resistivity characteristics of the materials can be extracted during nanoindentation. With the help of thermoresistive probes, the sample surface can be heated and nanoindentation experiments can be performed at the same time.

Note that since the multi-probe technique relies on the deflection of tuning fork probe and these probes have higher spring constants as compared to the most of the conventional AFM cantilever probes, there will be a measurement limitation depending on the material compliance. Especially measuring of the static deflection on soft materials might not be effectively performed. Finding of a threshold value is also among the future work of the proposed multi-probe nanoindentation technique.

Another important extension of this dissertation work is to utilize dual-probe operation with side-wall imaging capability. For example, instead of tilting the micropillars 90 degrees and performing pushing experiments, with specially designed mounting apparatus and change of feedback signal connections, tuning forks can be tilted 90 degrees and perform side-wall AFM imaging. While one of the probes can push the micropillar, the other one can perform side-wall AFM scanning so that radius of curvature and displacement values can be measured with a very high accuracy. With the high resolution force sensing capability demonstrated in this work, one can measure the deflection of the micropillars for the ultra-small force levels and compare the deflection behaviors with the mechanical models that are investigated in this dissertation work.

As an application of micropillar force sensors, preliminary results to cell traction force microscopy is presented. The results show the viability of the developed characterization techniques and its application into cell traction forces to detect cancer cell forces.

Among the future work and possible envisioned extension of this application include the application of PDMS micropillars for quantifying inflammation induced cancer cell traction forces. There is a growing interest in the biomedical engineering field on measuring cell traction forces for cancer cells in order to investigate the dynamics of cancer metastasis [101], [102], [103]. The factors that are regulating these forces for cancer cells are still not completely understood and inflammation is considered as one of them. Therefore, by introducing inflammation cytokines e.g. TNF-α into micropillar cell culturing environment, these forces can be quantified. With the effective tools and techniques that are developed in this dissertation work, more accurate quantification of force levels can be obtained.

In addition to application of polymeric micropillar arrays as force sensors, they can be used in other sensing applications such as a humidity sensor. Recently, Wang et al. demonstrated PMMA micropillar arrays as an ultra-sensitive humidity sensor [104]. Polymeric PMMA micropillars fabricated on top of a quartz crystal substrate enhances detection of humidity through water molecules adsorbed on top of the PMMA micropillars. The adsorbed water molecules eventually causes an increase in the resonance frequency shift which can be correlated into humidity. Similar to the force sensing application, mechanical characterization of PMMA micropillar sensors is also crucial so that accurate sensor models can be developed.

Bibliography

[1] M. L. Oyen, "Nanoindentation of biological and biomimetic materials," *Exp. Tech.*, vol. 37, no. 1, pp. 73–87, 2013.

[2] D. M. Ebenstein and L. A. Pruitt, "Nanoindentation of biological materials," *Nano Today*, vol. 1, pp. 26–33, Aug. 2006.

[3] S. E. Cross, Y.-S. Jin, J. Rao, and J. K. Gimzewski, "Nanomechanical analysis of cells from cancer patients," *Nat. Nanotechnol.*, vol. 2, pp. 780–783, Dec. 2007.

[4] W. Gindl, H. S. Gupta, T. Schöberl, H. C. Lichtenegger, and P. Fratzl, "Mechanical properties of spruce wood cell walls by nanoindentation," *Appl. Phys. A*, vol. 79, no. 8, pp. 2069–2073, 2004.

[5] J. D. Kaufman and C. M. Klapperich, "Surface detection errors cause overestimation of the modulus in nanoindentation on soft materials," *J. Mech. Behav. Biomed. Mater.*, vol. 2, pp. 312–317, Aug. 2009.

[6] D. G. Yablon, *Scanning probe microscopy for industrial applications: nanomechanical characterization*. John Wiley & Sons, 2013.

[7] Y. Sun, B. Akhremitchev, and G. C. Walker, "Using the adhesive interaction between atomic force microscopy tips and polymer surfaces to measure the elastic modulus of compliant samples," *Langmuir*, vol. 20, no. 14, pp. 5837–5845, 2004.

[8] M. E. Dokukin and I. Sokolov, "On the measurements of rigidity modulus of soft materials in nanoindentation experiments at small depth," *Macromolecules*, vol. 45, no. 10, pp. 4277–4288, 2012.

[9] J. Ren and Q. Zou, "A Control-Based Approach to Accurate Nanoindentation Quantification in Broadband Nanomechanical Measurement Using Scanning Probe Microscope," *IEEE Trans. Nanotechnol.*, vol. 13, no. 1, pp. 46–54, 2014.

[10] S. R. Cohen and E. Kalfon-Cohen, "Dynamic nanoindentation by instrumented nanoindentation and force microscopy: a comparative review," *Beilstein J. Nanotechnol.*, vol. 4, no. 1, pp. 815–833, 2013.

[11] "Nanonics Imaging Ltd," 2015.

[12] K. Fukui, H. Onishi, and Y. Iwasawa, "Atom-resolved image of the TiO 2 (110) surface by noncontact atomic force microscopy," *Phys. Rev. Lett.*, vol. 79, no. 21, p. 4202, 1997.

[13] D. W. Evans, N. A. Vavalle, R. DeVita, P. Rajagopalan, and J. L. Sparks, "NanoIndentation Device for Investigating the Mechanics of Compliant Materials," *Exp. Mech.*, vol. 53, pp. 217–229, May 2012.

[14] B. K. Nowakowski, D. T. Smith, S. T. Smith, L. F. Correa, and R. F. Cook, "Development of a precision nanoindentation platform," *Rev. Sci. Instrum.*, vol. 84, p. 075110, July 2013.

[15] V. Oiko, B. Martins, P. Silva, V. Rodrigues, and D. Ugarte, "Development of a quartz tuning-fork-based force sensor for measurements in the tens of nanoNewton force range during nanomanipulation experiments," *Rev. Sci. Instrum.*, vol. 85, p. 035003, Mar. 2014.

[16] H. Huang, H. Zhao, J. Mi, J. Yang, S. Wan, L. Xu, and Z. Ma, "A novel and compact nanoindentation device for in situ nanoindentation tests inside the scanning electron microscope," *AIP Adv.*, vol. 2, p. 012104, Mar. 2012.

[17] J. Falter, M. Stiefermann, G. Langewisch, P. Schurig, H. Hölscher, H. Fuchs, and A. Schirmeisen, "Calibration of quartz tuning fork spring constants for non-contact atomic force microscopy: direct mechanical measurements and simulations," *Beilstein J. Nanotechnol.*, vol. 5, no. 1, pp. 507–516, 2014.

[18] S. L. Crick and F. C.-P. Yin, "Assessing Micromechanical Properties of Cells with Atomic Force Microscopy: Importance of the Contact Point," *Biomech Model Mechanobiol*, vol. 6, pp. 199–210, June 2006.

[19] H. Hertz, "On the contact of solid elastic bodies," *J. reine und Angew. Math.*, vol. 92, pp. 156–171, 1881.

[20] W. C. Oliver and G. M. Pharr, "Measurement of hardness and elastic modulus by instrumented indentation: Advances in understanding and refinements to methodology," *J. Mater. Res.*, vol. 19, no. 1, pp. 3–20, 2004.

[21] Y. Qin and R. Reifenberger, "Calibrating a tuning fork for use as a scanning probe microscope force sensor," *Rev. Sci. Instrum.*, vol. 78, no. 6, p. 63704, 2007.

[22] F. Sansoz and T. Gang, "A force-matching method for quantitative hardness measurements by atomic force microscopy with diamond-tipped sapphire cantilevers," *Ultramicroscopy*, vol. 111, no. 1, pp. 11–19, 2010.

[23] "Corning Ltd Eagle Glass 2000 Material Information," 2015.

[24] M. A. Hopcroft, W. D. Nix, and T. W. Kenny, "What is the Young's Modulus of Silicon?," *Microelectromechanical Syst. J.*, vol. 19, no. 2, pp. 229–238, 2010.

[25] E. Cinar, F. Sahin and D. Yablon, "Development of a Novel Nanoindentation Technique by Utilizing a Multi-probe AFM System," *Beilstein J. Nanotechnol.*

[26] E. Cinar and F. Sahin, "New approach for nanoindentation using multiprobe AFM system," in *IEEE 14th Int. Conf. Nanotechnol.*, pp. 49–53, 2014.

[27] J. C. Acosta, G. Hwang, J. Polesel-Maris, and S. Régnier, "A tuning fork based wide range mechanical characterization tool with nanorobotic manipulators inside a scanning electron microscope," *Rev. Sci. Instrum.*, vol. 82, no. 3, p. 35116, 2011.

[28] J. E. Sader and S. P. Jarvis, "Accurate formulas for interaction force and energy in frequency modulation force spectroscopy," *Appl. Phys. Lett.*, vol. 84, no. 10, pp. 1801–1803, 2004.

[29] S. J. O'shea and M. E. Welland, "Atomic force microscopy at solid-liquid interfaces," *Langmuir*, vol. 14, no. 15, pp. 4186–4197, 1998.

[30] S. Hu and A. Raman, "Inverting amplitude and phase to reconstruct tip sample interaction forces in tapping mode atomic force microscopy," *Nanotechnology*, vol. 19, no. 37, p. 375704, 2008.

[31] H. Hölscher, "Quantitative measurement of tip-sample interactions in amplitude modulation atomic force microscopy," *Appl. Phys. Lett.*, vol. 89, no. 12, p. 123109, 2006.

[32] A. J. Katan, M. H. Van Es, and T. H. Oosterkamp, “Quantitative force versus distance measurements in amplitude modulation AFM: a novel force inversion technique,” *Nanotechnology*, vol. 20, no. 16, p. 165703, 2009.

[33] M. Lee and W. Jhe, “General theory of amplitude-modulation atomic force microscopy,” *Phys. Rev. Lett.*, vol. 97, no. 3, p. 36104, 2006.

[34] F. J. Giessibl, “Forces and frequency shifts in atomic-resolution dynamic-force microscopy,” *Phys. Rev. B*, vol. 56, no. 24, p. 16010, 1997.

[35] T. R. Albrecht, P. Grütter, D. Horne, and D. Rugar, “Frequency modulation detection using high-Q cantilevers for enhanced force microscope sensitivity,” *J. Appl. Phys.*, vol. 69, no. 2, pp. 668–673, 1991.

[36] U. Dürig, “Relations between interaction force and frequency shift in large-amplitude dynamic force microscopy,” *Appl. Phys. Lett.*, vol. 75, no. 3, pp. 433–435, 1999.

[37] J. Otero, R. Baños, L. González, E. Torrents, A. Juárez, and M. Puig-Vidal, “Quartz tuning fork studies on the surface properties of Pseudomonas aeruginosa during early stages of biofilm formation,” *Colloids Surfaces B Biointerfaces*, vol. 102, pp. 117–123, 2013.

[38] J.-O. Abrahamians, B. Sauvet, J. Polesel-Maris, R. Braive, and S. Regnier, “A nanorobotic system for in situ stiffness measurements on membranes,” *Robot. IEEE Trans.*, vol. 30, no. 1, pp. 119–124, 2014.

[39] G. H. Simon, M. Heyde, and H.-P. Rust, “Recipes for cantilever parameter determination in dynamic force spectroscopy: spring constant and amplitude,” *Nanotechnology*, vol. 18, no. 25, p. 255503, 2007.

[40] T. Fujii, “PDMS-based microfluidic devices for biomedical applications,” *Microelectron. Eng.*, vol. 61, pp. 907–914, 2002.

[41] E. Leclerc, Y. Sakai, and T. Fujii, “Microfluidic PDMS (polydimethylsiloxane) bioreactor for large-scale culture of hepatocytes,” *Biotechnol. Prog.*, vol. 20, no. 3, pp. 750–755, 2004.

[42] A. Mata, A. J. Fleischman, and S. Roy, “Characterization of polydimethylsiloxane (PDMS) properties for biomedical micro/nanosystems,” *Biomed. Microdevices*, vol. 7, no. 4, pp. 281–293, 2005.

[43] E. K. Dimitriadis, F. Horkay, J. Maresca, B. Kachar, and R. S. Chadwick, “Determination of elastic moduli of thin layers of soft material using the atomic force microscope,” *Biophys. J.*, vol. 82, no. 5, pp. 2798–2810, 2002.

[44] I. D. Johnston, D. K. McCluskey, C. K. L. Tan, and M. C. Tracey, “Mechanical characterization of bulk Sylgard 184 for microfluidics and microengineering,” *J. Micromechanics Microengineering*, vol. 24, no. 3, p. 35017, 2014.

[45] M. Liu, J. Sun, Y. Sun, C. Bock, and Q. Chen, “Thickness-dependent mechanical properties of polydimethylsiloxane membranes,” *J. micromechanics microengineering*, vol. 19, no. 3, p. 35028, 2009.

[46] J. K. Deuschle, E. J. de Souza, E. Arzt, and S. Enders, “Nanoindentation studies on crosslinking and curing effects of PDMS,” *Int. J. Mater. Res.*, vol. 101, no. 8, pp. 1014–1023, 2010.

[47] W. Xu, N. Chahine, and T. Sulchek, “Extreme hardening of PDMS thin films due to high compressive strain and confined thickness,” *Langmuir*, vol. 27, no. 13, pp. 8470–8477, 2011.

[48] F. Carrillo, S. Gupta, M. Balooch, S. J. Marshall, G. W. Marshall, L. Pruitt, and C. M. Puttlitz, “Nanoindentation of polydimethylsiloxane elastomers: Effect of crosslinking, work of adhesion, and fluid environment on elastic modulus,” *J. Mater. Res.*, vol. 20, no. 10, pp. 2820–2830, 2005.

[49] S. Gupta, F. Carrillo, C. Li, L. Pruitt, and C. Puttlitz, “Adhesive forces significantly affect elastic modulus determination of soft polymeric materials in nanoindentation,” *Mater. Lett.*, vol. 61, no. 2, pp. 448–451, 2007.

[50] D.-E. Lin, Li-Yu and Kim, “Measurement of the elastic modulus of polymeric films using an AFM.pdf,” 2012.

[51] P. Zheng and T. J. McCarthy, “Rediscovering silicones: Molecularly smooth, low surface energy, unfilled, uv/vis-transparent, extremely cross-linked, thermally stable, hard, elastic pdms,” *Langmuir*, vol. 26, no. 24, pp. 18585–18590, 2010.

[52] A. J. Wrucke, C.-S. Han, and P. Majumdar, “Indentation size effect of multiple orders of magnitude in polydimethylsiloxane,” *J. Appl. Polym. Sci.*, vol. 128, no. 1, pp. 258–264, 2013.

[53] Y. Y. Lim and M. M. Chaudhri, “Indentation of elastic solids with

a rigid Vickers pyramidal indenter," *Mech. Mater.*, vol. 38, no. 12, pp. 1213–1228, 2006.

[54] T.-Y. Zhang and W.-H. Xu, "Surface Effects on Nanoindentation," *J. Mater. Res.*, vol. 17, no. 07, pp. 1715–1720, 2002.

[55] Q. Liao, J. Huang, T. Zhu, C. Xiong, and J. Fang, "A hybrid model to determine mechanical properties of soft polymers by nanoindentation," *Mech. Mater.*, vol. 42, no. 12, pp. 1043–1047, 2010.

[56] B. Bhushan, Y. C. Jung, and K. Koch, "Self-Cleaning Efficiency of Artificial Superhydrophobic Surfaces," *Langmuir*, vol. 25, no. 5, pp. 3240–3248, 2009.

[57] H. E. Jeong and K. Y. Suh, "Nanohairs and nanotubes: efficient structural elements for gecko-inspired artificial dry adhesives," *Nano Today*, vol. 4, no. 4, pp. 335–346, 2009.

[58] D. Paretkar, M. Kamperman, A. S. Schneider, D. Martina, C. Creton, and E. Arzt, "Bioinspired pressure actuated adhesive system," *Mater. Sci. Eng. C*, vol. 31, no. 6, pp. 1152–1159, 2011.

[59] C. S. Chen, M. Mrksich, S. Huang, G. M. Whitesides, and D. E. Ingber, "Geometric Control of Cell Life and Death," *Science (80-.).*, vol. 276, no. 5317, pp. 1425–1428, 1997.

[60] B.-Z. Katz, E. Zamir, A. Bershadsky, Z. Kam, K. M. Yamada, and B. Geiger, "Physical state of the extracellular matrix regulates the structure and molecular composition of cell-matrix adhesions," *Mol. Biol. Cell*, vol. 11, no. 3, pp. 1047–1060, 2000.

[61] M. Ochsner, M. R. Dusseiller, H. M. Grandin, S. Luna-Morris, M. Textor, V. Vogel, and M. L. Smith, "Micro-well arrays for 3D

shape control and high resolution analysis of single cells," *R. Soc. Chem.*, vol. 7, no. 8, pp. 1074–1077, 2007.

[62] D. E. Discher, P. Janmey, and Y.-l. Wang, "Tissue cells feel and respond to the stiffness of their substrate," *Science (80-.).*, vol. 310, no. 5751, pp. 1139–1143, 2005.

[63] J. P. Winer, S. Oake, and P. A. Janmey, "Non-linear elasticity of extracellular matrices enables contractile cells to communicate local position and orientation," *PLoS One*, vol. 4, no. 7, pp. 6382–6388, 2009.

[64] A. J. Engler, S. Sen, H. L. Sweeney, and D. E. Discher, "Matrix elasticity directs stem cell lineage specification," *Cell*, vol. 126, no. 4, pp. 677–689, 2006.

[65] A. Kostic, J. Sap, and M. P. Sheetz, "RPTP is required for rigidity-dependent inhibition of extension and differentiation of hippocampal neurons," *J. Cell Sci.*, vol. 120, no. 21, pp. 3895–3904, 2007.

[66] N. Q. Balaban, U. S. Schwarz, D. Riveline, P. Goichberg, G. Tzur, I. Sabanay, D. Mahalu, S. Safran, and A. Bershadsky, "Force and focal adhesion assembly: a close relationship studied using elastic micropatterned substrates," *Nat. Cell Biol.*, vol. 3, no. 5, pp. 466–472, 2001.

[67] C. G. Galbraith, K. M. Yamada, and M. P. Sheetz, "The relationship between force and focal complex development," *J. Cell Biol.*, vol. 159, no. 4, pp. 695–705, 2002.

[68] C. S. Fu, Jianping and Wang, Yang-Kao and Yang, Michael T and Desai, Ravi A and Yu, Xiang and Liu, Zhijun and Chen, "Mechanical regulation of cell function with geometrically modulated elastomeric substrates," *Nat. Methods*, vol. 7, no. 9, 2010.

[69] J. Mathur, A and Roca-Cusachs, P and Rossier, OM and Wind, SJ and Sheetz, MP and Hone, "New approach for measuring protrusive forces in cells," *J. Vac. Sci. Technol. B*, vol. 29, no. 6, pp. 06–12, 2011.

[70] C. S. Chen, "Mechanotransduction–a field pulling together ?," *J. Cell Sci.*, vol. 121, no. 20, pp. 3285–3292, 2008.

[71] J. H. Wang and J.-S. Lin, "Cell traction force and measurement methods," *Biomech. Model. Mechanobiol.*, vol. 6, no. 6, pp. 361–371, 2007.

[72] N. J. Sniadecki, A. Anguelouch, M. T. Yang, C. M. Lamb, Z. Liu, S. B. Kirschner, Y. Liu, D. H. Reich, and C. S. Chen, "Magnetic microposts as an approach to apply forces to living cells," *Proc. Natl. Acad. Sci.*, vol. 104, no. 37, pp. 14553–14558, 2007.

[73] J. L. Tan, J. Tien, D. M. Pirone, D. S. Gray, K. Bhadriraju, and C. S. Chen, "Cells lying on a bed of microneedles: an approach to isolate mechanical force," *Proc. Natl. Acad. Sci.*, vol. 100, no. 4, pp. 1484–1489, 2003.

[74] M. Ghibaudo, A. Saez, L. Trichet, A. Xayaphoummine, J. Browaeys, P. Silberzan, A. Buguin, and B. Ladoux, "Traction forces and rigidity sensing regulate cell functions," *Soft Matter*, vol. 4, no. 9, pp. 1836–1843, 2008.

[75] A. Rabodzey, P. Alcaide, F. W. Luscinskas, and B. Ladoux, "Mechanical forces induced by the transendothelial migration of human neutrophils," *Biophys. J.*, vol. 95, no. 3, pp. 1428–1438, 2008.

[76] N. J. Sniadecki, C. M. Lamb, Y. Liu, C. S. Chen, and D. H. Reich, "Magnetic microposts for mechanical stimulation of biological

cells: fabrication, characterization, and analysis," *Rev. Sci. Instrum.*, vol. 79, no. 4, pp. 32–44, 2008.

[77] K. T. Bashour, A. Gondarenko, H. Chen, K. Shen, X. Liu, M. Huse, J. C. Hone, and L. C. Kam, "CD28 and CD3 have complementary roles in T-cell traction forces," *Proc. Natl. Acad. Sci.*, vol. 111, no. 6, 2014.

[78] F. Khademolhosseini, C.-C. Liu, C. J. Lim, and M. Chiao, "Application of periodic loads on cells from magnetic micropillar arrays impedes cellular migration," in *Micro Electro Mech. Syst. (MEMS), 2015 28th IEEE Int. Conf.*, pp. 624–627, 2015.

[79] O. Du Roure, A. Saez, A. Buguin, R. H. Austin, P. Chavrier, P. Siberzan, and B. Ladoux, "Force mapping in epithelial cell migration," *Proc. Natl. Acad. Sci. U. S. A.*, vol. 7, no. 7, pp. 2390–2395, 2005.

[80] I. Schoen, W. Hu, E. Klotzsch, and V. Vogel, "Probing cellular traction forces by micropillar arrays: contribution of substrate warping to pillar deflection," *Nano Lett.*, vol. 10, no. 5, pp. 1823–1830, 2010.

[81] P. Du, I.-K. Lin, H. Lu, and X. Zhang, "Extension of the beam theory for polymer bio-transducers with low aspect ratios and viscoelastic characteristics," *J. Micromechanics Microengineering*, vol. 20, no. 9, pp. 95–100, 2010.

[82] J. Y. Lee, W. K. Seong, I.-S. Choi, R. Ghosh, A. Vaziri, C.-W. Yang, K.-R. Lee, and M.-W. Moon, "In situ Measurement of the Adhesion Strength and Effective Elastic Stiffness of Single Soft Micropillar," *J. Adhes.*, vol. 91, no. 5, pp. 369–380, 2015.

[83] P. Du, C. Cheng, H. Lu, and X. Zhang, “Investigation of cellular contraction forces in the frequency domain using a PDMS micropillar-based force transducer,” *J. Microelectromechanical Syst.*, vol. 22, no. 1, pp. 44–53, 2013.

[84] P. Du, X. Zheng, I.-K. Lin, and X. Zhang, “Effect of loading rates on cellular force measurements by polymer micropillar based transducers,” *Appl. Phys. Lett.*, vol. 99, no. 8, pp. 83–89, 2011.

[85] A. Sedlmayr, *Experimental Investigations of Deformation Pathways in Nanowires*. 2014.

[86] H. Lee, K. Lee, B. Ahn, J. Xu, L. Xu, and K. W. Oh, “A new fabrication process for uniform SU-8 thick photoresist structures by simultaneously removing edge bead and air bubbles,” *J. Micromechanics Microengineering*, vol. 21, no. 12, pp. 125–130, 2011.

[87] L. Euler, “Methodus inveniendi lineas curvas maximi minimive proprietate gaudentes (appendix, de curvis elasticis),” *Lausanne und Genf*, vol. 1744, 1774.

[88] S. Timoshenko and S. Woinowsky-Krieger, *Theory of plates and shells*. McGraw-hill New York, 1959.

[89] D. C. Lam, F. Yang, A. Chong, J. Wang, and P. Tong, “Experiments and theory in strain gradient elasticity,” *J. Mech. Phys. Solids*, vol. 51, no. 8, pp. 1477–1508, 2003.

[90] S. Park and X. Gao, “Bernoulli–Euler beam model based on a modified couple stress theory,” *J. Micromechanics Microengineering*, vol. 16, no. 11, pp. 2355–2360, 2006.

[91] M. Mooney, "A theory of large elastic deformation," *J. Appl. Phys.*, vol. 11, no. 9, pp. 582–592, 1940.

[92] R. Rivlin and J. Ericksen, "Stress-deformation relations for isotropic materials," *J. Ration. Mech. Anal.*, vol. 4, no. 3, pp. 323–425, 1955.

[93] R. W. Ogden, *Non-linear elastic deformations.* Courier Corporation, 1997.

[94] O. Yeoh, "Some forms of the strain energy function for rubber," *Rubber Chem. Technol.*, vol. 66, no. 5, pp. 754–771, 1993.

[95] Y.-S. Yu and Y.-P. Zhao, "Deformation of PDMS membrane and microcantilever by a water droplet: Comparison between Mooney–Rivlin and linear elastic constitutive models," *J. Colloid Interface Sci.*, vol. 332, no. 2, pp. 467–476, 2009.

[96] T. K. Kim, J. K. Kim, and C. Jeong, "Measurement of nonlinear mechanical properties of PDMS elastomer," *Microelectron. Eng.*, vol. 88, no. 8, pp. 1982–1985, 2011.

[97] J. Gao, D. Guo, S. Santhanam, and G. K. Fedder, "Large stroke electrostatic actuated PDMS-on-silicon micro-pump," in *18th Int. Conf. Solid-State Sensors, Actuators Microsystems*, pp. 117–120, 2015.

[98] "COMSOL Multiphysics," 2015.

[99] T. Peng, "MATLAB Central: Detect circles with various radii in grayscale image via Hough Transform," 2010.

[100] L. Trichet, L. Digabel, H. Jimmy, V. Rhoda, K. Sri Ram, M. Gupta, C. Ribrault, P. Hersen, R. Voituriez, and B. Ladoux, "Evidence of a large-scale mechanosensing mechanism for cellular adaptation to

substrate stiffness," *Proc. Natl. Acad. Sci.*, vol. 109, no. 18, pp. 6933–6938, 2012.

[101] F. Heinemann, H. Doschke, and M. Radmacher, "Keratocyte lamellipodial protrusion is characterized by a concave force-velocity relation," *Biophys. J.*, vol. 100, no. 6, pp. 1420–1427, 2011.

[102] D. Rosel, J. Brabek, O. Tolde, C. T. Mierke, D. P. Zitterbart, C. Raupach, K. Bicanova, and P. Kollmannsberger, "Up-regulation of Rho/ROCK signaling in sarcoma cells drives invasion and increased generation of protrusive forces," *Mol. Cancer Res.*, vol. 9, no. 9, pp. 1410–1420, 2008.

[103] V. Peschetola, V. M. Laurent, A. Duperray, R. Michel, D. Ambrosi, L. Preziosi, and C. Verdier, "Time-dependent traction force microscopy for cancer cells as a measure of invasiveness," *Cytoskeleton*, vol. 70, no. 4, pp. 201–214, 2013.

[104] P. Wang, J. Su, C.-F. Su, W. Dai, G. Cernigliaro, and H. Sun, "An ultrasensitive quartz crystal microbalance-micropillars based sensor for humidity detection," *J. Appl. Phys.*, vol. 115, no. 22, p. 224501, 2014.

[105] E. Cinar and F. Sahin, "A System of Systems Perspective to a Multi-Probe SPM System," *Int. J. Complex Syst. Comput. Sens. Control*, 2015.

[106] E. Cinar and F. Sahin, "A system of systems analysis of a multi-probe SPM system," in *IEEE 10th Syst. Syst. Eng. Conf.*, pp. 117–121, 2015.

Appendix A

A Closer Look at the Multi-Probe System Operation

A.1 Tuning fork excitation mechanism

Under the upper piezo scanner system, there is an electroblock unit that carries piezo excitation elements as shown in Figure A.1. The tuning fork is excited with voltages ranging from 0-5 V and the preamp block is used to amplify the electrical signal that is read from the fork itself. Oscillations can be controlled by regulating the voltage of the excitation.

A tuning fork is excited at a fixed frequency (resonance frequency) of the probe. The lock-in controllers detect the change in amplitude and phase based on an internal reference signal. Assume that this reference signal has a frequency ω_r. If a sine wave signal is used to excite the tuning fork, then the signal will be in the form $V_{sig} sin(\omega_{sig} t + \theta_{sig})$ where V_{sig} is the signal

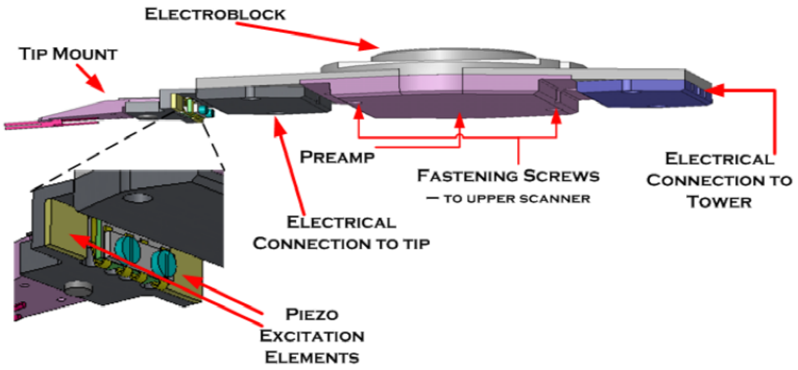

Figure A.1: Schematic showing the excitation block where tuning fork piezo excitation elements are placed [11]

amplitude, and θ_{sig} is the signal's phase. Similarly a reference signal can be represented as $V_{ref} sin(\omega_{ref} t + \theta_{ref})$. If the two signals are multiplied:

$$\begin{aligned} V &= V_{sig} sin(\omega_{sig} t + \theta_{sig}) V_{ref} sin(\omega_{ref} t + \theta_{ref}) \\ &= \frac{1}{2} V_{sig} V_{ref} cos([\omega_{sig} - \omega_{ref}]t + \theta_{sig} - \theta_{ref}) - \frac{1}{2} V_{sig} V_{ref} cos([\omega_{sig} + \omega_{ref}]t \\ &+ \theta_{sig} + \theta_{ref}) \end{aligned} \tag{A.1}$$

Equation A.1 includes two AC signals, one include the difference frequencies and the other one includes the sum of frequencies. If the signal is passed through a low pass filter, the AC signals will be removed and if $\omega_{sig} = \omega_{ref}$, the result of the low pass filter will be a DC signal with the following form.

$$V_1 = \frac{1}{2} V_{sig} V_{ref} \cos(\theta_{sig} - \theta_{ref}) \tag{A.2}$$

One can adjust θ_{ref} so that $\theta = \theta_{sig} - \theta_{ref} = 0$. This will give an output where we can directly measure V_{sig}. In addition, if we shift the reference signal 90^o and multiply the actual signal with $V_{ref} sin(\omega_{ref} t + \theta_{ref} + 90^o)$ then we can obtain eq. A.3.

$$V_2 = \frac{1}{2} V_{sig} V_{ref} \sin(\theta_{sig} - \theta_{ref}) \tag{A.3}$$

Therefore, we can have two output vectors from lock-in controller where $X = V_{sig} \cos\theta$ and $Y = V_{sig} \sin\theta$. The magnitude of the vectors can be calculated to obtain V_{sig} that is $R = \sqrt{X^2 + Y^2}$ and the phase difference can be calculated as $\theta = \tan^{-1}(Y/X)$.

Figure A.2 demonstrates the basic blocks of tuning fork excitation. Lock-in amplifiers are used to set Amplitude and Phase of fork oscillation so that the fork can oscillate at its resonant frequency. By using Phase-lock-loop (PLL) system and based on the internal reference signal, phase and amplitude shifts can be detected and processed as error signal by the PID controllers. High voltage adapters can be used to excite the piezo scanner based on the processed error signal within the system.

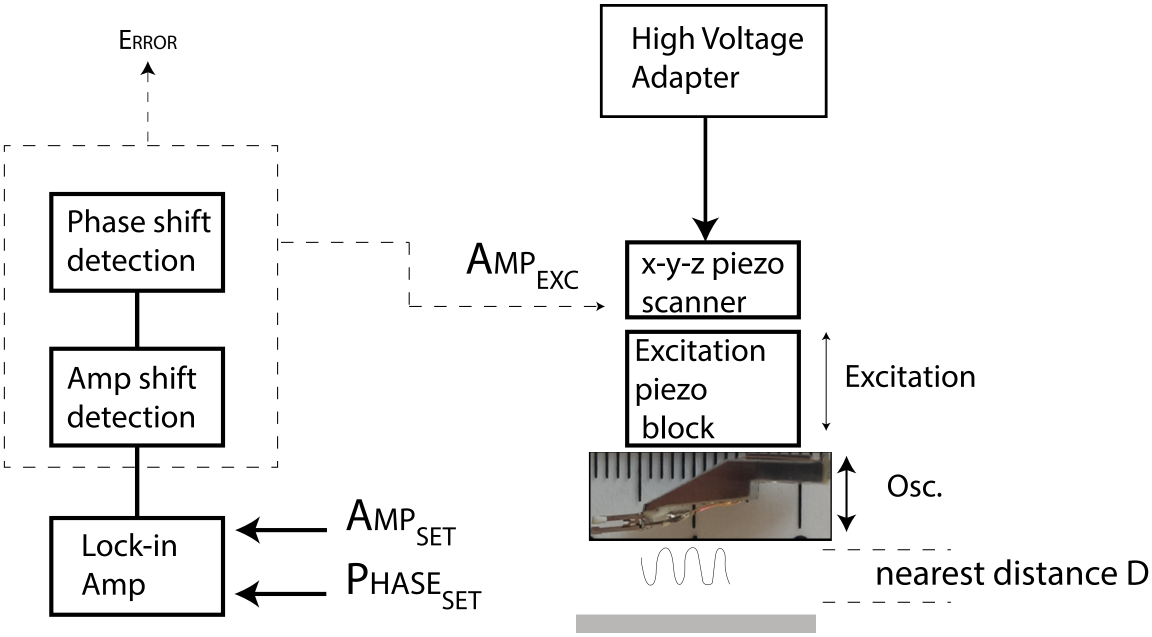

Figure A.2: Tuning fork excitation elements and their positions

A.2 Nano-work-shop (NWS) control software

In order to provide an extensive user interface to the tool, each probe terminal can be independently operated by control software installed on separate PCs for the corresponding towers. Nano-work-shop (NWS) control software is a lab-view based software that can process signals coming from DAQ card hardware connected to the PC.

Figure A.3(a) and A.3(b) demonstrate the example images of NWS control software. Figure A.3(a) shows the results of a silicon specimen surface AFM scan after an indentation experiment is performed with a multi-probe nanoindentation approach. The SPM control section of the software includes lock-in settings system module. In this module,lock-in settings of a newly mounted probe is configured. In addition, a stepper motor control section is where coarse Z-movement of the probe are controlled during approach and retract of the tip as well as a nanoindentation module where a controlled tip pressing is performed. The Force/Distance diagram menu shows the generated Force curves after nanoindentation experiments which include force calculation algorithms developed during the course of this dissertation work and is explained further in detail in a later chapter (chapter 4).

By the help of open design, user can write codes for individualized operations and enable interfacing to other LabView modules for different equipments. Signals up to 8 different channels can be acquired for image construction and integration with external equipments.

A.3 System Calibration

For calibration, two independent systems, a scanning AFM tower system and the lower sample scanner system are interconnected through auxiliary port of the data translation interface terminals. The aim of the calibration is to adjust the calibration coefficients of the system for certain physical measurements such as validity of the height information as well as multi-system operation. The AFM tower system is equipped with a probe that is

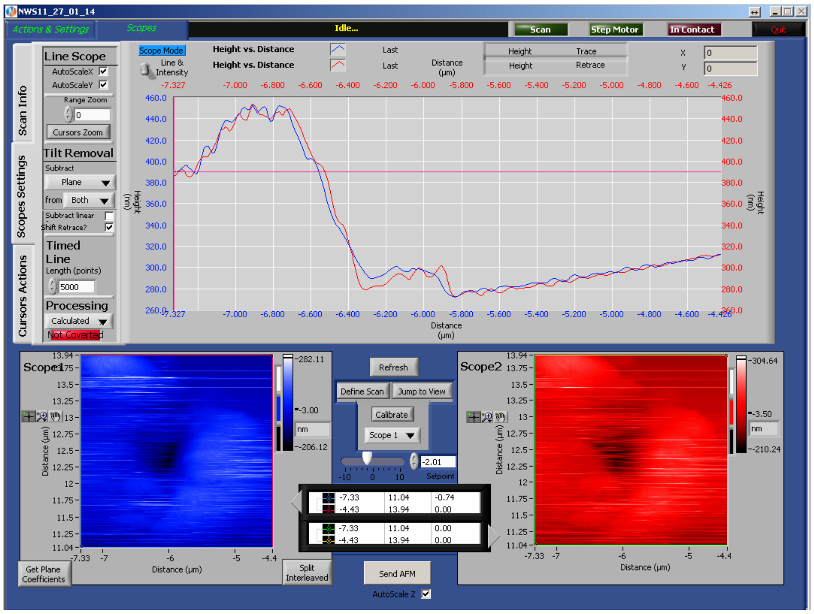

(a) NWS software after scanning a nanoindentation mark on a silicon surface

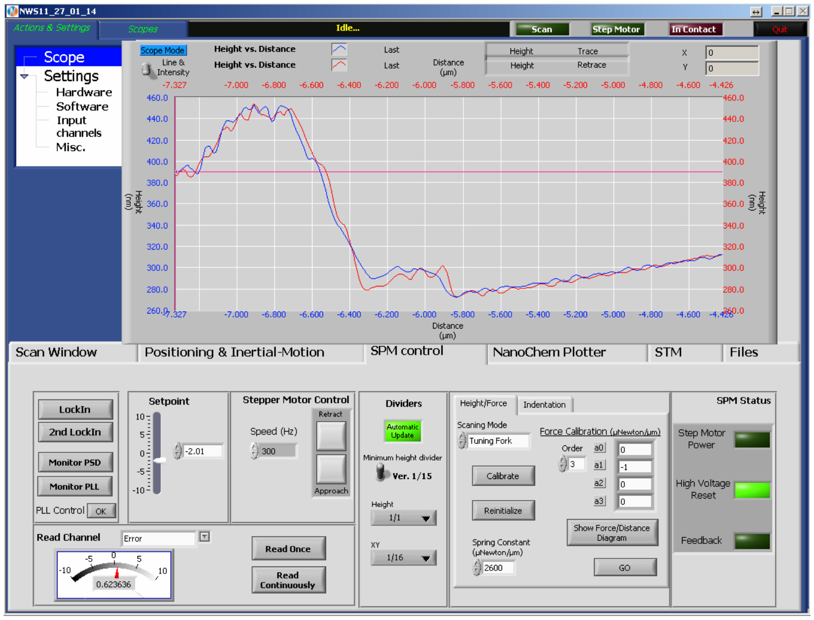

(b) NWS software SPM Control Menu

Figure A.3: Calibrated system scan outputs and height information verifying the calibrated system measurements

specially used for AFM scanning. It includes a $300 \mu m$ length cantilevered probe tip with a 20 nm radius at the end. A schematic representation of the system configuration is given in Figure A.4. The height information of the AFM tower system is transferred through the lower scanner system by the data translation interface box terminals. The system is configured to make a scan of the calibration grid chip which includes 115 nm of micropillar structures. In this configuration, AFM tower system is configured to make movements only in the Z axis where the lower scanner system is configured to move the sample only in X and Y axis. After programming the scanning parameters and when the user starts the scan, the AFM tower system always stays in constant feedback contact with the sample and changes only the Z-position by moving up and down. As the AFM tower system scans the sample in the Z direction, it sends the height information that is how much it moves up and down in the Z axis to the lower sample scanner system software through Data Translation interface unit. As a result, an image of the surface topography is constructed according to the data exchanged and combined on the lower scanner system computer.

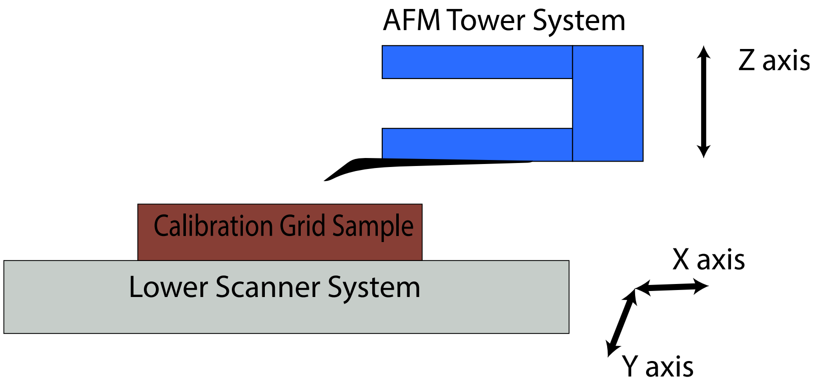

Figure A.4: Multi-probe SPM system calibration

Figure A.5(a) presents the results of calibration scan of the system when two independent systems work in tandem through data exchange. On the left is a 2D microscope image of the calibration chip. The sample includes 115 nm SiO_2 micropillars and microwells on a silicon chip. On the right is an image constructed at the lower scanner system terminal by the data collected from the AFM tower system as well as the lower scanner system. Figure A.5(b) is the height profile showing the accurate micropillar information in nanometers after the calibration coefficients of the system are adjusted according to the actual height of the calibration chip.

A.4 Example applications using the multi-probe system

Simultaneous operation of multiple independent systems in MV-4000 and its highly interoperable architecture enables solving complex tasks effectively. One of these applications is in the field of Near-Scanning-Optical-Microscopy (NSOM). NSOM is a microscopy technique that allows users to obtain an image of a surface beyond the resolution limit of light. In order to do this, the surface is illuminated with a laser light source through a fiber on the tip of the probe and the second probe is used to collect the lights scattered from the surface at an extremely close distance from the surface. In order to achieve this, two tower systems and the lower scanner system is

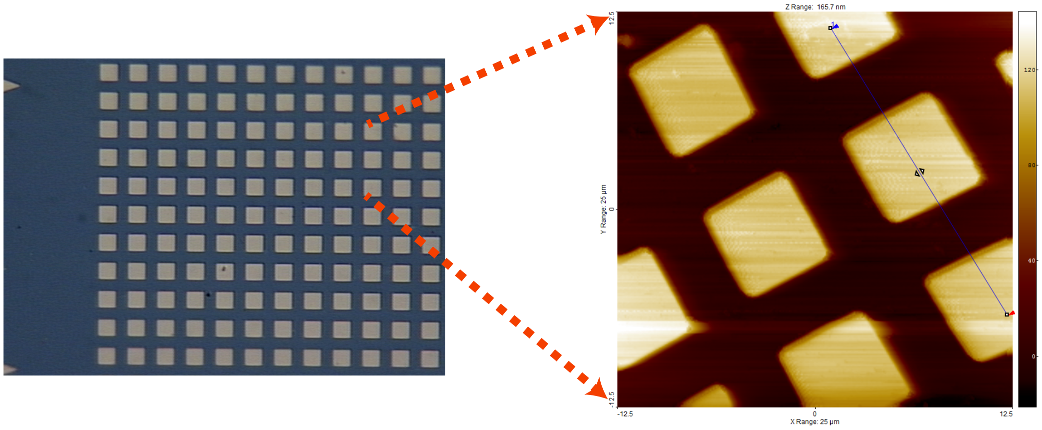

(a) Microscope picture of calibration grid and an AFM scan performed after system calibration.

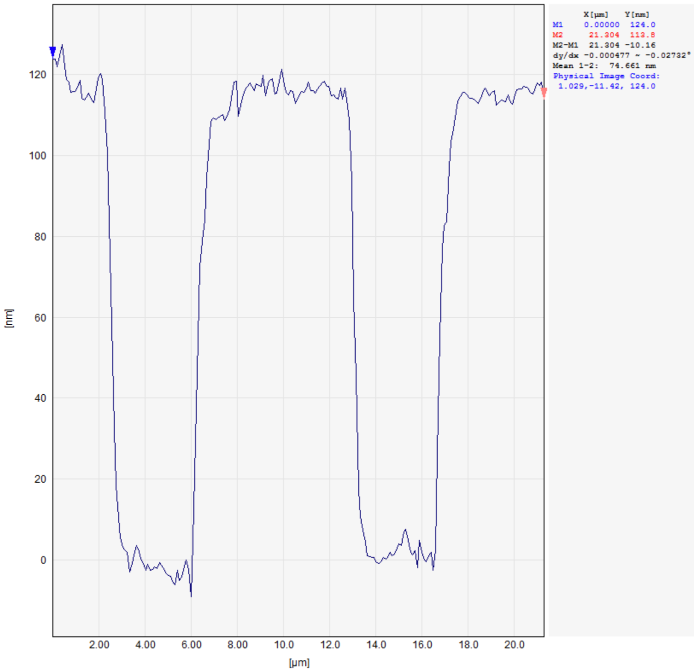

```
        X[µm]    Y[nm]
M1    0.00000  124.0
M2     21.304  113.8
M2-M1  21.304 -10.16
dy/dx -0.000477 ~ -0.02732°
Mean 1-2:  74.661 nm
Physical Image Coord:
 1.029,-11.42, 124.0
```

(b) The height profile along the line drawn in the AFM scan image showing ∼ 115nm height value

Figure A.5: Calibrated system scan outputs and height information verifying the calibrated system measurements.

configured to operate simultaneously as shown schematically in Figure A.6. A photon counter detector system is connected through one of the tower systems by NSOM or AUX2 input channel of Data Translation Interface.

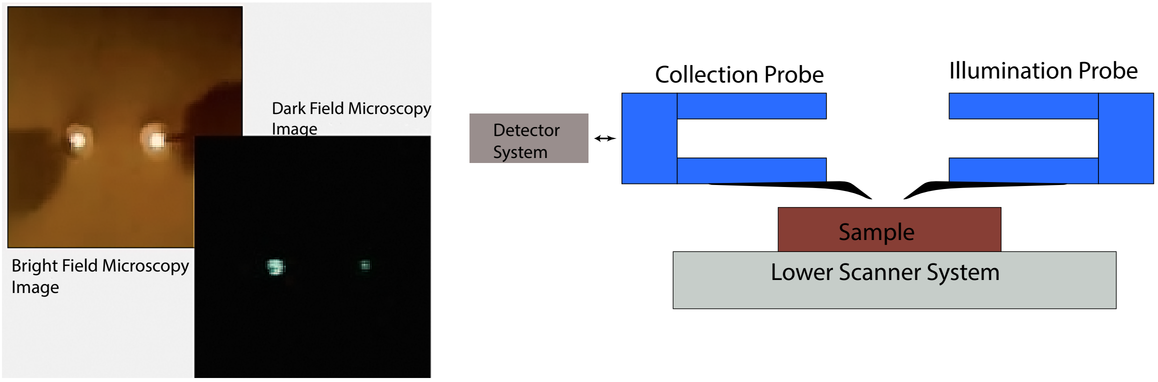

Figure A.6: An example application of simultaneous operation of multiple systems to achieve NSOM measurements (The microscopy images are courtesy of Nanonics Imaging Ltd.)

As one of the tower systems function as a light source for the illumination of material surface, the second system is used as a photon collector in order to count photons. At the end, a simultaneous scan is performed and an ultra-high resolution of both spatial and temporal surface image are extracted by the help of multiple systems operations. Another example to the applications using simultaneous operation of tower systems, it is possible to create a system configuration by integrating electrical probes and measurement tools in order to measure the electrical properties of the materials. Similar to a measurement of resistivity with a conventional multi-meter that has two terminals, the two electrical probes can be used to measure the electrical properties with readily available nanometric positioning and manipulation of the systems. One of the towers can be equipped with conductive electrical wire probes, voltage suppliers and it can be used to bias the surface. At the same time, the second probe can be used to measure the electrical properties of the surface. Up to four probes can be used, simultaneously in this operation to achieve more complex tasks. The flexible system design architecture and its capabilities are investigated more in depth from system engineering perspectives in our publications [105], [106].